UNIVERSITY OF CALIFORNIA SAN DIEGO

Effect of Target Material on Fast Electron Transport

A dissertation submitted in partial satisfaction of the
requirements for the degree
Doctor of Philosophy

in

Engineering Sciences (Engineering Physics)

by

Sugreev Chawla

Committee in charge:

Professor Farhat Beg, Chair
Alexey Arefiev
Cliff Surko
Mark Tillack
George Tynan
Mingsheng Wei

2019

The dissertation of Sugreev Chawla is approved, and it is acceptable in quality and form for publication on microfilm and electronically:

_____

_____

_____

_____

_____

_____
Chair

University of California San Diego

2019

DEDICATION

To my parents, for teaching me the importance of selflessness, generosity, humility and education.

EPIGRAPH

ARI: Only a fool thinks he can solve the world's problems.

GUS: Yeah, but you've got to try, don't you?

— Fargo

Season 1, Episode 5

TABLE OF CONTENTS

LIST OF FIGURES

LIST OF TABLES

ACKNOWLEDGEMENTS

This work performed under the auspices of the U.S. Department of Energy by Lawrence Livermore National Laboratory under Contract DE-AC52-07NA27344.

Chapter 5, in part, is a reprint of material as it appears in S. Chawla, M.S. Wei, R. Mishra, K.U. Akli, C.D. Chen, H.S. McLean, A. Morace, P.K. Patel, H. Sawada, Y. Sentoku, R.B. Stephens, F.N. Beg, Physical Review Letters **110**, 025001 (2013). The dissertation author was the primary investigator and author of this paper.

Chapter 6, in part, is a reprint of material as it appears in S. Chawla, M. Bailly-Grandvaux, H.S. McLean, P.K. Patel, M.S. Wei, F.N. Beg, Physics of Plasmas **26**, 033111 (2019). The dissertation author was the primary investigator and author of this material.

VITA

2005	B.A. Physics, B.A. Applied Mathematics, University of California, Berkeley
2010	M.S. Engineering Sciences (Engineering Physics), University of California, San Diego
2019	Ph.D. Engineering Sciences (Engineering Physics), University of California, San Diego

ABSTRACT OF THE DISSERTATION

Effect of Target Material on Fast Electron Transport

by

Sugreev Chawla

Doctor of Philosophy in Engineering Sciences (Engineering Physics)

University of California San Diego, 2019

Professor Farhat Beg, Chair

In cone-guided fast ignition (FI) inertial confinement fusion, successful ignition relies on the efficient transport of a relativistic electron beam (REB) through a solid density cone tip to a high-density fuel core. A variety of physics mechanisms affect the quality of beam transport, and these effects vary with tip material. This thesis presents a systematic study of the effect of tip material on REB transport.

An experiment was performed using the Titan laser (150 J, 0.7 ps pulse duration, 1 μm wavelength) at LLNL on multilayered targets with varying transport layers. A more collimated electron beam was consistently observed using high- or mid-Z transport layers as compared to low Z layers, without a significant loss in forward-going electron energy flux. PIC simulations

agreed well with experiments, showing the formation of strong resistive magnetic channels ($\sim$80 MG) enveloped by a global B-field that collimate initially divergent fast electrons (in high-Z targets). These results illustrated the dynamic competition between stopping and collimation that is essential to understand in order to optimize electron flux levels.

Hybrid-PIC simulations further investigated transport in various materials at Titan laser conditions. REB energy loss from stopping was similar in low- and mid-Z materials (21 - 27 %), and much higher in Au (54 %), dominated by ohmic stopping. Resistive magnetic field growth was shown to depend on the dynamic competition between the resistivity and resistivity gradient source terms in Faraday's Law. Resistivity evolution, in addition, was shown to depend on the Spitzer-like competition between the ionization state and temperature growth rates. Results suggest that, at Titan conditions, mid-atomic number materials like Cu and Ag are optimal for collimation.

This work has significant implications for fast ignition. At FI conditions, more energy will be injected into the cone tip very quickly, leading to faster ionization and heating rates. Higher atomic number materials may be favorable at these conditions as ionization can continue for a longer period during a $\sim$20 ps FI pulse. These results motivate further computational and experimental work to investigate how multilayer targets can be exploited to maximize fast electron beam collimation whilst minimizing deposition rates.

Chapter 1

Introduction

1.1 ICF Basics

Inertial Confinement Fusion (ICF) is an approach to fusion that relies on the fuel mass inertia for confinement [1] for a long enough time for efficient thermonuclear burn to occur. The fusion reaction of deuterium and tritium,

$$D + T = n\,(14.06\,MeV) + \alpha\,(3.52\,MeV) \tag{1.1}$$

has the largest reaction rate (up to 2 orders of magnitude) than other candidate reactions up to temperatures of around 400 keV (see Fig. 1.1), and is therefore the preferred fuel for fusion schemes.

As shown in Fig. 1.2, ICF targets generally consist of a spherical shell filled with low-density gas ($\leq$ 1.0 mg/cm^3). The shell is made up of an outer ablator layer and an inner layer of frozen or liquid DT fuel. In the ignition scheme known as central hotspot ignition (CHS) ignition, energy from a laser driver is delivered to the ablator layer. As the ablator heats and expands outward, the rest of the shell is pushed inward with rocket-like motion. In its final configuration, the fuel is nearly isobaric with a central hotspot region containing 2-5% of the

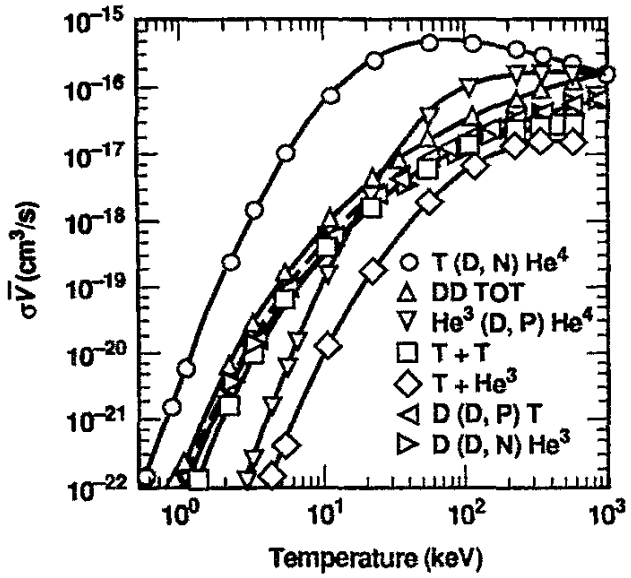

Figure 1.1: Thermonuclear reaction rates for various fusion reactions. Figure taken from Lindl[1].

fuel and a dense main fuel region surrounding it and containing the remaining mass. Ignition occurs in the central region and the thermonuclear burn propagates radially outward to the main fuel producing high gain.

The fuel conditions required for efficient burn and high yield relative to the driver energy can be obtained by analyzing the burn fraction of the fuel. The rate of thermonuclear reactions n is given by

$$\frac{dn}{dt} = N_D N_T \langle \sigma v \rangle, \tag{1.2}$$

where $\langle \sigma v \rangle$ is the reaction cross section averaged over a Maxwellian distribution of particles and

$$N_D = N_T = \left(\frac{1}{2} N_0 - n \right) \tag{1.3}$$

assuming an equimolar DT mixture where N_0 is the initial total number density. Defining the

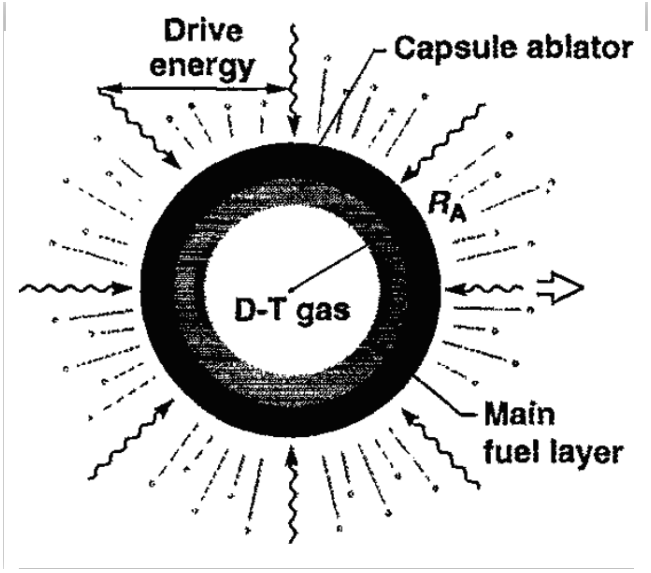

Figure 1.2: Configuration of an ICF target and driver beams. Figure taken from Lindl[1].

burn fraction as $\phi = 2n/N_0$, Eq. 1.2 becomes

$$\frac{d\phi}{dt} = \frac{N_0}{2}(1-\phi)^2\langle\sigma v\rangle. \tag{1.4}$$

Assuming the cross section is nearly constant over the burn duration, this equation can be integrated to get

$$\frac{\phi}{1-\phi} = \frac{N_0\tau}{2}\langle\sigma v\rangle. \tag{1.5}$$

where τ is the confinement time. For ICF, the burn of an ignited fuel mass is usually quenched by hydrodynamic expansion, so we can estimate the confinement time to be on the order of time for a rarefaction wave to propagate across the main fuel layer. If the speed of sound is C_s and we choose $\tau \approx r/3C_s$, the burn efficiency can be written as

$$\frac{\phi}{1-\phi} = \frac{N_0}{2}\langle\sigma v\rangle \frac{r}{6C_s}. \tag{1.6}$$

Typical temperatures associated with the burn of DT ICF capsules range from 20 - 40 keV.

The ratio of the cross section to the sound speed is nearly constant in this range, and we have approximately

$$\phi = \frac{\rho r}{\rho r + 6\ (g/cm^3)}, \tag{1.7}$$

where the number density N_0 has been related to the mass density ρ using

$$N_0 = 6.02 \times 10^{23}\ \frac{Z}{A}\ \rho\ \approx\ 2.4 \times 10^{23} \text{ for DT.} \tag{1.8}$$

Assuming a reasonable burn fraction of 1/3, Eq. 1.7 dictates $\rho r = 3$ g/cm^3. Writing the mass of a spherical volume as

$$M_f = \frac{4\pi}{3} \frac{(\rho r)^3}{\rho^2} \tag{1.9}$$

and assuming M_f=1 mg yields a fuel density of ρ **= 300 g/cm**^{3}.

The temperature requirement for ignition is based on effective internal heating of the fuel by α particles. Not only must the heating overcome energy loss from radiation, thermal conduction and hydrodynamic expansion, but the temperature must be such that the α-particle range is less than the hotspot ρr. The issue of α-particle range is dominant, and at densities between 10-100 g/cm^3 the range can be fitted by

$$\rho r = \frac{0.015\ T_e^{5/4}}{1 + 0.0082\ T_e^{5/4}} \tag{1.10}$$

which yields $\rho r\ \approx 0.4$ g/cm^2 at **10 keV**[10].

These compression and heating requirements necessitate a very uniform target surface and highly symmetric compression beams. Moreover, the efficiency of this ignition scheme is sensitive to the Rayleigh-Taylor instability. An alternative scheme, Fast Ignition, offers higher gains and reduced symmetry requirements by decoupling the compression and ignition stages of fusion process.

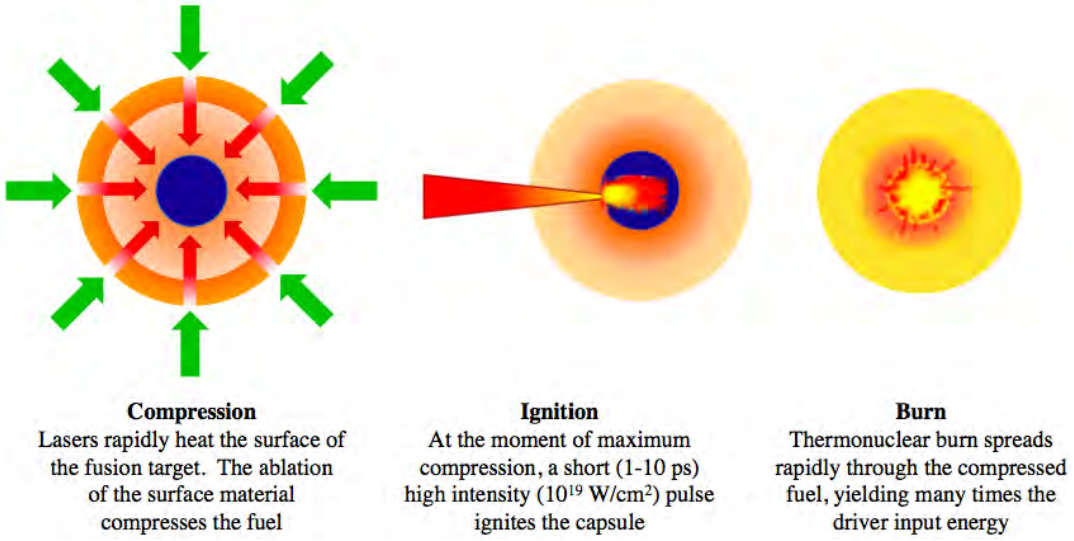

Figure 1.3: Schematic of the fast ignition fusion concept. Figure courtesy of T. Ma, LLNL.

1.2 Fast Ignition

The advent of the chirped pulse amplification (CPA)[11] technology and optical parametric amplification (OPA)[12, 13] have allowed for petawatt (10^{15} W) laser intensities to be achieved, yielding the possibility for an alternative ignition scheme known as fast ignition (FI)[14]. In CHS, fuel compression and ignition are coupled, placing high symmetry requirements on the laser drive. FI offers a scheme to decouple ignition and compression, reducing the driver energy required for compression and lowering the sensitivity to hydrodynamic instabilities.

In the FI scheme, as shown in Fig. 1.3, a laser driver similar to that of CHS would compress and assemble the high-density fuel. At maximum fuel compression, a short-pulse high-intensity ignitor laser would irradiate the capsule producing suprathermal electrons at the plasma critical density that then ignite the fuel. The thermonuclear burn would then consume the capsule.

The requirements for ignition in the FI scheme are significantly different from those of CHS, mainly because the fuel compression is isochoric and ignition energy is delivered by energetic particles (see Fig. 1.4). This lower density, larger fuel volume allows for less stringent

convergence requirements and, therefore, hydrodynamic instabilities are not as detrimental. In addition, a lower density implies more mass to burn and higher gain.

Atzeni[3] performed detailed 2D radiation-hydrodynamic simulations of ignition of pre-compressed fuel by fast particles in order to calculate ignition conditions for FI. In the density interval of $50 \leq \rho \leq 3000$ g/cm^3, a parallel beam of unspecified fast particles with straight path and uniform stopping power delivered energy to plasma electrons. The beam had constant power W_p for duration t_p and an intensity I_p distributed uniformly over a circular cross section of radius r_b, so that $W_p = I_p \pi r_b^2$ and $E_p = W_p t_p$. A large set of simulations determined ignition would occur if beam energy, power and intensity simultaneously exceed threshold values given by:

$$E_{ig} = 140 \left(\frac{\rho}{100 \text{ g/cm}^3} \right)^{-1.85} \text{kJ} \tag{1.11}$$

$$W_{ig} = 2.6 \times 10^{15} \left(\frac{\rho}{100 \text{ g/cm}^3} \right)^{-1} \text{W} \tag{1.12}$$

$$I_{ig} = 2.4 \times 10^{19} \left(\frac{\rho}{100 \text{ g/cm}^3} \right)^{-0.95} \text{W/cm}^2 \tag{1.13}$$

Ignition thresholds were found to vary very weakly with fast particle range R, and the value of $R = 0.6$ g/cm^2 was optimal or close to optimal. Plots of ignition windows for various values of density can be seen in Fig. 1.5. These plots imply that for a full-scale FI scheme, the optimal set of parameters to ignited compressed DT fuel with a density of 300 g/cm^3 are $r_b = 21$ μm, $I_p = 6.3 \times 10^19$ W/cm^2, $t_p = 20$ ps, and $E_p = 20$ kJ.

1.3 Cone-guided Fast Ignition

Though FI alleviates the symmetry and hydrodynamic issues of CHS whilst providing higher gain, problems arise with the transport of energy from the the plasma critical density location to the compressed fuel. The ablation during fuel assembly creates a significant amount of coronal plasma that pushes the critical density location $\sim$100 μm from the compressed fuel.

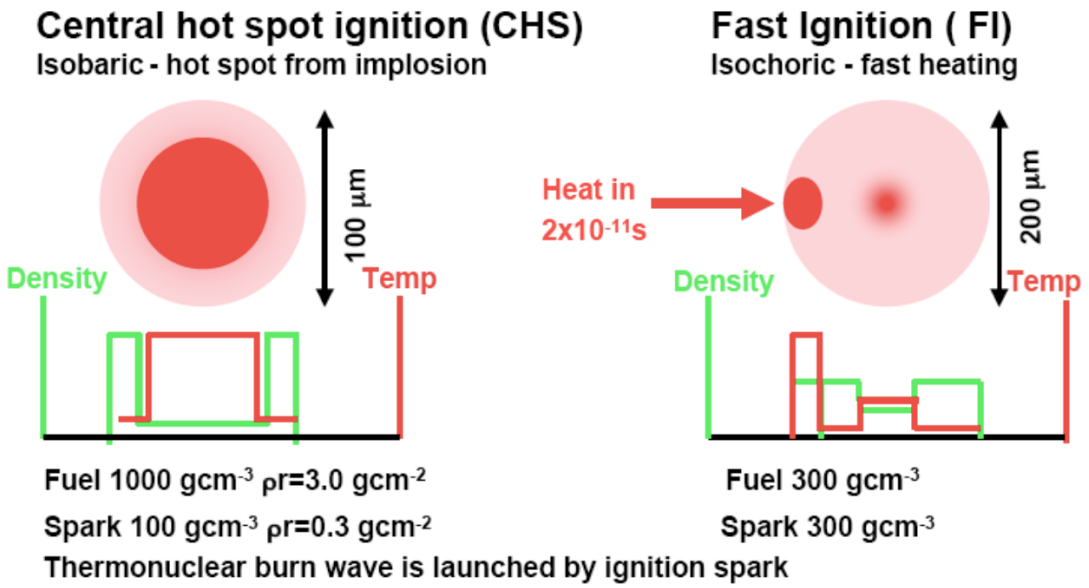

Figure 1.4: Comparison of CHS and FI fuel assemblies. Note the low-density, high-temperature hot spot in the CHS scheme and the constant density fuel assembly in the FI scheme. Figure taken from Mackinnon[2].

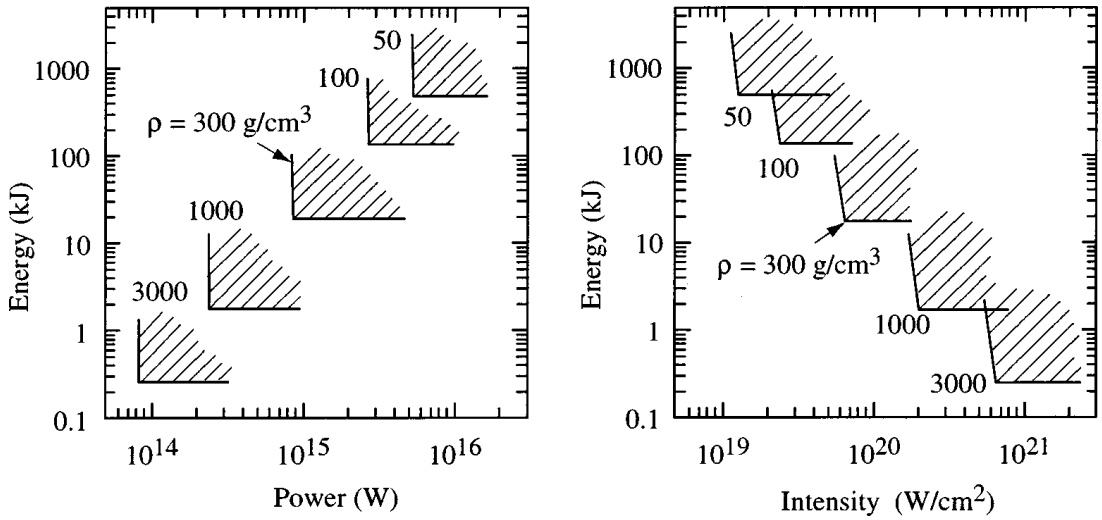

Figure 1.5: Lower left corner of ignition windows for different values of pre compressed fuel, assuming a particle range $R = 0.6$ g/cm^2. Figure taken from Atzeni[3].

Fast electrons created by laser plasma interaction then need to travel this distance and deliver the minimum amount of energy within a certain area for ignition. Transport over this range is subject to scattering and beam-plasma instabilities (Weibel) that can significantly lower the amount of energy reaching the core.

Cone guided FI attempts to decrease the standoff distance between electron source and fuel surface using a cone embedded in the fuel capsule (see Fig. 1.6). Though its feasibility has been verified experimentally[15, 16], major issues remain. As described in Chapter 4, the main pulse of an FI ignitor beam is always preceded by relatively low intensity pre-pulse. There is enough energy in this pre-pulse to ablate solid material from the interior cone tip and walls, creating preplasma and pushing back the plasma critical density away from the fuel. The laser-plasma interaction creates relativistic or fast electrons that then need to propagate through the pre plasma and solid cone tip, and successfully deposit the bulk of their energy to the compressed fuel for ignition. During this transport through solid density plasma, the fast electron beam is subject to various linear and non-linear energy loss mechanisms[17–21] and scattering off background electrons and ions that can significantly increase beam divergence and reduce the amount of energy deposited in the fuel. Many experiments have investigated transport through solid materials [22–25]. Most of these, however, do not go into detail about the magnetic field development and its effects on transport but rather focus on quantifying beam divergence, electron conversion efficiency and temperature, and electron stopping lengths.

Involved in the physics of all these processes is the cone tip material. Different materials have different densities, heat capacities and ionization potentials that affect preplasma formation (and therefore laser absorption physics) and transport physics (via resistivity evolution, for example) that will change the final energy spectrum, beam density and divergence as it arrives the compressed fuel. The main goal of this thesis, therefore, is to describe experimental and computational investigations of how different cone tip materials affect the transport of relativistic electron beams.

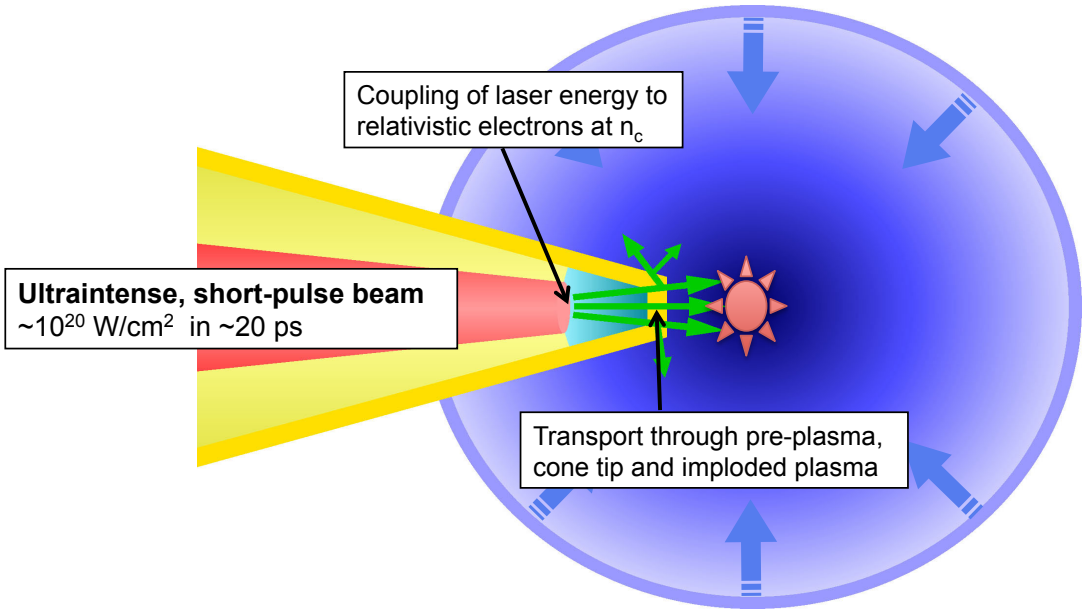

Figure 1.6: Cross-section of cone-capsule configuration. The ignitor pulse is directed through the cone and interacts with the pre-plasma near the critical density, creating fast electrons that travel through the cone tip and to the compressed fuel. Figure courtesy of P.K. Patel, LLNL.

1.4 Outline of Dissertation

Chapter 2 introduces basic plasma concepts, laser-plasma interaction physics and electron transport physics. Dominant laser absorption mechanisms and fast electron source temperature scalings are discussed. In addition, details of fast electron stopping and scattering, radiation production and plasma resistivity models are provided.

Chapter 3 introduces three plasma simulation codes used to model various stages of a laser-plasma experiment. Brief descriptions of HYDRA (hydrodynamic code for pre-plasma modeling) and PICLS (particle-in-cell (PIC) code for laser-plasma interaction modeling) are given with the main physics models used by each code. The majority of the chapter is dedicated to the details of the ZUMA, a hybrid-PIC code used to model the transport of relativistic electrons through solid materials. All of the code's major subroutines are described, as well as physics, diagnostic, and benchmarking development done by the author.

Chapter 4 provides an overview of the Titan Laser System at LLNL that was used to

conduct the main experiment of this work. Laser diagnostics and major experimental diagnostics used to characterize the laser-plasma interaction and fast electron transport are described with detailed descriptions of data analysis methods.

Chapter 5 describes an experiment that investigated the effect of target material on fast-electron transport. The Titan Laser irradiated multilayered solid Al targets with embedded transport (Au, Mo, Al) and tracer (Cu) layers. Kα diagnostics consistently detected a more collimated electron beam in high- or mid-Z (Au or Mo) transport targets compared to Al transport targets. All targets showed a similar electron flux level in the central spot of the beam. Two-dimensional collisional particle-in-cell simulations showed formation of strong self-generated resistive magnetic fields in targets with a high-Z transport layer that suppressed the fast-electron beam divergence; the consequent magnetic channels guided the fast electrons to a smaller spot, in good agreement with experiments.

Chapter 6 reports results of a computational investigation using the ZUMA code to explore in greater detail the physics of electron transport in various materials. More specifically, fast electron deposition mechanisms are examined for various electron energy ranges as a function of time. Magnetic field evolution is examined spatially and temporally and the origins of magnetic field growth are shown to be dominated by material resistivity, temperature and ionization state evolution. Implications for cone tip design are discussed.

Chapter 7 summarizes and concludes the work.

1.5 Role of Author

In Chapter 5, the author was responsible for the planning, setup and execution of the experiment. The author performed the target positioning and alignment, laser focal spot optimization and setup of the DCHOPG spectrometer. The author managed diagnostic data collection during the experiment and analyzed all of the data from the Kα diagnostics described in

Chapter 4. The Kα imager setup was performed by Alessio Morace and Charlie Jarrott and the equivalent plane monitor setup and analysis by Tony Link. The bremmstrahlung spectrometer data was analyzed by Brad Westover.

The author performed the HYDRA simulations and the PICLS simulations were performed by Rohini Mishra, with additional post processing of the results done by the author in MATLAB. The author was involved in ZUMA physics package, diagnostic and benchmarking code development as described in Chapter 3. In Chapter 6, the author designed and executed all ZUMA simulations and developed the analysis codebase in Python and MATLAB.

Chapter 2

Physics of Laser Plasma Interactions and Electron Transport

2.1 Basic Plasma Physics

We begin by describing some basic plasma parameters. For a test charge in a singly ionized plasma, Poisson's equation is

$$\nabla^2 \varphi = -4\pi \, [Q\delta(\vec{r}) - e(n_e - n_i)], \tag{2.1}$$

where Q is the test particle charge, n_e and n_i are the plasma electron and ion densities, respectively, and e is electron charge. If we assume a Boltzmann distribution ($n_{e,i}(\vec{r}) = n_{e0,i0}\, e^{\frac{e\varphi}{k_B T}}$) for the densities and linearize (assuming a weakly correlated plasma, i.e. $\frac{e\varphi}{k_B T} \ll 1$), to 1st order we have

$$n_e \approx \; n_{e0}(1 - \frac{e\varphi}{k_B T}) \; , \; n_i \approx \; n_{i0}(1 - \frac{e\varphi}{k_B T}). \tag{2.2}$$

Substituting in these expressions in Eq. 2.1 gives

$$\nabla^2\varphi = -4\pi Q\delta(\vec{r}) + \frac{2}{\lambda_D^2}\varphi, \tag{2.3}$$

where we have defined $\lambda_D = \sqrt{\frac{k_B T}{4\pi\bar{n}_0 e^2}}$ and $\bar{n}_0 = (n_{e0} + n_{i0})/2$. Recall the Fourier transform of φ is

$$\tilde{\varphi}(\vec{k}) = \iiint \frac{d^3\vec{r}}{(2\pi)^3}\, e^{-i\vec{k}\cdot\vec{r}}\, \varphi(\vec{r}). \tag{2.4}$$

Applying this to Eq. 2.3 and assuming the test charge is located at $\vec{r} = 0$, we have

$$(k^2 + \frac{2}{\lambda_D^2})\tilde{\varphi} = 4\pi Q. \tag{2.5}$$

The solution for φ can be obtained by applying the inverse Fourier transform to $\tilde{\varphi}$ and solving the $\vec{k}_r$ integral using Cauchy's Theorem. The result is

$$\varphi = \frac{Q}{\vec{r}}\, e^{-\sqrt{2}\vec{r}/\lambda_D}. \tag{2.6}$$

The potential of point charge in a plasma is simply that of one in vacuum screened spatially by the surrounding plasma over a scale length of λ_D, known as the Debye length. The characteristic electron plasma frequency is then just

$$\omega_{pe} = \bar{v}_e/\lambda_D = \sqrt{4\pi n_e^2/m_e}, \tag{2.7}$$

where $\bar{v}_e = \sqrt{k_B T_e/m_e}$ is the electron thermal velocity and T_e and m_e are the electron temperature and mass.

The dispersion relation for an electromagnetic wave propagating in a plasma is

$$k^2c^2 = \omega_0^2 - \omega_{pe}^2, \tag{2.8}$$

where k and ω_0 and the wavenumber and frequency of the EM wave. For frequencies less than the plasma frequency the wavenumber becomes imaginary and light cannot propagate in the plasma. For a given frequency of light, then, the plasma density at which that light will be reflected is known as the critical density and is defined as

$$n_{crit} \equiv \frac{m_e \omega_0^2}{4\pi e^2}. \tag{2.9}$$

The frequency of interest in this work is 1054 nm, that of the Titan Laser System used in the experiment described in Chapter 5, and has associated with it an approximate critical density of 10^{21} cm^{-3}.

2.2 Laser Plasma Interactions

The physics of laser-plasma interactions is a rich and complex area. Here we describe the main mechanisms dealing with laser light absorption by plasma in underdense (inverse bremmstrahlung absorption) and overdense (resonance absorption, J x B heating) plasma, relativistic electron generation and relevant scaling laws of generated electrons in the FI and sub-FI regimes.

2.2.1 Ponderomotive Force

The equation of motion of a single electron oscillating in the center of a focused laser beam in the non-relativistic case ($\beta \ll 1$) is

$$m\frac{d\mathbf{v}}{dt} = -e\left[\mathbf{E}(\mathbf{r}) + \frac{\mathbf{v}\times\mathbf{B}(\mathbf{r})}{c}\right], \tag{2.10}$$

where we can assume the electric field vector of the laser light has a spatial dependence of the form

$$\mathbf{E} = \mathbf{E_0}(\mathbf{r})\cos(\omega_0 t). \tag{2.11}$$

If we write the electron velocity as a sum of first and second order terms, $\mathbf{v} = \mathbf{v}_1 + \mathbf{v}_2$, and consider the instantaneous equilibrium position of the electron, then the magnetic field term vanishes. In the first order, then, at initial position $\mathbf{r_0}$ we have

$$m\frac{d\mathbf{v_1}}{dt} = -e\mathbf{E}(\mathbf{r_0}) \tag{2.12}$$

$$\implies \frac{d\mathbf{r_1}}{dt} = \mathbf{v_1} = -\frac{e}{m\omega_0}\mathbf{E_0}(\mathbf{r_0})\sin(\omega_0 t) \tag{2.13}$$

$$\implies \mathbf{r_1} = \frac{e}{m\omega_0^2}\mathbf{E_0}(\mathbf{r})\cos(\omega_0 t). \tag{2.14}$$

Given $\mathbf{r_1}$, we can perform the calculation in second order. Taylor expanding the electric field around $\mathbf{r_0}$ yields

$$\mathbf{E}(\mathbf{r}) = \mathbf{E}(\mathbf{r_0}) + (\mathbf{r_1}\cdot\nabla)\mathbf{E}|_{\mathbf{r}=\mathbf{r_0}} + \cdots \tag{2.15}$$

The equation of motion, now including the magnetic field term, is

$$m\frac{d\mathbf{v_2}}{dt} = -e\left[(\mathbf{r_1}\cdot\nabla)\mathbf{E} + \frac{\mathbf{v_1}\times\mathbf{B_1}(\mathbf{r})}{c}\right]. \tag{2.16}$$

Integrating Faraday's law, $\partial\mathbf{B}/\partial t = -c\nabla\times\mathbf{E}$, gives an expression for the magnetic field we can use to write $\mathbf{B_1}$:

$$\mathbf{B_1} = \frac{c}{\omega_0}\nabla\times\mathbf{E_0}|_{\mathbf{r}=\mathbf{r_0}}\sin(\omega_0 t). \tag{2.17}$$

Substituting expressions for $\mathbf{B_1}$, $\mathbf{v_1}$ and $\mathbf{r_1}$ into Eq. 2.16 and averaging over the laser period gives

$$\begin{aligned}\mathbf{F_p} = m\left\langle\frac{d\mathbf{v_2}}{dt}\right\rangle &= -\frac{1}{2}\frac{e}{m\omega_0^2}[(\mathbf{E_0}\cdot\nabla)\mathbf{E_0} + \mathbf{E_0}\times(\nabla\times\mathbf{E_0})] \\ &= -\frac{1}{2}\frac{e}{m\omega_0^2}\nabla < \mathbf{E_0^2}(\mathbf{r}) > \\ &= -\frac{e^2}{4m\omega_0^2}\nabla\mathbf{E_0^2}.\end{aligned} \tag{2.18}$$

Thus the ponderomotive force acts to push electrons away from regions of high intensity (since

$\mathbf{I} \propto \mathbf{E^2}$).

2.2.2 Inverse Bremmstrahlung Absorption

Also known as collisional absorption, this is the process by which laser light is transferred to plasma electrons via collisions[26]. The rate of energy transfer can be obtained by calculating the average power dissipated by the light wave per unit volume of the plasma by the Joule effect,

$$P = \langle \mathbf{j} \cdot \mathbf{E} \rangle = \frac{1}{2} \Re(\mathbf{j}^* \cdot \mathbf{E}), \tag{2.19}$$

where $\mathbf{j}^*$ is the complex conjugate of the current density $\mathbf{j} = -i\omega\varepsilon_0\chi_e\mathbf{E}$, ω is the laser frequency, and χ_e is the plasma electron susceptibility given by

$$\chi_e(\omega) = -\frac{\omega_{pe}^2}{\omega(\omega + i\nu_{ei})}. \tag{2.20}$$

Substituting for $\mathbf{j}^*$, we have

$$P = \frac{1}{2}\omega\varepsilon_0 \Im(\chi_e)|\mathbf{E}|^2 = \omega\varepsilon_0 \Im(\chi_e)\langle \mathbf{E}^2 \rangle, \tag{2.21}$$

and then using Eq. 2.20 we get

$$P = \nu_{ei}\frac{\omega_{pe}^2}{\omega^2 + \nu_{ei}^2}\varepsilon_0 \Im(\chi_e)\langle \mathbf{E}^2 \rangle \simeq \nu_{ei}\frac{\omega_{pe}^2}{\omega^2}\varepsilon_0\langle \mathbf{E}^2 \rangle \tag{2.22}$$

Thus inverse bremmstrahlung absorption is most effective for large scale length, under dense plasmas. It heats the main body of the electron distribution function, evident by the fact $\nu_{ei} \sim v^{-3}$.

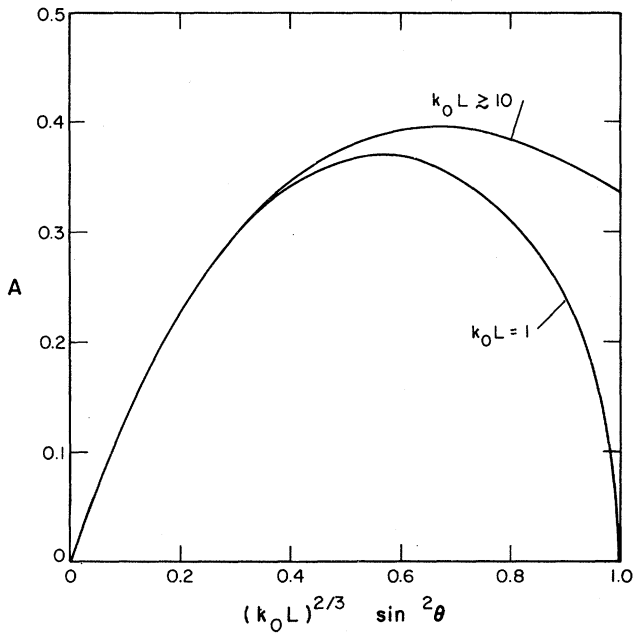

Figure 2.1: Power absorption coefficient A as a function of incidence angle θ and density gradient scale length L. Figure taken from Freidberg[4].

2.2.3 Resonance Absorption

The electric field component of laser light can excite plasma oscillations at the plasma critical density if the light is p-polarized and obliquely incident on the plasma density gradient. Given an incidence angle of θ, light will be reflected at $n_{crit}\ \cos^2\theta$, known as the classical turning point. p-polarization of the light is necessary so $\mathbf{E}\cdot\nabla \neq 0$, allowing the electric field can excite electrons at the critical density and resonantly drive electron-plasma (Langmuir) waves. Freidberg[4] found that a maximum absorption of $\sim 50\%$ could be achieved with an incidence angle given by

$$(k_0L)^{2/3}\sin^2(\theta_{opt}) \simeq (\frac{1}{2})^{2/3}, \tag{2.23}$$

where k_0 is the laser vacuum wavenumber, L is the distance over which the plasma density rises linearly from $\omega_{pe} = 0$ to $\omega_{pe} = \omega_0$, and θ_{opt} is the optimal incidence angle. Figure 2.1 shows how absorption varies with incidence angle for two different values of k_0L. The absorbed

energy excites a population of energetic electrons that form a non-Maxwellian tail on the plasma electron velocity distribution. Forslund, et. al performed simulations that the temperature, T, of these energetic electrons scales as

$$T \approx 10[T_{keV} I_{15} \lambda_{\mu}^2]^{1/3}\ keV, \tag{2.24}$$

where T_{keV} is the background electron temperature in keV, I_{15} is the laser intensity normalized by 10^15 W/cm^2, and λ_{μ}^2 is the laser wavelength in microns.

Resonance absorption will dominate over inverse bremsstrahlung absorption at high laser intensities. This is because high laser intensities will create high plasma temperatures, and since the electron-ion collision frequency is inversely proportional to temperature ($\nu_{ei} \propto T_e^{-3/2}$), high temperatures imply smaller collision frequencies and thus less collisional absorption.

2.2.4 J x B Heating

The electron equation of motion for a plasma fluid element is

$$\frac{\partial \mathbf{p}}{\partial t} + \mathbf{v} \cdot \nabla \mathbf{p} = -e \left[\mathbf{E} + \frac{\mathbf{v} \times \mathbf{B}}{c} \right], \tag{2.25}$$

where $\mathbf{p} = \gamma m \mathbf{v}$. Rewriting this in terms of the vector potential ($\mathbf{B} = \nabla \times \mathbf{A}$) and the electrostatic potential ($\mathbf{E} = -\frac{1}{c}\frac{\partial \mathbf{A}}{\partial t} - \nabla \phi$), we have

$$\frac{\partial \mathbf{p}}{\partial t} + \frac{\mathbf{p} \cdot \nabla \mathbf{p}}{\gamma m} = -e \left[\left(-\frac{1}{c}\frac{\partial \mathbf{A}}{\partial t} - \nabla \phi \right) + \frac{\mathbf{p} \times \nabla \times \mathbf{A}}{\gamma m c} \right]. \tag{2.26}$$

Decomposing the momentum into transverse and longitudinal components, $\mathbf{p} = \mathbf{p}_t + \mathbf{p}_L$, and assuming $\mathbf{A}$ has only a transverse component that varies in the longitudinal ($\hat{z}$) direction, we

have

$$\frac{\partial}{\partial t}\left(\mathbf{p}_t - \frac{e}{c}\mathbf{A}\right) + \frac{\mathbf{p}_L}{\gamma m}\frac{\partial}{\partial z}\left(\mathbf{p}_t - \frac{e}{c}\mathbf{A}\right) = 0, \tag{2.27}$$

implying that the transverse momentum has the form

$$\mathbf{p}_t = \frac{e}{c}\mathbf{A}. \tag{2.28}$$

The longitudinal part of Eq. 2.26 is

$$\frac{\partial p_L}{\partial t} + \frac{\mathbf{p}\cdot\nabla\mathbf{p}}{\gamma m} = e\nabla\phi - \frac{e}{\gamma mc}\frac{\mathbf{p}\times\nabla\mathbf{A}}{\gamma mc}, \tag{2.29}$$

which simplifies to

$$\frac{\partial p_L}{\partial t} = e\nabla\phi - m_0c^2\nabla(\gamma - 1), \tag{2.30}$$

where $\gamma = \sqrt{(1+a_0^2)}$ for circularly polarized light and $\gamma = \sqrt{(1+a_0^2/2)}$ for linearly polarized light. The first term on the RHS is simply the standard electrostatic force and the second term is the relativistic ponderomotive force with potential

$$U_p = (\gamma - 1)m_0c^2. \tag{2.31}$$

a_0 is known as the *normalized momentum* and is used often in calculations related to high intensity laser-plasma interactions. In the oscillating field of a laser, the transverse electric field will cause electrons to oscillate with quiver velocity v_{osc}. Then

$$a_0 = \frac{p_{osc}}{m_ec} = \frac{\gamma v_{osc}}{c} = \frac{eE_0}{m_ec\omega_0} = \sqrt{\frac{I\lambda_{\mu m}^2}{1.37\times10^{18}(W/cm^2)}} \tag{2.32}$$

where p_{osc} is the quiver momentum, I is the laser intensity and $\lambda_{\mu m}$ is the laser wavelength in μm. The normalization factor of 1.37×10^{18} is chosen such that when $a_0 < 1$, the ponderomo-

tive force of the laser accelerates electrons electrons in the perpendicular direction over many microns. When $a_0 > 1$, the laser magnetic field becomes non-negligible and the electrons can be accelerated longitudinally by the $\mathbf{j} \times \mathbf{B}$ force described above. The energy gained by electrons due to this force thus scales according to the ponderomotive potential, yield an electron "temperature"[27] of

$$T_{hot} \approx \left(\sqrt{1 + \frac{I\lambda_{\mu m}^2}{1.37 \times 10^{18}}} - 1 \right) \text{ 511 keV} \tag{2.33}$$

for circularly polarized light (2.8×10^{18} for linearly polarized light).

2.2.5 Electron Source Characterization

Experimental and computational characterization and analysis of the electron source produced in a high-intensity relativistic laser-plasma interactions is an extensive area research in the FI community. Numerous experimental studies inferring electron sources from fast electron-produced bremmstrahlung and Kα emission data[24, 28–30] and simulations of laser-plasma interactions[27, 31–33] have described electron source angular distributions, energy distributions and hot electron temperature scaling models as a function of laser intensity.

At laser intensities above 10^{19} W/cm^2 (the regime of interest in this work), Wilks [27] ponderomotive scaling due to the $\mathbf{j} \times \mathbf{B}$ force dominates, and Beg[28] empirically found that a scaling of

$$T_{hot} \approx \left(\frac{I\lambda_{\mu m}^2}{10^{17}} \right)^{1/3} \text{ 100 keV} \tag{2.34}$$

holds true for intensities below 10^{19} W/cm^2. At $\sim 10^{20}$ W/cm^2 (the intensity of the experiment and most simulations described in this work), these scaling models agree within a factor of 2. Many works like this assume a Mawellian energy distribution of the form

$$f(E) \approx E^{1/2} exp(-E/T_{hot}), \tag{2.35}$$

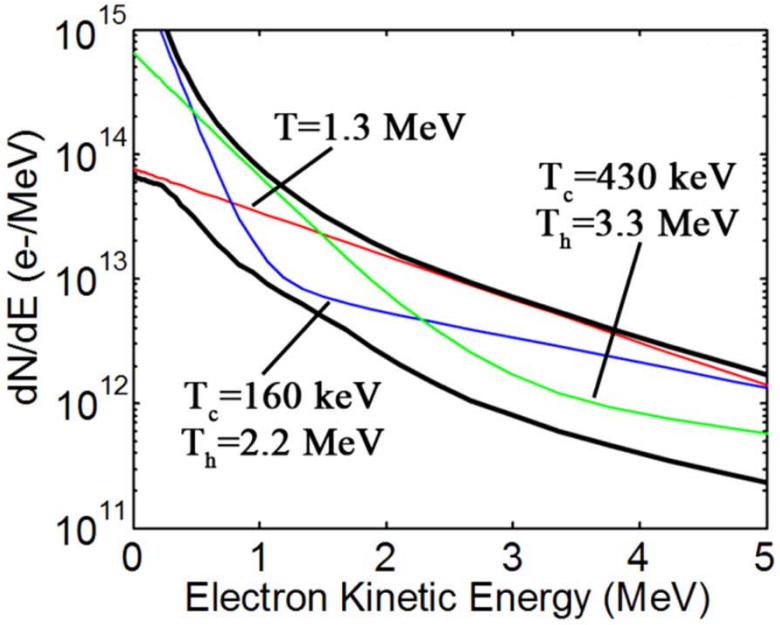

Figure 2.2: Various 2-temperature electron energy spectra consistent with bremmstrahlung and Kα emission data from an experiment in which 1 mm^3 metal targets were irradiated with laser pulses with intensities between 3×10^{18} and 8×10^{19} W/cm^2. A 1-temperature distribution is shown in red for reference, two sample 2-temperature distributions shown in green and blue while the black lines represent the envelope of these curves. Figure taken from Chen[30].

however recent experimental and computational studies[29–31] have show 2-temperature distributions of the form

$$f(E) \approx \ f_1(E)exp(-E/T_{hot,1}) + f_2(E)exp(-E/T2_{hot,2}) \tag{2.36}$$

to be more accurate (see Fig. 2.2). In general, accurately determining an electron source model $f(E,\theta,t)$ is rather complex and, as the purpose of this work is to study transport, it suffices to use a Mawellian distribution for electron energy with a time-varying angular distribution and hot electron temperature determined by detailed laser-plasma simulations, as will be described in Chapters 3 and 6.

2.2.6 Classical Ejection Angle

In the non-relativistic regime, electron motion is perpendicular to the laser wave vector. This is not the case in the relativistic regime. We will derive a simple model of electron motion assuming a plane wave, more specifically the angle of velocity with respect to the propagation axis of the wave[5].

First consider a free electron initially at rest in the field of an electromagnetic laser pulse for which we assume a plane wave structure propagating in vacuum. The laser pulse is described by its vector potential $\mathbf{A}(\mathbf{r},t)$. Let x be the propagation direction, so $\mathbf{A}$ is directed in the yz plane and depends only on $x-ct$. The relativistic equation of motion is then

$$\frac{d\mathbf{p}}{dt} = -e(\mathbf{E} + \mathbf{v} \times \mathbf{B}), \tag{2.37}$$

where $\mathbf{p} = m_e\gamma\mathbf{v}$ and we can write the Lorentz factor as

$$\gamma = \sqrt{1 + \frac{p^2}{m_e^2c^2}}. \tag{2.38}$$

If we express the electric and magnetic fields in terms of the vector potential

$$\mathbf{E} = -\frac{\partial \mathbf{A}}{\partial t} \tag{2.39}$$

$$\mathbf{B} = \nabla \times \mathbf{A}, \tag{2.40}$$

then we can write the equation of motion as

$$\frac{d}{dt}(\mathbf{p} - e\mathbf{A}) = -e(\nabla \mathbf{A}) \cdot \mathbf{v}. \tag{2.41}$$

The corresponding energy equation then reads

$$\frac{d}{dt}\gamma m_e c^2 = -e\mathbf{v} \cdot \frac{\partial \mathbf{A}}{\partial t}. \tag{2.42}$$

The transverse part of Eq. 2.41 gives

$$\mathbf{p}_\perp = e\mathbf{A} \tag{2.43}$$

$$\mathbf{v}_\perp = \frac{e\mathbf{A}}{m_e \gamma}. \tag{2.44}$$

Inserting this result in the longitudinal part of Eq. 2.41 and in Eq. 2.42 yields

$$\begin{aligned} \frac{dp_x}{dt} &= -\frac{e^2}{2m_e\gamma}\frac{\partial A^2}{\partial x} \\ \frac{d}{dt}\gamma m_e c^2 &= \frac{e^2}{2m_e\gamma}\frac{\partial A^2}{\partial t} \\ \implies \frac{d}{dt}(\gamma m_e c^2 - p_x c) &= \frac{e^2}{2m_e\gamma}\left(\frac{\partial}{\partial t} + c\frac{\partial}{\partial x}\right)A^2. \end{aligned} \tag{2.45}$$

For an EM plane wave propagating in vacuum towards $x\,0$, $\mathbf{A}$ is a function of $x - ct$ so

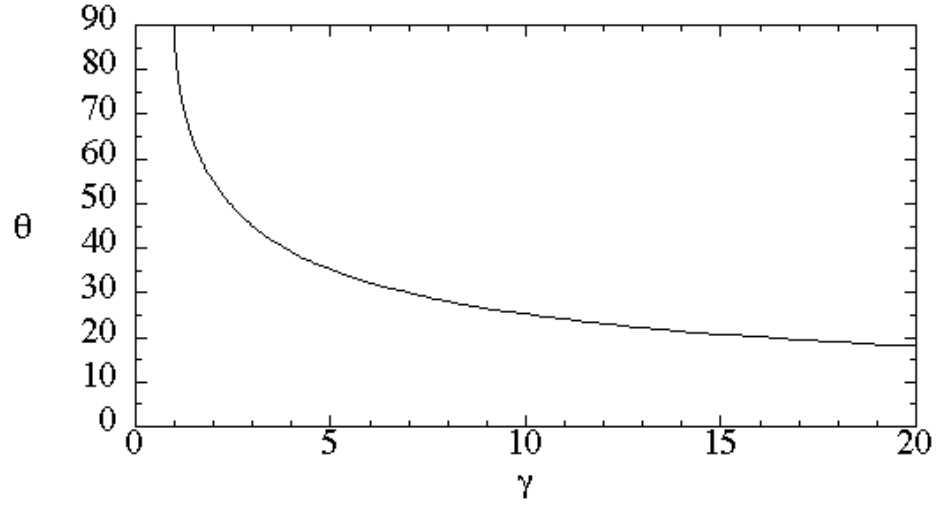

Figure 2.3: Angle of electron velocity with respect to wave propagation axis as a function of Lorentz factor. Figure taken from Mora[5].

the RHS of Eq. 2.45 vanishes. Thus for an electron initially at rest

$$\gamma m_e c^2 - p_x c = \gamma m_e c^2$$

or

$$\gamma = 1 + \frac{p_x}{m_e c}. \tag{2.46}$$

Combining this result and Eq. 2.38, we obtain

$$\frac{p_x}{m_e c} = \frac{1}{2}\left(\frac{\mathbf{p}_\perp}{m_e c}\right)^2. \tag{2.47}$$

Now that we have an expression for p_x in terms of $\mathbf{p}_\perp$, we can easily write down an expression for the angle of the velocity with respect to the x-axis (see Fig. 2.3) as

$$\tan\theta = \left(\frac{2}{\gamma - 1}\right)^{1/2}. \tag{2.48}$$

2.3 Relativistic Electron Beam Transport

The focus of this thesis is on the transport of relativistic electron beams through solid density plasma. In this section, detailed descriptions are presented of energy loss (radiative and collisional) and scattering models of fast electrons as they propagate through plasma as well as plasma resistivity models relevant to the evolution of the background plasma during transport. Nonlinear phenomena of relativistic beam transport are also discussed.

2.3.1 Collective Stopping

In the laser-plasma interactions relevant to this work, large currents of relativistic (or fast) electrons are generated. The current rapidly ionizes the background target material creating a plasma with resistivity η. In order to propagate, Bell, et al., note that a background plasma must supply a "return" current[34] to maintain charge neutrality such that

$$j_{total} = j_{fast} + j_{return} \cong 0. \tag{2.49}$$

The electrons constituting j_{return} will be moving slowly as compared to the fast electrons, and will be slowed by the background resistivity. Because of this non-instantaneous charge neutralization, a resistive electric field $E = \eta j_{return} = -\eta j_{fast}$ will form that directly opposes fast electrons. The fast electrons will then decelerate and deposit part of their energy into the background in a process known as ohmic stopping.

The continuity equation for fast electrons combined with Eq. 2.49 gives

$$\frac{\partial n}{\partial t} = \nabla \cdot \left(\frac{j_{fast}}{e} \right) = -\nabla \cdot \left(\frac{\sigma E}{e} \right) \tag{2.50}$$

where $j_{return} = \sigma E$ and σ is the background plasma conductivity. Assuming a Maxwellian distribution for the fast electrons and that they are confined by the electric field, $E = -\nabla\phi$, the

fast electron number density $n \sim \exp(\phi/T_0)$ giving

$$E = -\frac{T_0}{n}\nabla n. \tag{2.51}$$

Substituting this into Eq. 2.50 gives

$$\frac{\partial n}{\partial t} = \nabla \cdot \left(\frac{\sigma T_0}{en} \nabla n \right). \tag{2.52}$$

This is a diffusion equation with coefficient $D = \sigma T_0/en$, which is inversely proportional to fast electron density.

Given some crude assumptions (constant fast electron temperature during laser pulse, constant and uniform conductivity, system is 1D function of z which is the distance from the front target surface), Eq. 2.52 has a solution of the form

$$n = n_0 \left(\frac{t}{\tau_{las}} \right) \left(\frac{z_0}{z + z_0} \right)^2 \tag{2.53}$$

where

$$n_0 = \frac{2 I_{abs}^2 \tau_{las}}{9 e T_{hot}^3 \sigma} \tag{2.54}$$

and

$$z_0 = \frac{3 T_0^2 \sigma}{I_{abs}}. \tag{2.55}$$

I_{abs} is the absorbed laser intensity, τ_{las} is the laser pulse duration, and z_0 is the ohmic stopping scale-length, which is the distance over which the potential change equals the fast electron mean energy. Thus, as laser intensity increases, conversion efficiency increases (because n_0 is proportional to I_{abs}^2) but penetration depth decreases.

2.3.2 Collisional Stopping and Scattering

Expressions for the stopping power, scattering coefficients and range of fast electrons in dense plasmas typical of fusion targets was were derived by Solodov and Betti[35] and Atzeni, Schiavi and Davies[36] and we follow their derivations here.

The drag of a relativistic, or fast, electron in a plasma can be written as

$$\frac{dp}{dt} = -\frac{D}{v^2} L_d \tag{2.56}$$

where $D = n_e e^4 / 4\pi\varepsilon_0^2 m_e$, n_e is the is the background free electron density and

$$L_d|_{W\rangle W_c} = \frac{n_e v^2}{D} \int_{\varepsilon_c}^{K/2} \varepsilon \frac{\partial \sigma}{\partial \varepsilon} d\varepsilon. \tag{2.57}$$

Here σ is the binary collision cross section, ε_c is lower energy exchange cutoff from the binary collision model and $K/2$ is the maximum energy exchange of a fast electron with energy K. Applicability of the binary collision model requires the de Broglie wavelength of the fast electron to be much less than the electron separation, i.e. $p \gg \hbar n_e^{1/3}$. This implies fast electron energies much greater than a few eV, which is a valid assumption for this work.

Moller[37] derived an analytic expression for the cross section,

$$\frac{\partial \sigma}{\partial \varepsilon} = \frac{e^2}{8\pi\varepsilon_0^2 m_e v^2} \left[\frac{1}{\varepsilon^2} + \frac{1}{(K-\varepsilon)^2} + \left(\frac{\gamma - 1}{\gamma K} \right)^2 - \frac{2\gamma - 1}{\gamma^2 \varepsilon (K - \varepsilon)} \right], \tag{2.58}$$

given in the lab frame of the target electron. Inserting Eq. 2.58 into Eq. 2.57 neglecting terms of order ε_c / K yields

$$L_d|_{W>W_c} = \ln \sqrt{\frac{K}{\varepsilon_c}} + \frac{9}{16} - \ln 2 + \frac{(1/2)\ln 2 + 1/16}{\gamma^2} - \frac{\ln 2 + 1/8}{\gamma}. \tag{2.59}$$

Collective effects due to the energy exchange of fast electrons with distant background electrons

uses a model that assumes a small perturbation of the background caused by a charge particle with constant velocity. This is separated into 2 parts: a transverse component due to the oscillation of background electrons (Bethe) and a longitudinal component due to the polarization of the background (density effect correction), which lowers the stopping power. Because of the complexity of these calculations, we write down the sum of these 2 terms as

$$L_d|_{W<W_c} = \ln\frac{\sqrt{2m_e v^2 W_c}}{\hbar\omega_p}, \tag{2.60}$$

where ω_p is the plasma frequency of background electrons. This results applies to the contribution from background bound electrons for sufficiently fast electrons, implying that all materials look like plasmas given an electron fast enough. The exact condition that must be satisfied is $\sqrt{2m_e v^2 W_c} > \hbar\omega_p$ (for a compressed DT $\hbar\omega_p$ is only 370 eV). Summing Eqs. 2.59 and 2.60 gives

$$L_d = \ln\frac{\sqrt{m_e v^2 K}}{\hbar\omega_p} + \frac{9}{16} - \ln 2 + \frac{(1/2)\ln 2 + 1/16}{\gamma^2} - \frac{\ln 2 + 1/8}{\gamma}. \tag{2.61}$$

Note the arbitrary energy cutoff has cancelled out, assuming that it is much less than the fast electron's energy. Equation 2.61 is independent of the temperature and binding energy of background electrons, and background material.

To determine the coefficient of scattering, consider the mean squared rate of deflection of a fast electron

$$\langle\theta^2\rangle = \frac{2ZmeD}{p^2 v} L_s, \tag{2.62}$$

where Z is the atomic number of the scattering particle. Using a similar approach as before, we can calculate the scattering of the fast electron by nearby background particles using a binary collision model, yielding

$$\langle\theta^2\rangle|_{\theta>\theta_c} = 2\pi n_b v \int_{\theta_c}^{\theta_{max}} \theta^2 \frac{\partial\sigma}{\partial\Omega} \sin\theta d\theta, \tag{2.63}$$

where n_b is the number density of background particles, Ω is the solid angle, θ_c is a lower cutoff of the scattering angle from the binary collision model and θ_{max} is the maximum scattering angle, which is π for ions or atoms and $\sin^{-1}\sqrt{2/(\gamma+3)}$ for electrons, due to the maximum energy exchange of $K/2$. For angles below θ_c (i.e. the treatment of background particles farther away than λ_D), a screened potential is used with the binary collision model..

The relativistic differential cross section for fast electrons scattering off plasma ions with charge number Z is

$$\frac{d\sigma}{d\Omega} = \left(\frac{b_{0i}}{2\sin^2(\theta/2)}\right)^2 \left(\frac{\Lambda_Q^2 \sin^2(\theta/2)}{1+\Lambda_Q^2 \sin^2(\theta/2)}\right)^2 \left(1-\beta^2 \sin^2(\theta/2)\right), \tag{2.64}$$

where $b_{0i} = Ze^2/4\pi\varepsilon_0 pv$, $\Lambda_Q^2 = 2\lambda_D p/\hbar$ (p is electron momentum), $\beta = v/c$ and θ is the scattering angle. This result is from the first Born approximation for a shielded potential. The first term is the Rutherford scattering formula, the second term is due to shielding (neglecting this term gives Mott's formula[38]), and the third term is the spin term. Solving this integral will give L_{si}, the ion contribution to the scattering coefficient. It can be determined numerically to be

$$L_{si} \approx \ln\Lambda_Q - 0.234 - 0.659\frac{v^2}{c^2}, \Lambda_Q \gg 1.$$

To determine an expression for fast electron scattering by plasma electrons that takes into account screening, we note that $4p^2\sin^2\theta/2$ is the 4-momentum in the center of mass frame of a fast-plasma electron interaction. For particles of equal mass m, the 4-momentum transfer in the plasma electron frame is $2mW$ and the corresponding term for the plasma electron is $2m(K-W)$. These are invariant Mandelstam variables, and we can write the screening term from Eq. 2.64 as

$$S_U = \left(\frac{2m_e U}{\hbar^2/\lambda_D^2 + 2m_e U}\right)^2, \tag{2.65}$$

where U is W for the fast electron and $K-W$ for the target plasma electron. Using the relation

$$W = K\frac{(\gamma-1)\sin^2\theta}{(\gamma-1)\sin^2\theta+2}. \tag{2.66}$$

we can write the Moller cross section (Eq. 2.58) in terms of scattering angle θ in the laboratory frame as

$$\begin{aligned}\frac{\partial\sigma}{\partial\Omega} &= b_0^2\left[S_W\csc^4\theta + S_{K-W}(\frac{\gamma+1}{2})^2\sec^4\theta\right.\\ &+ \frac{S_W+S_{K-W}}{2}\left(\frac{\gamma^2-1}{\gamma[(\gamma-1)\sin^2\theta+2]}\right)^2\\ &- \left.\sqrt{S_W S_{K-W}}\frac{2\gamma-1}{\gamma^2}\frac{\gamma+1}{2}\sec^2\theta\csc^2\theta\right] \qquad (2.67)\\ S_W &= \left(\frac{\Lambda_Q^2\sin^2\theta}{2(\gamma-1)\sin^2\theta+4+\Lambda_Q^2\sin^2\theta}\right)^2 \qquad (2.68)\\ S_{K-W} &= \left(\frac{\Lambda_Q^2\cos^2\theta}{(\gamma^2-1)\sin^2\theta+2(\gamma+1)+\Lambda_Q^2\cos^2\theta}\right)^2 \qquad (2.69)\end{aligned}$$

Calculating L_{se} from these expressions involves integrals that cannot be solved analytically or give complex results. As such, the limits of high ($\gamma \gg 1$) and low ($\gamma - 1 \ll 4$) fast electron energy are applied and shielding terms are simplified such that only the potential of the target electron is shielded. Numerically solving the integrals and rearranging into a useful working form yields

$$L_{se} = \ln\Lambda_Q - \frac{1}{2}\ln\frac{\gamma+3}{2} - \frac{\ln 2}{2} - \frac{3}{4} + f(\gamma), \Lambda_Q \gg 1, \tag{2.70}$$

where $f(\gamma)$ has to be determined numerically and has been chosen so it goes to zero for strongly

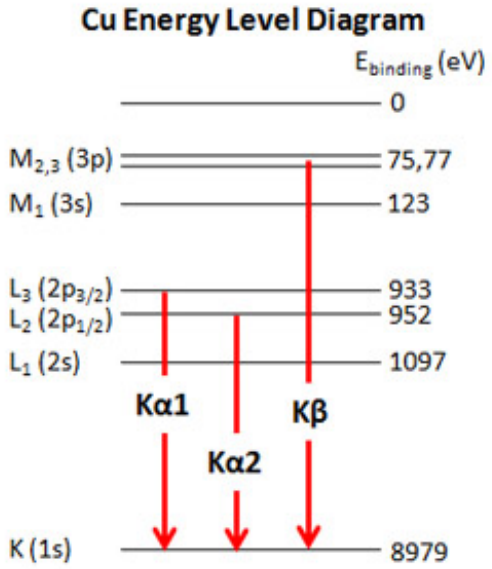

Figure 2.4: Energy diagram of non-ionized copper. Kα1, Kα2 and Kβ emission results from transitions form the L and M shells to the K shell.

relativistic electrons and is always small. It has the following limiting forms

$$f(\gamma) \approx \frac{1}{2}\frac{v^2}{c^2}\left[\ln\frac{2(\gamma+2)}{\gamma+3}-\frac{1}{2}\right]-\frac{\ln 2}{2}+\frac{1}{4}-\frac{2\gamma-1}{2\gamma^2}\frac{\gamma+1}{\gamma+3}, \gamma \gg 1 \tag{2.71}$$

$$f(1) = -0.304 \tag{2.72}$$

2.3.3 K-shell emission

Energetic electrons moving through solid density plasmas can collide with inner shell atomic electrons and eject them from the atom. The resulting vacancy is filled by the transition of an electron from a higher energy state and yields the radiation of a photon with energy given by the difference of beginning and ending energy states of the transferred electron. This process is exploited in FI related experiments to diagnose relativistic electrons moving through solid targets. The energy diagram of non-ionized Cu, a material routinely used as a fluorescence diagnostic material, is shown in Fig. 2.4.

Many classical and quantum mechanical calculations of K-shell ionization cross sections have been made, though none has been fully successful in describing the phenomena over a wide range of atomic numbers Z and overvoltages U, defined as the ratio between the incident electron energy and the ionization energy of the electrons in the K-shell. Hombourger[8] developed empirical expressions describing the cross sections for K-shell ionization of atoms from ionization threshold to high energy of the order of some MeV, and we give his results here.

The cross section is

$$Q_K = n_K \pi a_0^2 G_r \left(\frac{R_y}{E_K}\right)^{C_U} D_U \tag{2.73}$$

where n_K is the number of electrons present in the K-shell, a_0 is the first Bohr radius, R_y is the Rydberg constant, E_K is the threshold energy, D_U is the reduced cross section and C_U is an exponent which depends on U. A relativistic correction factor calculated by Grysinski[39] is given by

$$G_r = \left(\frac{1+2J}{U+2J}\right)\left(\frac{J+U}{J+1}\right)\left(\frac{(1+U)(U+2J)(1+J)^2}{U(2+U)(1+J)^2+J(2J+1)}\right)^{3/2} \tag{2.74}$$

where $J = (mc^2)/E_K$. Polynomial expressions for D_U and C_U are fit using a least-squares interpolation with coefficients given in [8]. A plot for the Cu K-shell ionization cross section given by Eq. 2.73 is shown in Fig. 2.5.

2.3.4 Thomas-Fermi Model

The Thomas-Fermi model is an ion-sphere model of the atom that is used to determine approximate potential fields and charge densities in metals. In the context of this work, it is used to derive the equation of state of matter at high pressures and various temperatures[40].

In Thomas-Fermi theory electrons are treated as a charged fluid surrounding the nucleus with properties obtained from finite-temperature Fermi-Dirac statistics. Consider a sphere of radius $R_0 = (3/4\pi n_i)^{1/3}$ containing an atomic nucleus. Assume the sphere contains enough

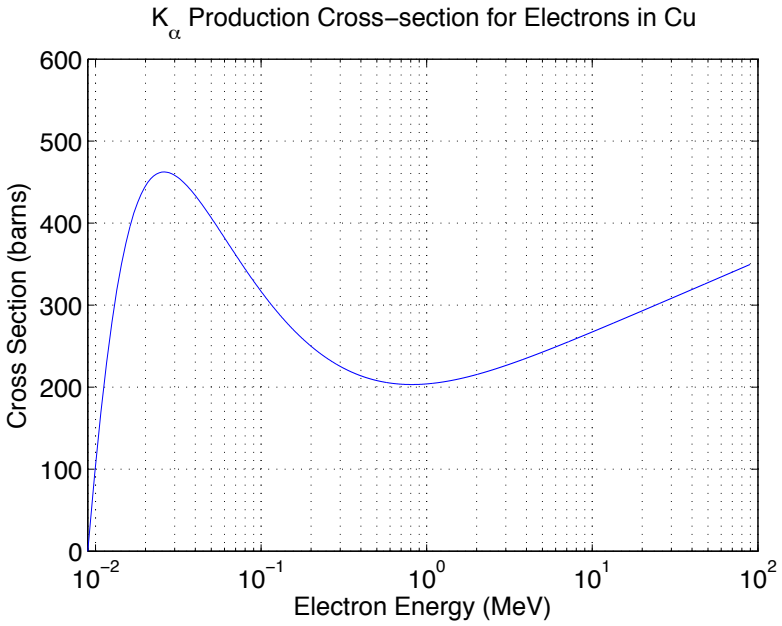

Figure 2.5: Cross section in terms of incident electron energy (MeV) rather than overvoltage U.

electrons be electrically neutral with no other ions. Within the sphere the potential is

$$\nabla^2 V = 4\pi e n(r) - 4\pi Ze\delta(\mathbf{r}), \tag{2.75}$$

where n(r) is the total electron number density including bound and free electrons. At the origin $V(r) \rightarrow Ze/r$, and neutrality of the sphere implies $\partial V/\partial r = 0$ at $r = R_0$. The electron density is determined by the formula for a finite-temperature semiclassical electron gas,

$$n(r) = \int \frac{2d^3p}{h^3} f(r,p) = c_1 (kT)^{3/2} F_{1/2}\left(-\frac{\mu + eV(r)}{kT}\right), \tag{2.76}$$

where

$$f(r,p) = \{1+exp[p^2/2m - eV(r) - \mu]/kT\}^{-1} \tag{2.77}$$

$$c_1 = (1/2\pi^2)(2m/\hbar^2)^{3/2} \tag{2.78}$$

$$F_v(y) = \int_0^\infty \frac{x^v dx}{1+exp(x+y)}. \tag{2.79}$$

Here $f(r,p)$ is the Fermi-Dirac distribution function and the electron chemical potential μ is determined by the by sphere neutrality condition

$$\int n(r) d^3r = Z. \tag{2.80}$$

Given this model, the equations used in constructing thermodynamic functions, such as free energy, entropy, pressure and charge state can then be defined[41].

2.3.5 Resistivity Models

The Spitzer model for electrical resistivity[42] is widely used to describe transport of laser created fast electrons. Consider a fully ionized, non-degenerate collisional plasma. Consider an electron with momentum $p = m_e v$ colliding at a distance b from an ion of charge Zq_e. The scattering angle θ as a function of the distance, or impact parameter, is

$$\tan\left(\frac{\theta}{2}\right) = \frac{Ze^2}{4\pi\varepsilon_0 m v^2 b}, \tag{2.81}$$

where e is the electron charge.

The impact parameter in the large angle limit, $\theta = \pi/2$, is then

$$b = \frac{Ze^2}{4\pi\varepsilon_0 m v^2}. \tag{2.82}$$

Substituting this into the equation for the scattering cross section of the target, $\sigma = \pi b^2$, gives

$$\sigma = \frac{\pi Z^2 e^4}{16\pi^2 \varepsilon_0^2 m^2 v^4}, \tag{2.83}$$

and the collision frequency is then

$$\nu_{ei} = nv\sigma = \frac{\pi n Z^2 e^4}{16\pi^2 \varepsilon_0^2 m^2 v^3}. \tag{2.84}$$

Including small angle scattering (which dominate over large angle scattering in collisional plasmas) adds a $\ln\Lambda$ term to the collision frequency from the integration over all impact parameters $\int_{r_{min}}^{r_{max}} \frac{dr}{r}$. Assuming the Drude model of thermal conductivity and $v = v_{th} = \sqrt{k_B T/m}$, we have then that the resistivity is

$$\eta = \frac{m}{ne^2}\nu_{ei} = \frac{\pi Z e^2 m^{1/2} \ln\Lambda}{16\pi^2 \varepsilon_0^2 (k_B T)^{3/2}}. \tag{2.85}$$

Thus $\eta \sim Z/T^{3/2}$; resistivity increases with ionization state and decreases as temperature rises. Note that as temperature decreases to 0, resistivity goes to infinity. We know that this cannot be accurate because certain metals at room temperature are good conductors. This is a consequence of assuming a collisional, fully ionized plasma.

Lee and More[6] developed an electron conductivity model for dense plasmas with a complete set of transport coefficients including electrical conductivity, thermal conductivity, thermoelectric power, and Hall, Nernst, Ettinghausen, and Leduc-Righi coefficients. The coefficients apply over a wide range of plasma temperature and density and are valid for arbitrarily strong magnetic fields.

In their approach outlined here, different formulas are used for the electron relaxation time in plasma, solid, and liquid phases (see Fig. 2.6). For the solid and liquid phases, the electron map is obtained from the Bloch-Gruneisen theory with a melting formula derived from

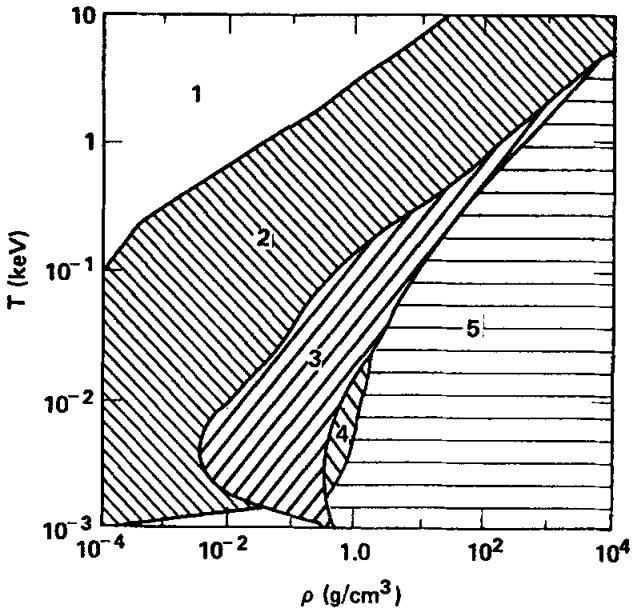

Figure 2.6: Five temperature and density regions where different theories are used to calculate electron relaxation time. Figure taken from Lee[6].

Thomas-Fermi theory. Transport coefficients are obtained from the solution to Boltzmann equation in the relaxation time approximation. The collision operator includes contributions from the scattering of electrons by ions and by neutrals. The electron degeneracy is taken into account by using a Fermi-Dirac distribution for the electrons.

We outline here the derivation of coefficients for the case of a plasma with no magnetic field, weak electric field and small temperature and density gradients as an example. In general, given a 6D electron distribution $f(\mathbf{r},\mathbf{v},t)$, Boltzmann's equation of the form

$$\frac{\partial f}{\partial t}+\mathbf{v}\cdot\frac{\partial f}{\partial \mathbf{r}}-\frac{e}{m}\left(\mathbf{E}+\frac{\mathbf{v}\times\mathbf{B}}{c}\right)\cdot\frac{\partial f}{\partial \mathbf{v}}=\frac{\partial f}{\partial t}|_{coll} \tag{2.86}$$

is satisfied where $\mathbf{E}$ and $\mathbf{B}$ are the electric and magnetic fields, e and m are the electron charge and mass, and c is the speed of light. The collision operator can be written as

$$\frac{\partial f}{\partial t}|_{coll}=-\frac{f-f_0}{\tau_c}, \tag{2.87}$$

where f_0 is a local-equilibrium Fermi-Dirac distribution function depending on electron temperature and density n_e. τ_c is the relaxation time with contributions from electron-ion and electron-neutral scattering giving

$$1/\tau_c = 1/\tau_{ei} + 1/\tau_{en}, \tag{2.88}$$

where $\tau_{ei} = 1/n_i v \sigma_{ei}$ and $\tau_{en} = 1/n_0 v \sigma_{en}$ are the electron-ion and electron-neutral collision rates with n as density and σ as the momentum transfer cross section.

Simplifying to our example case and considering only steady-state transport processes (time derivatives go to 0), Eq. 2.99 becomes

$$\mathbf{v} \cdot \frac{\partial f}{\partial \mathbf{r}} - \frac{e}{m}\mathbf{E} \cdot \frac{\partial f}{\partial \mathbf{v}} = -\frac{f - f_0}{\tau_c}. \tag{2.89}$$

Rewriting this equation in terms of f and letting $\varepsilon = \frac{1}{2}mv^2$, we have

$$f = f_0 - \tau_c \frac{\partial f_0}{\partial \varepsilon} \mathbf{v} \cdot \left(-e\mathbf{E} + \frac{\varepsilon - \mu}{T} \nabla T \right), \tag{2.90}$$

where μ is the chemical potential.

The electrical current, energy flux and heat current are given by

$$\mathbf{j} = -e \int \frac{2d^3p}{h^3} \mathbf{v} f(\mathbf{v}) \tag{2.91}$$

$$\mathbf{Q}_\varepsilon = \int \frac{2d^3p}{h^3} \frac{mv^2}{2} \mathbf{v} f(\mathbf{v}) \tag{2.92}$$

$$\mathbf{Q} = \mathbf{Q}_\varepsilon + \frac{1}{e}\left(\frac{\mu}{T} - \frac{\partial \mu}{\partial T} \right) \mathbf{j} \tag{2.93}$$

Using Eq. 2.90, $\mathbf{j}$ and $\mathbf{Q}$ become linear functions of the temperature gradient and electric field:

$$\mathbf{j} = \sigma(\mathbf{E} - S\nabla T) \tag{2.94}$$

$$\mathbf{Q} = TS\mathbf{j} - K\nabla T, \tag{2.95}$$

where σ is the electrical conductivity, K is the thermal conductivity and S is the thermoelectric power. These coefficients can be obtained by substituting Eq. 2.90 into Eqs. 2.91 and 2.92, yielding

$$\sigma = e^2 K_0 \tag{2.96}$$

$$K = (1/T)(K_2 - K_1^2/K_0) \tag{2.97}$$

$$S = \frac{1}{e}\left(\frac{\mu}{T} - \frac{\partial \mu}{\partial T}\right) - \frac{K_1}{eTK_0}, \tag{2.98}$$

where

$$K_n = -\int \tau_c \, \frac{v^3}{3} \, \varepsilon^n \, \frac{\partial f_0}{\partial \varepsilon} \, \frac{2d^3p}{h^3}. \tag{2.99}$$

Calculation of the coefficient integrals requires knowledge of the momentum transfer cross sections. Lee and More found the Coulomb cross section with appropriate cut-off parameters can give a good approximation to numerical calculations of cross sections using partial wave theory. For the Coulomb logarithm, the maximum impact parameter is determined by screening as described by Debye theory. Lee and More apply degeneracy corrections and substitute the interatomic distance for the screening length in dense, strongly correlated plasma. The minimum impact parameter is set by the classical distance of closest approach or the de Broglie wavelength at high energies.

Once the cross section is calculated, evaluation of the transport coefficients is done numerically and the results are fitted by simple analytic functions. Details of electron mean free path calculations in solids and liquids as well as transport coefficient calculations including magnetic fields are complex and omitted here. This model greatly improves the accuracy of transport coefficients over the Spitzer model at low temperatures and agrees exactly with Spitzer at high temperatures (see Fig. 2.7). However, an error of less than a factor of 2 is still reported and the conductivity is overestimated for low-Z materials like hydrogen due to the neglect of electron-electron scattering.

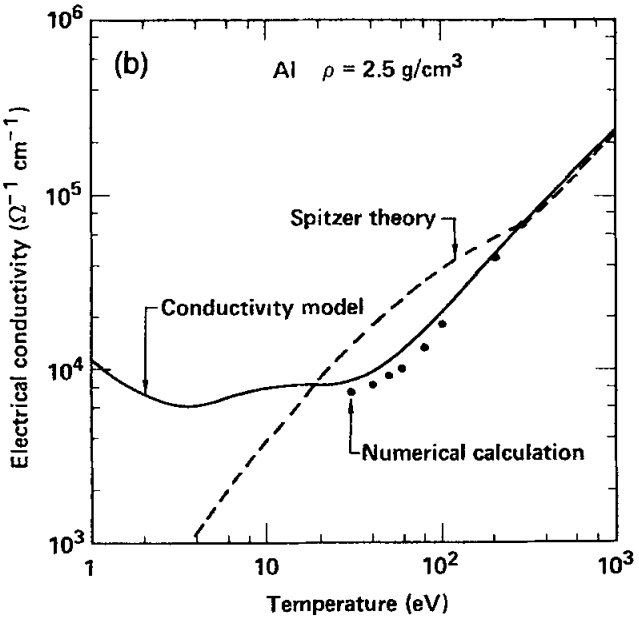

Figure 2.7: Electrical conductivity of solid Al (2.5 g/cm^3) versus electron temperature. The solid curve is the model of Lee and More and the dashed curve is from Spitzer. The solid circles are numerical calculations using partial waves theory. Figure taken from Lee[6].

Desjarlais[7] modified the Lee-More model to allow better agreement with experimental data and theories for dense plasmas in the metal-insulator transition regime. Modifications include an empirical modification to the minimum allowed electron relaxation time, a more accurate treatment of electron-neutral collisions, and a new ionization equilibrium model. The Lee-More model determines electron density using the Thomas-Fermi ionization model. However, the Thomas-Fermi model neglects any atomic structure effects on the ionization equilibrium and thus gives too high an ionization level under conditions well known to produce very low, insulator-like, ionization levels. Desjarlais, therefore, simply takes a weighted blend of Thomas-Fermi and a single ionization Saha model with a pressure ionization correction. Figure 2.8 shows the very good agreement between the Desjarlais modified Lee-More model (LMD) and Al experimental data at low temperatures.

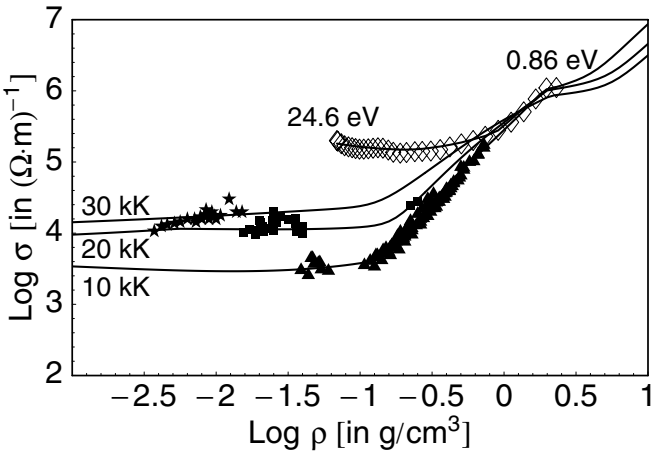

Figure 2.8: Comparison between results of the LMD model and experimental data for aluminum at various densities and low temperatures. Figure taken from Desjarlais[7].

Chapter 3

Plasma Simulation Codes

Several types of codes are used to simulate various stages of a laser-plasma interaction. This section will describe three codes used for this work: HYDRA, a radiation hydrodynamics code used to model pre-plasma formation, PICLS, a particle-in-cell (PIC) code used to model the laser-plasma interaction, and ZUMA, a hybrid-PIC code used to model the transport of relativistic electrons.

3.1 HYDRA

HDYRA[43] models laser interactions with solid density targets as a hydrodynamic problem with the laser rays acting as a source of energy on the grid. This laser energy is absorbed by *electrons* at a rate specified by the inverse bremsstrahlung approximation, after which this energy can be transferred to ions so that, in the absence of other heating (or cooling), the ion and electron temperatures will equilibrate on the electron-ion equilibration timescale, $\tau_{e,i}$ [6, 42]. This fluid is allowed to radiate and the diffusion of this radiation can be modeled by tracking the radiation energy density in a fixed number of photon energy groups, u_g, use the standard multi-group diffusion approximation to model radiation transport.

The equations of energy conservation for this 3T fluid (with hydrodynamic terms dropped

for simplicity) are then

$$\frac{\partial(\rho e_{\text{ele}})}{\partial t} = \rho \frac{c_{v,\text{ele}}}{\tau_{e,i}}(T_{\text{ion}} - T_{\text{ele}}) - \nabla \cdot \vec{q}_{\text{ele}} + Q_{\text{las}} + Q_{\text{abs}} - Q_{\text{emis}} \tag{3.1}$$

and

$$\frac{\partial(\rho e_{\text{ion}})}{\partial t} = \rho \frac{c_{v,\text{ele}}}{\tau_{e,i}}(T_{\text{ele}} - T_{\text{ion}}), \tag{3.2}$$

where e_{ele} and e_{ion} are the electron and ion specific internal energies, T_{ele} and T_{ion} are the electron and ion temperatures, $c_{v,\text{ele}}$ is the electron heat capacity computed from the EOS, $\vec{q}_{\text{ele}}$ is the heat flux from electron thermal conduction, Q_{las} is the laser heating and

$$\frac{\partial u_g}{\partial t} = \nabla \cdot \vec{q}_{\text{rad},g} - Q_{\text{abs},g} + Q_{\text{emis},g};\ g = 1, ..., N_g \tag{3.3}$$

and

$$Q_{\text{abs}} = \sum_{g=1}^{N_g} Q_{\text{abs},g},\ Q_{\text{emis}} = \sum_{g=1}^{N_g} Q_{\text{emis},g} \tag{3.4}$$

are the equations of radiative transfer for N_g energy groups. Q_{abs} and Q_{emis} represent the total radiation energy absorbed or emitted. For the present discussion we omit the equations of mass and momentum conservation, as well as equations connecting $Q_{\text{abs},g}$ and $Q_{\text{emis},g}$ to the opacity and temperature of the plasma, all of which can be found in a number of more-complete presentations of the equations of radiation-hydrodynamics [44].

Implicit in Eqs. 3.1-3.4 is an EOS model that is needed to determine the electron heat capacity as well as the relevant pressure for the fluid in whatever density and temperature state it may achieve during the course of the simulation. Note the EOS model treats electrons and ions *without* assuming that $T_{\text{ele}} = T_{\text{ion}}$, a condition often refered to as Local Thermodynamic

Equilibrum. Instead, for example, the total internal energy in each cell is given by

$$e_{\text{tot}} = e_{\text{ele}}(\rho, T_{\text{ele}}) + e_{\text{ion}}(\rho, T_{\text{ion}}) + \frac{1}{\rho}\sum_{g=1}^{N_g} u_g. \tag{3.5}$$

Likewise the total pressure is the sum of electron, ion and radiation components that are each functions of density and the temperature of the species. In this work, the inline Quotidian equation of state (QEOS) tables were used.

Also important is a model for the electron thermal heat flux into or out of a cell relative to the surrounding temperature gradient,

$$\vec{q}_{\text{ele}} = -K_{\text{ele}} \nabla T_{\text{ele}}. \tag{3.6}$$

K_{ele} can be a complicated function of density, temperature and the material properties, such as the Lee & More 1984 [6] model used in this work. However, near or significantly above $\sim$100 eV, K_{ele} typically asymptotes to the classical Spitzer formula [42]. In cases where a large value of $|\nabla T_{\text{ele}}|$ would give rise to unphysically large heat fluxes, $\vec{q}_{\text{ele}}$ is capped to some fraction of the maximum physically-allowable heat flux by a flux limiter, e.g.,

$$\vec{q}_{\text{max,ele}} = \alpha_{\text{ele}} n_{\text{ele}} k_{\text{B}} T_{\text{ele}} \sqrt{\frac{k_{\text{B}} T_{\text{ele}}}{m_{\text{ele}}}}, \tag{3.7}$$

where n_{ele} is the electron number density, k_{B} is Boltzmann's constant, m_{ele} is the mass of the electron, and $\alpha_{\text{ele}} = 0.05$ for this work.

These equations are coupled with a hydrodynamics solver and a ray-tracing algorithm to model the propagation of laser rays through the computational mesh. HYDRA employs an arbitrary Langrangian-Eularian (ALE) method for mesh evolution, allowing the grid to distort and move with the fluid flow with (preferably) minor deviations from this Lagrangian behavior to prevent severe tangling of the mesh[45].

3.2 PICLS

The interaction of an ultra-high intensity laser pulse with plasma near solid density involves highly non-linear processes and non-Maxwellian electron distributions. A kinetic treatment of particle distributions, therefore, is required to accurately compute relevant plasma parameters. For this work the code PICLS, developed by Y. Sentoku at UNR, was used. PICLS is a 2D PIC code that includes relativistic binary collisions and radiation cooling models.

3.2.1 PIC Method

The PIC method[46] was developed to address the challenge of consistently evolving large numbers of particles in a plasma. It is computationally impractical to simulate the actual number of particles in a solid density plasma ($\sim 10^{23}$), so a much smaller number ($\sim 10^{10}$) of *macro-particles* are used instead. These particles represent a large number of real particles but maintain the charge-mass ratio of an individual particle, thus behaving as expected when influenced by the Lorentz force.

Spatial grids are defined in the simulation region and macro-particles are distributed continuously on the grid according to the densities of the materials in the region. Maxwell's curl equations,

$$\frac{\partial \mathbf{E}}{\partial t} = c\nabla \times \mathbf{B} - 4\pi \mathbf{J} \tag{3.8}$$

$$\frac{\partial \mathbf{B}}{\partial t} = -c\nabla \times \mathbf{E} \tag{3.9}$$

are then solved using a finite difference scheme[46] at grid vertices where the current is collected in each grid cell and values at vertex locations are interpolated using a 4th order scheme. Advancing the particle locations and momenta in time is a multistep process:

- macro-particles are accelerated for a half timestep by $\mathbf{E}$
- Colulomb collisions performed between macro-particles

- macro-particle momenta rotated by **B** according to Lorentz force equation
- macro-particles are accelerated for remaining half timestep by **E**
- Colulomb collisions performed between macro-particles

The field values at particle locations are interpolated from vertex locations in a similar manner as the current interpolation.

3.2.2 PICLS Physics

The collision model in PICLS is fully relativistic and deals with collisions between weighted particles of arbitrary species, perfectly conserving energy and conserving momentum on average[47]. The model assumes small angle scattering and that the simulation grid size is $\sim \lambda_D$ so that collisions are only performed on particles within a Debye sphere. Moreover, the collision frequencies for free electrons include terms dealing with collisions with other free electrons, bounded electrons, ions and unshielded ion charge.

For electron-electron collisions

$$\nu_{ee} = \frac{1}{2}\frac{4\pi e^4 n_i}{p^2 v}\{Z_i\ ln(\Lambda_{free}) + (Z - Z_i)\ ln(\Lambda_{bound})\} \tag{3.10}$$

where n_i is the local ion density, e is the charge of an electron, p and v are the electron momentum and velocity in the rest frame of the colliding particle and Z_i and Z are the current degree of ionization and atomic number of the ion species associated with the bound electron. Λ_{free} is the Coulomb logarithm factor for free-free collisions and is defined as $\frac{\lambda_D}{b_0}$ where b_0 is the deBroglie wavelength of the impacting electron, and

$$\Lambda_{bound} = \frac{1}{2}\left[ln\ \frac{(\gamma-1)^2(\gamma+1)}{2\ I^2} + 1 - \beta^2 - \frac{2\gamma-1}{\gamma^2}\ ln2 + \frac{\gamma-1}{8\gamma}\right] \tag{3.11}$$

is the Coulomb logarithm factor for free-bound collisions where

$$I(Z_i) = 10(eV) \cdot \frac{Z}{mc^2} \frac{1.29\, x^{(0.72-0.18x)}}{\sqrt{1-x}} \tag{3.12}$$

$x = Z_i/Z$, and γ is the Lorentz relativistic factor. For electron-ion collisions

$$\nu_{ei} = \frac{4\pi e^4 n_i}{p^2 v} \{Z_i^2\ ln(\frac{\lambda_D}{a}) + \langle \bar{Z}^2 \rangle\ ln(\frac{a}{b_0})\} \tag{3.13}$$

where $a = 1.4\frac{a_{Bohr}}{Z_i}$ is the radius of the bounded electron cloud and $\bar{Z}$ is the average unshielded nuclear charge and $\langle \bar{Z}^2 \rangle = \sum_{j=i+1}^{N} \frac{Z_j^2}{N-i}$.

In addition to these collision models, PICLS also includes radiation losses due to free-free collisions and bound-bound collisions. Both the collision and radiation cooling models have been shown to have large effects in high density target materials such as gold[48].

3.3 ZUMA

The code ZUMA was develop by D. Larson at LLNL and is based on the hybrid models of Davies[49] and Honrubia[21]. ZUMA treats relativistic electrons kinetically and the background plasma as a resistive fluid (thus considered a hybrid-PIC code). Computationally, this allows for simulations of larger spatial and temporal scales than PIC simulations in a much shorter time. The physical assumptions of the code are also well suited to the problem of laser produced relativistic electron transport through solid density metals. Namely, the number density of relativistic electrons is much less than that of background electrons and the relativistic electron velocity is much greater than the mean background velocity. ZUMA also assumes current neutrality between the relativistic electron current and the background return current, a valid assumption for solid density metal targets.

More detail will be provided about ZUMA than the previously described codes as the

dissertation author developed parts of code, used it for the all of the physics investigations in Chapter 6, and developed a Python codebase for analyzing the simulation output.

3.3.1 ZUMA Timestep

The main ZUMA timestep is outlined here with detailed descriptions of each module/function following. Referenced equations are described in Chapter 2. For each time t:

- **Drag and Scatter** routines applied to particles
- **Move Particles** 1/2 timestep
- **Apply Lorentz Forces** routines applied to particles
- **Move Particles** 1/2 timestep
- **Inject Particles** according to current laser conditions
- **Accumulate Sources**
- **Update Fields**
- **Update Temperature**
- **Diagnostics Output**

Drag and Scatter

For each particle, this subroutine computes its drag and scatter coefficients and the Kα and bremmstrahlung radiation generated as it travels through the background plasma. The equations for drag and scatter are from Atzeni[36] (see Sec. 2.3.2). Kα emission is calculated using cross sections from Hombourger[8](see Sec. 2.3.3) and bremmstrahlung emission is calculated using cross sections generated by the code ITS[50]. The resulting particle energy, E_{final}, after these processes is

$$E_{final} = E_{original} - E_{K\alpha} - E_{Brems} - E_{Drag},$$

where $E_{original}$ is the particle energy before module is executed. Kα and bremmstrahlung radiation values per cell are stored and particle energy losses from drag are accumulated in background heat deposition arrays. All of these values are resolved in time and heat deposition is additionally resolved by fast electron energy (10 logarithmically spaced energy bins from 0.1 to 27 MeV).

Move Particles

Particles positions are advanced in time according to their current positions and velocities. Particles with energies below an adjustable energy threshold (usually 5-10 keV) are deposited into the background as heat. Boundary conditions are applied in this module (reflective or absorbing) and diagnostics tracking particle flux are run.

To properly characterize fast electron divergence and energy flux, a diagnostic was developed to record fast electron energies and angles relative to the z-axis (axis of propagation for electrons) at various radii throughout the simulation target. Fig. 3.1 illustrates how the diagnostic works. At various radii relative to the particle injection location, time integrated particle number and energy are recorded if the particle crosses a radial curve. Particle number is determined by simply recording and accumulating the weight, w, of the fast electron macroparticle. Energy is defined as Ew, where E is the particle energy before advancement, and is similarly accumulated over time.

Apply Lorentz Forces

Current **E** and **B** fields are obtained and linearly interpolated at particle positions. Particle velocities are then updated 1/2 timestep according to the Lorentz force law

$$F = -e(\mathbf{E} + \mathbf{v} \times \mathbf{B}).$$

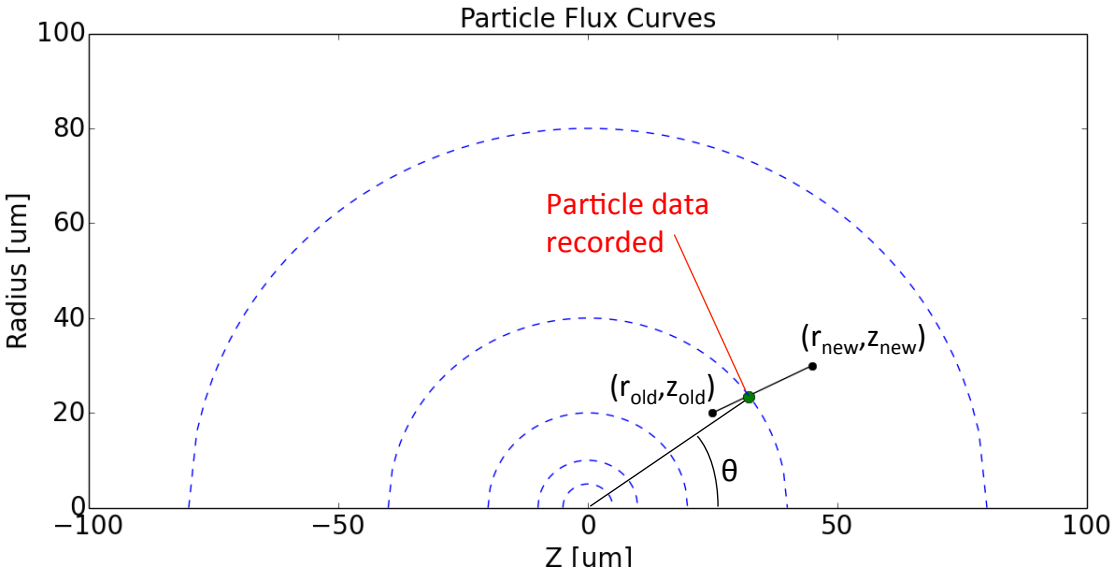

Figure 3.1: Typical setup of particle flux curves (blue dotted lines) in a ZUMA simulation region. Here, particles are injected at $z = 0$ μm in the $+z$ direction and particle data is recorded at radii of 5, 10, 20, 40 and 80 μm. The (r,z) coordinates of each particle are known before and after advancement. Linear motion is assumed between these coordinates, and the intersection of the linear particle trajectory and circular flux curve is calculated to obtain the particle angle, $0^\circ < \theta < 180^\circ$, relative to (0,0) and the z-axis.

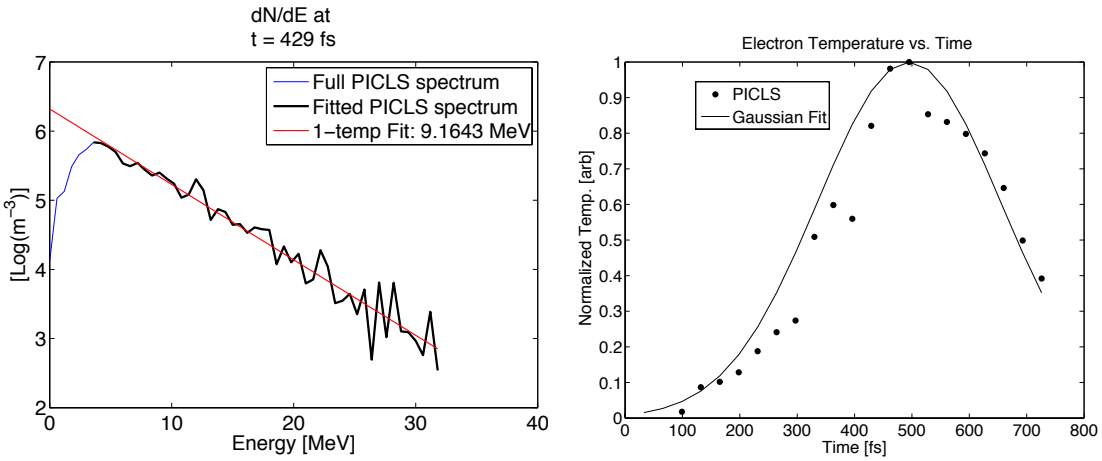

Figure 3.2: An LPI simulation using experimental conditions was run using the PICLS code. At 22 timesteps during the laser pulse (730 fs), the injected electron spectrum (dN/dE) was sampled. The LHS plot shows the spectrum (blue) at $t = 429$ fs fitted with a 1-temperature exponential distribution (red). The RHS plot shows the fitted electron temperatures vs. time with a Gaussian fit, clearly indicating a temporally-dependent energy distribution.

The difference between particle energy before and after the Lorentz force is applied is calculated and used as a diagnostic to track the amount of energy fast electrons lose to fields (ohmic stopping). Moreover, this diagnostic is resolved in time and fast electron energy.

Inject Particles

This subroutine injects particles at a specified location based on user inputted laser intensity and fast electron distributions. The main steps involve constructing normalized fast electron energy and angle distributions, generating macroparticles consistent with these distributions with weights based on spatial and temporal laser pulse parameters, and implementing diagnostics to track the injected spectrum. When first implemented, ZUMA did not allow for fast electron energy or angular distributions that depended on time. This functionality was added by the author because, in addition to being more physically accurate (see Fig. 3.2), it was applied in previously reported state-of-the art hybrid-PIC simulations by Honrubia[20] that were used as a benchmark (see Sec. 3.3.2) and launching point for the simulations presented in Chapter 6.

The laser intensity, assuming Gaussian distributions in space and time, is defined as

$$I(r,t) = I_0 \; e^{-r^2/2\sigma_r^2} \; e^{-t^2/2\sigma_t^2} \tag{3.14}$$

where I_0 is the peak intensity, r is radius, t is time and σ_r and σ_t are the standard deviations of the spatial and temporal distributions. Since a laser plasma interaction is not actually being calculated, this intensity serves to calculate the number of particles (or weight of each macroparticle) injected at each location and time.

After a value for intensity is calculated based on the current time and randomly chosen particle location, the electron energy and angular probability distributions are defined and normalized. Energy distributions can be complex, two-temperature distributions, as defined by Eq.1 in [33], or as straightforward as a single exponential distribution of the form $exp(-E/T)$, where E is electron energy and T is an average beam temperature supplied by the user. In any case, ZUMA will use the supplied energy distribution to randomly choose a particle's energy. Similarly, the particle injection angle can be determined from a supplied distribution, such as the classical ejection angle formula (see Sec. 2.2.6),

$$\tan(\theta) = \sqrt{\frac{2}{\gamma - 1}}$$

where θ and γ are the ejection angle and relativistic Lorentz factor of the particle.

Particle weight, w, is defined as

$$w = \frac{CE \; \cdot \; I(r,t) \; \cdot \; A_p \; \cdot \; dt}{E_p}$$

where CE is the laser-to-fast electron energy conversion efficiency (user inputted) and E_p is the particle energy. $A_p \approx 2\pi r dr$ is the annular area over which the particle injection occurs in the injection (usually $z = 0$) plane, where r is the particle injection radius and dr is the diameter (in

Table 3.1: Comparison of additional Ohm's law terms in the LMD and EH transport models for magnetized and unmagnetized cases.

	Hall	Thermo-electric	Nernst	Pressure
LMD-unmag		X		
LMD-mag	X	X	X	
EH-unmag		X		X
EH-mag	X	X		X

the r direction) of the particle.

Accumulate Sources

Calculate current density, J, based on current particle distributions by accumulating $w_p e v_p$, where w_p and v_p are the particle weight and velocity, respectively, and e is electron charge.

Update Fields

This subroutine updates **E** and **B** field values using Maxwell's equations. For the electric field calculation, the material resistivity, η, is first calculated using the LMD[6, 7] (see Sec. 2.3.5) or Epperlein-Haines (EH)[51] model with a modified Thomas-Fermi ionization model (see Sec. 2.3.4) from More[41]. The return current, $\mathbf{j_r}$, is then calculated using Ampere's law (assuming charge neutrality)

$$\mathbf{j_r} = -\mathbf{j_f} + \frac{1}{\mu_0}\nabla \times \mathbf{B}$$

where $\mathbf{j_f}$ is the fast electron current density. The electric field can then be determined using Ohm's law. ZUMA can calculate Ohm's Law using the LMD or EH models in the magnetized and unmagnetized cases. In addition to using different transport coefficients than the LMD model, the EH model can include different Ohm's law terms (in addition to $\eta \cdot \mathbf{j_r}$) as summarized in Table 3.1. For the simulations presented in this work, only the magnetized LMD model was used.

After calculating the electric field, ohmic heating, $\mathbf{j_r} \cdot \mathbf{E}$, can be calculated using the collisional (resistive and thermo-electric) terms of the electric field only. Given $\mathbf{E}$, the magnetic field is then determined using Faraday's law

$$\frac{\partial \mathbf{B}}{\partial t} = -\nabla \times \mathbf{E}.$$

Update Temperature

The background temperature is updated assuming instantaneous equilibration between electrons and ions according to

$$n_i(CZ + 1.5)\frac{\partial T_e}{\partial t} = \mathbf{j_r} \cdot \mathbf{E} + E_{Drag} \tag{3.15}$$

where n_i is the ion density, Z is the average ionization state, and RHS terms are previously defined ohmic heating and drag terms. C is the material heat capacity defined by

$$\begin{aligned} &\frac{3}{2}n_e k_B \frac{\pi^2 k_B T_e}{3\varepsilon_F}, && \frac{T_e}{T_f} \leq 0.7 \\ &\frac{3}{2}n_e k_B \left[\frac{5}{3}\frac{F_{3/2}}{F_{1/2}} - \frac{\mu}{k_B T_e} + \frac{1}{k_B}\frac{\partial \mu}{\partial T_e}\right], && \frac{T_e}{T_f} > 0.7, \end{aligned}$$

which yields a smooth transition between Fermi degenerate and classical states of matter. Here, F_n are Fermi-Dirac integrals with argument $\mu/(k_B T_e)$, T_F is the Fermi temperature and ε_F is the Fermi energy. The chemical potential, μ, is defined by Ichimaru with a fit between the degenerate and classical limits[52].

Diagnostics Output

Numerous diagnostics and outputs have been developed in ZUMA. Energy diagnostics yield temporally and spatially resolved values for fields, radiation (Kα and bremmstrahlung),

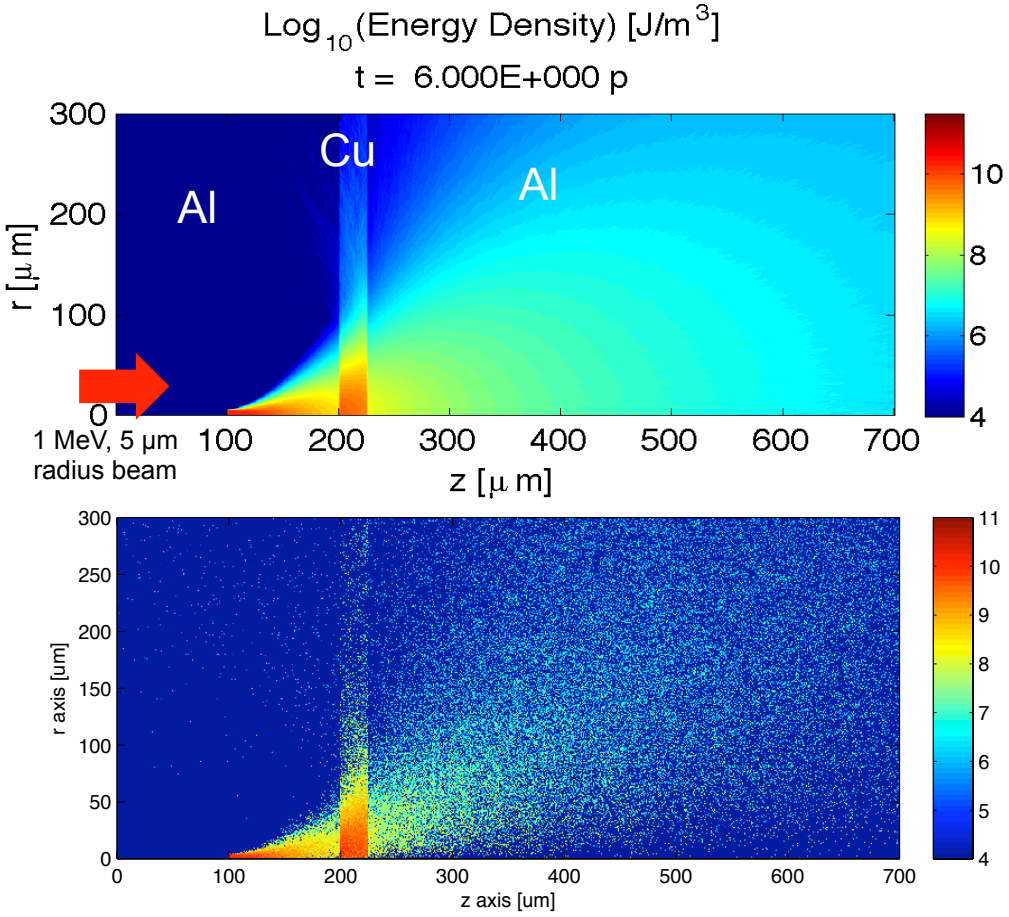

Figure 3.3: A 1 MeV relativistic electron beam with a 5 μm radius was injected into a 300 x 700 μm Al slab with 20 μm thick Cu layer. Resulting time-integrated Kα energy density yields are shown for ZUMA (top) and LSP (bottom) using the same color scale.

particles (lost/absorbed, propagating), heat deposition (collisional and ohmic), ionization and fast electron density. The author was responsible for the development of fast electron diagnostics tracking injected energy spectra and angular distributions as well as time integrated particle and energy flux diagnostics tracking the same quantities throughout the simulation region.

3.3.2 Development and Benchmarking

The author was responsible for extending the Kα emission package's functionality to multiple background materials (in addition to Cu). Emission energies are taken from the NIST

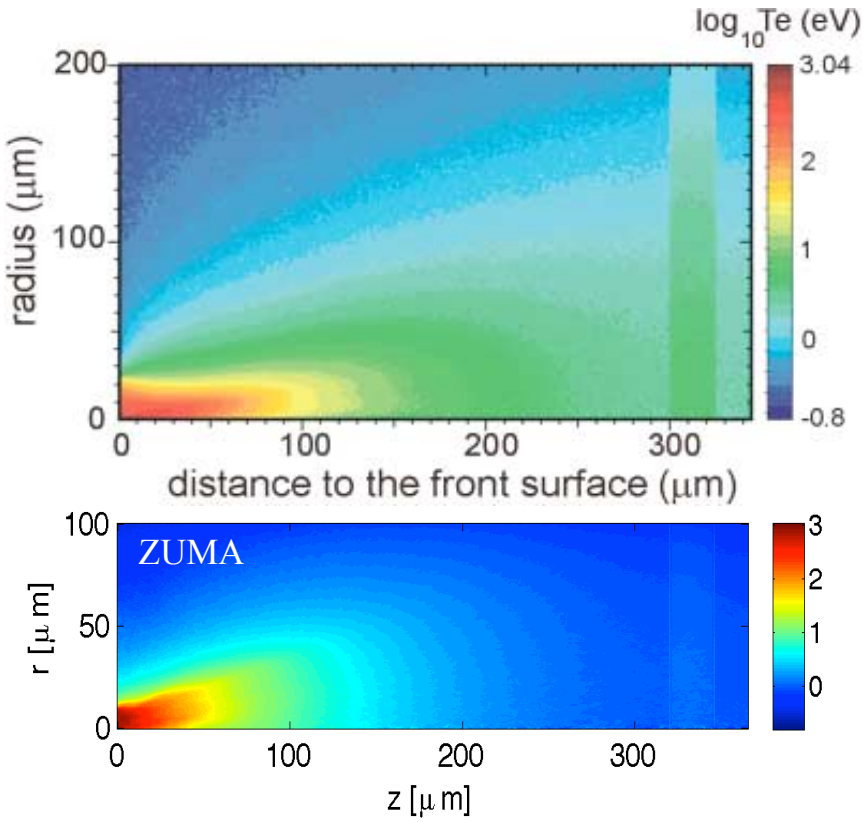

Figure 3.4: Time-dependent energy and angular distributions were used to inject relativistic electrons into an Al slab with a Cu fluorescence layer. The resulting temperature distributions (in units of $\log_{10} T_e$ (eV)) for Honrubia's code (top) and ZUMA (bottom) are shown.

database, fluorescence yields (ω_k) from Bambynek [53] and transition probabilities from Rao [54]. The Kα and Drag and Scatter routines were benchmarked to those of the plasma code LSP [55], which was previously benchmarked to analytic formulas by D. Higginson [56]. Figure 3.3 shows a comparison of spatially resolved Kα emission plots produced by ZUMA and LSP simulations of a monoenergetic electron beam propagating through a multilayered, solid target . Both codes yield similar spatial distributions and total Kα yields for Al and Cu are in good agreement.

Previously described injection routines were also compared to published simulations by Honrubia [20]. Beam parameters and targets identical to those used by Honrubia were implemented in ZUMA simulations, and resulting target temperature distributions are shown in Fig.

3.4. The Honrubia runs show slightly higher temperatures on axis past z = 50 μm, possibly due to the different resistivity model used (described in Eidmann [57]). Ohmic deposition and Kα emission were in excellent agreement.

Chapter 4

Laser Facility and Experimental Diagnostics

4.1 Titan Laser System

The Titan laser system at LLNL uses the technologies of mode-locking[58] and optical parametric chirped pulse amplification [11–13] to achieve extremely high on-target intensity levels ($\sim 10^{20}$ W/cm^2.).

Mode-locking[58] involves inducing a constant phase difference between various modes in the resonant cavity of the laser system. Because the phase difference is constant, constructive interference between the modes occurs at regular intervals producing pulses of laser light. Various methods exist for modulating the light in the resonant cavity (acousto-optic modulators, synchronous pumping, saturable absorbers) and can yield extremely short laser pulselengths. Efficient amplification of mode-locked pulses is achieved via optical parametric amplification (OPA) [12, 13] and chirped pulse amplification (CPA) [11]. In contrast to a standard lasing medium, OPA uses a nonlinear crystal and additional pump laser (wavelength shorter than signal pulse) to amplify the signal pulse more efficiently and with higher signal-prepulse contrast.

CPA involves stretching the signal pulse spatially and temporally before amplification and compression afterwards, thus avoiding damage of beam optics while achieving very high intensities.

The Titan laser[59] uses an Nd:Glass lasing medium to produce 1053 nm light with an energy of 150 J in 0.7 ps, yielding an on-target intensity of 10^{20} W/cm^2 after final focusing.

4.2 Laser Diagnostics

Various diagnostics are used to characterize the laser energy, pulse length, focal spot quality and pre-pulse. After the generation and amplification stages of the laser system but before the final focusing parabola, a small fraction of the main pulse ($\sim$1%), known as leakage light, is directed to these diagnostic systems. The on-shot energy is determined simply by directing the leakage to a calibrated calorimeter. The pulselength (FWHM of power vs. time trace) is determined using a 2nd order auto-correlator[60] which splits leakage light into two pulses. One is sent through a delay line of known length and recombined with the other, and the resulting intensity is recorded. Correlating delay and intensity then allows pulselength to be determined.

Preceding the main pulse is a pre-pulse caused by amplified spontaneous emission in the laser system. Though its intensity is $\sim 10^{-8}$ less than that of the main pulse, it is still high enough ($\sim 10^{12}$ W/cm^2) to ablate and ionize target surfaces. The resulting preplasma interacts with the main pulse and alters the laser-plasma interaction physics, and it is therefore important to characterize the pre-pulse. Figure 4.1 shows a typical oscilloscope trace of a Titan pre-pulse measured using a water cell protected fast diode[61]. Pre-pulse energies ranged from 10 - 30 mJ in this work.

The on-shot focal spot quality is measured using an equivalent plane monitor (EPM). Leakage light is directed onto a 16-bit CCD camera. Figures 4.2(a) and (b) show a typical camera image and intensity distribution for Titan. These images are acquired for every shot and are compared to an image of a low-energy OPCPA produced spot acquired after the focusing

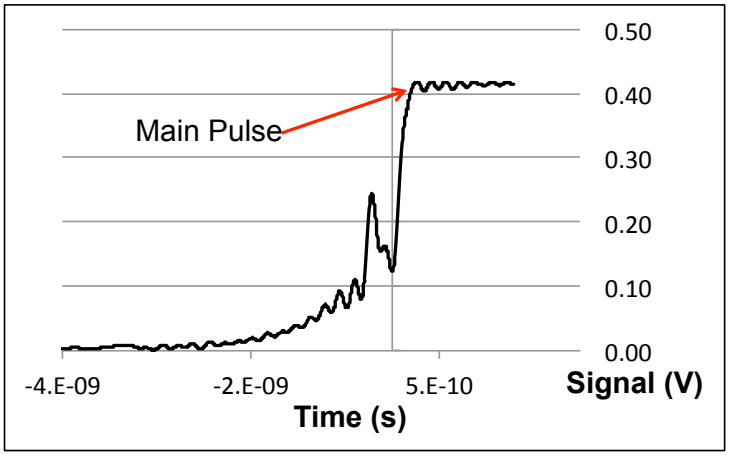

Figure 4.1: Typical Titan pre-pulse scope trace where the voltage is proportional to signal intensity. The intensity becomes significant ∼2 ns before the main pulse, which is saturating the scope output here.

parabola to ensure consistency during experiments.

4.3 Experimental Diagnostics

4.3.1 Kα Radiation Diagnostics

Kα Radiation

Fast electrons undergo binary collisions with background target material atoms that can cause ionization by removing atomic K-shell electrons. For copper, a commonly used material in fast ignition experimental targets, transitions of electrons from the L- and M-shells to the resulting vacant position in the K-shell can yield Kα ($K_{\alpha 1}$ = 8048 eV, $K_{\alpha 2}$ = 8028 eV) and $K_{\beta 1}$ (8905 eV) radiation, respectively. The cross-section for these interactions is relatively flat for a large range of fast electron impact energies [8, 62], as shown in Fig. 4.3, and therefore Cu K-shell emission intensity correlates well with fast electron flux [63]. Given the line intensity of $K_{\alpha 1}$ radiation is at least 3 times that of $K_{\alpha 2}$ and 5 times that of $K_{\beta 1}$, we measure the spatial and spectral distribution of radiation emitted from targets with experimental diagnostics tuned to the

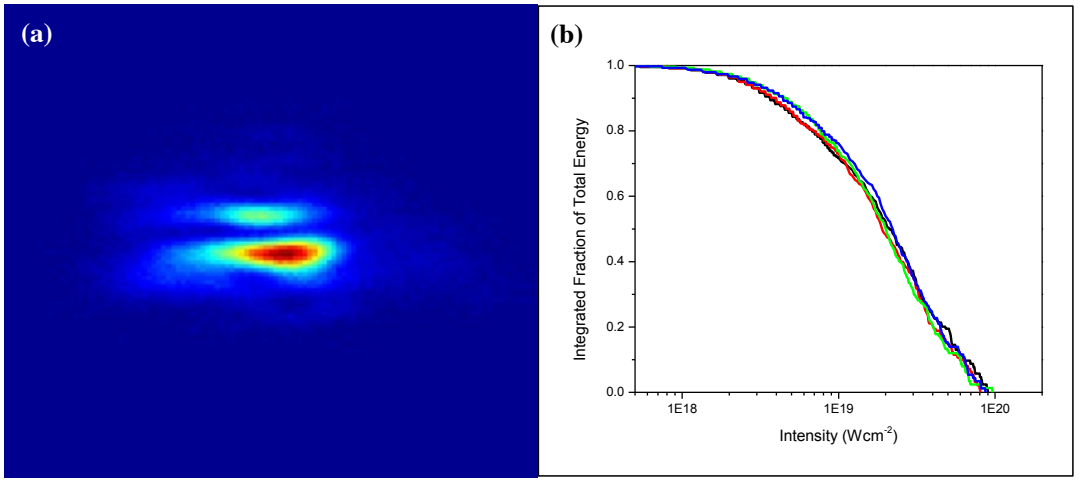

Figure 4.2: (a) Typical EPM focal spot image. (b) Corresponding intensity distribution (shown for several shots to illustrate consistency).

$K_{\alpha 1}$ line.

Dual Channel HOPG Spectrometer

The Dual Channel HOPG (highly ordered pyrolytic graphite) Spectrometer [64] is used to measure an absolute radiation spectrum via Bragg reflection. In crystal diffraction theory, the Bragg angle is defined by:

$$n\lambda = 2d\sin\theta_B, \tag{4.1}$$

where n is the diffraction order, λ is the radiation wavelength, d is the crystal plane separation and θ_B is the Bragg angle. Thus, given a crystal with particular plane spacing d, radiation with wavelength λ can be successfully reflected off the crystal only if it has an angle of incidence θ_B.

The HOPG crystals used are of grade ZYA with spacing $d = 0.3354$ nm and a mosaic spread of $\gamma = 0.4$, where γ is the full width half maximum of a Gaussian distribution of crystal plane orientations about the axis normal to the crystal surface. This mosaicity serves to increase reflectivity because incident radiation has a greater chance of encountering a Bragg reflection plane as it propagates through the crystal. The effect known as mosaic focusing can be achieved

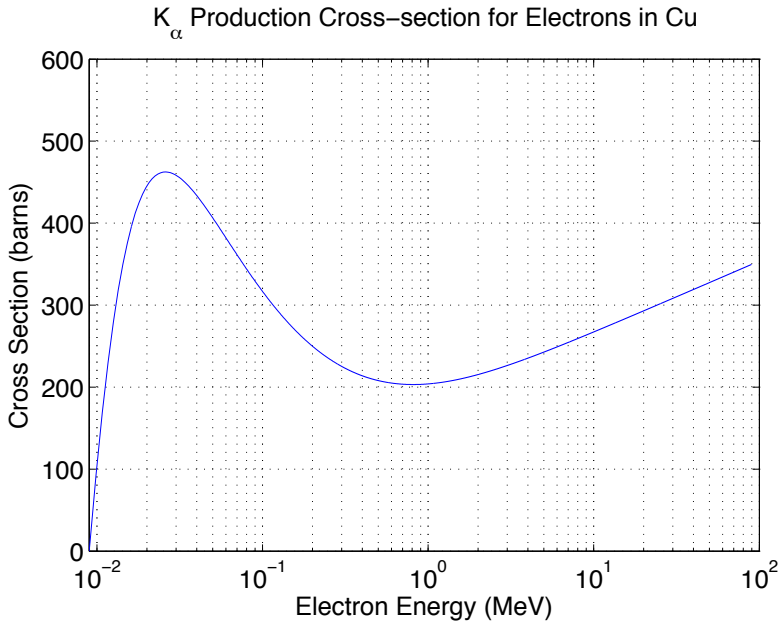

Figure 4.3: Cross section for Kα production as a function of fast electron impact energy in copper, given by equations in [8]. Note the relatively small variation between 0.2 and 10 MeV. Image courtesy of D.P. Higginson.

by setting the image detection plane-crystal distance to be equal to the source-crystal distance (magnification of 1). Moreover, orienting the detector parallel to the crystal surface allows for the focusing of multiple spectral lines.

The geometry of the DCHOPG was thus optimized to record spectral ranges centered on the Cu ($\sim$8 keV) and Ag ($\sim$22 keV) Kα radiation lines whilst maximizing photon collection efficiency and employing mosaic focusing, as shown in Fig. 4.4. Spectral images were recorded on commonly used and well characterized Fujifilm BAS-SR and MS image plates [65]. Figure 4.4(a) shows a sample image from the Cu channel of the DCHOPG. The largest source of spectral broadening is due to the depth ($\sim$2 mm) of the crystal. An incident photon can be reflected from a crystal plane at any depth in the crystal, hence the reflection plane of the spectrometer is variable. Because the image plane is fixed by spectrometer, a shift in the reflection plane translates to a smearing of a spectral line on the image plate. The effect of spectral broadening is to lower energy resolution, measured to be 56 ± 5 eV for the Cu channel.

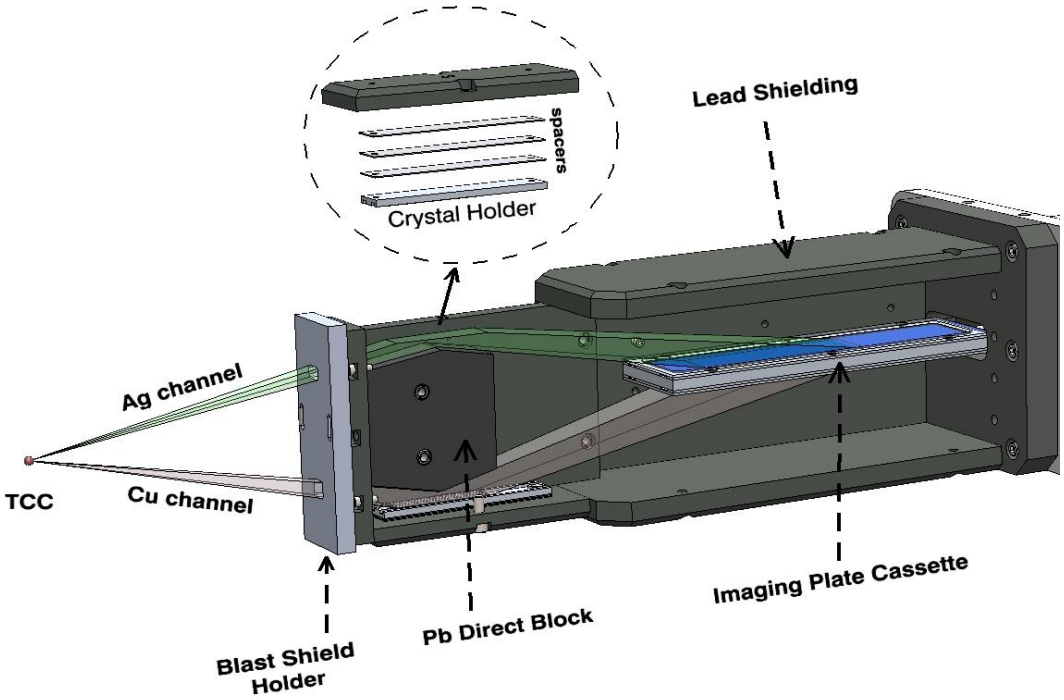

Figure 4.4: Schematic of DCHOPG Spectrometer. Illustrates path of radiation from target chamber center (TCC) through entrance slits, off HOPG crystals and onto image plates. Entrance slit geometry chosen so that incoming photons fill entire crystal surface. Image plates are held in light tight cassettes covered with a 50 μm aluminized mylar to prevent visible light and debris from reaching the image plates. Lead direct beam block and shielding minimize exposure of image plates to background radiation. Figure taken from [64].

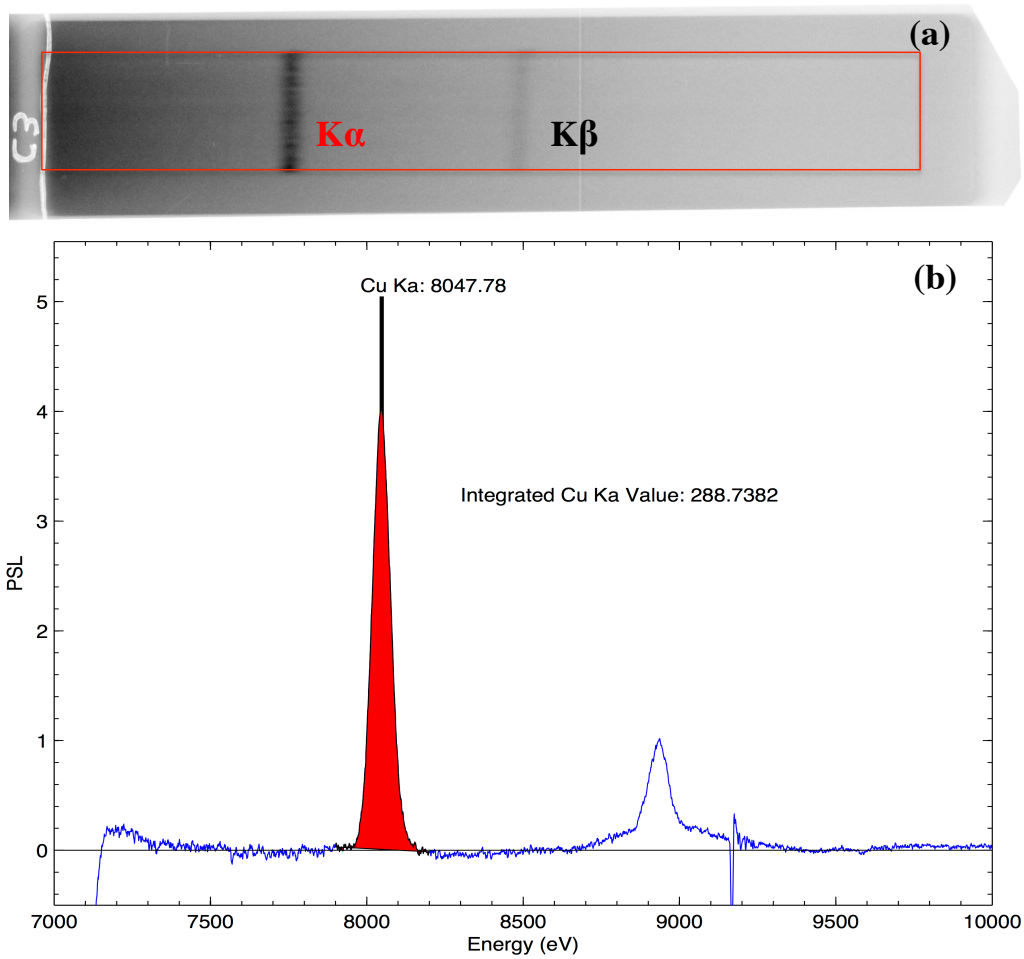

Figure 4.5: (a) Sample image of Cu DCHOPG data. Kα and Kβ lines are visible and red box shows region where lineout was taken. (b) Background subtracted lineout, integration under Kα peak shown in red. Spectral line amplitudes given in PSL (Photo Stimulated Luminescence) units obtained when image plates are digitized and processed by a Fuji FLA7000 scanner.

Figure 4.5(b) shows a background subtracted lineout taken along the energy axis of the image and integrated over the width of the crystal. The excellent signal to noise ratio is due to lead shielding and beam block of the DCHOPG. Analysis of spectra is straightforward; often the most useful feature for comparing experimental data is the integral under the Kα peak.

A cross calibration of the DCHOPG has been done with a Spectral Instruments CCD Camera so that relative integrated Kα yields can be converted to absolute yields. The camera was perviously calibrated at 5.9 keV and 22 keV using Fe-55 and Cd-109 sources [66]. The CCD camera and DCHOPG were then both fielded during the same experiment and a conversion constant of $A = (6.37 \times 10^8 \pm 18\%) \frac{photons}{sr \cdot PSL}$ was obtained for the Cu channel.

Kα Imager

The Cu Kα Imaging system[67] employs a spherically bent quartz 211 crystal to both reflect (via Bragg diffraction) and focus Cu Kα radiation with a narrow bandwidth ($\sim$6 eV), providing a diagnostic to measure 2D time-integrated fast electron spatial distributions. The crystal used in the experiment in this work has a spacing of $2d = 0.3082$ nm ($\theta_B = 88.7^\circ$ for Kα radiation) and a radius of curvature of 50 mm.

Fig. 4.6 shows a schematic of the system setup. The slight offset of the source from the crystal axis results in an optically astigmatic system. This astigmatism results in different meridional and sagittal crystal focal planes. To maximize spatial resolution, we place the image plates midway between these planes at location given by $p = qR/(2q-R)$, where p indicates the image location, q the object location, and R the radius of curvature of the crystal. At this location the point spread function, σ_{as}, is round and is the largest factor limiting the spatial resolution of the image. It is denoted by

$$\sigma_{as} = \frac{M+1}{M}(1-\sin\theta_B)D, \tag{4.2}$$

where M is the magnification of the system ($M = p/q$) and D is the aperture limiting the collect-

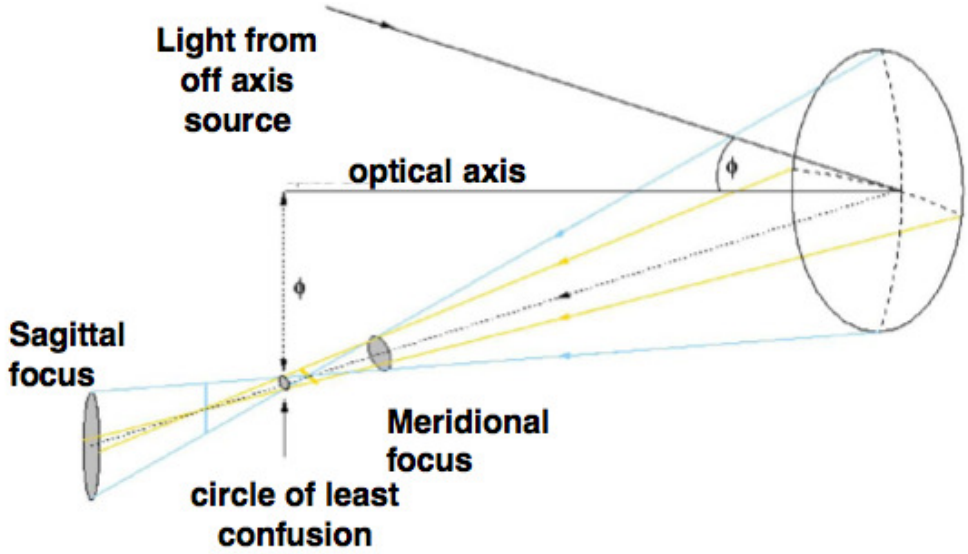

Figure 4.6: Setup of Cu Kα Imaging system. Light is emitted from the source/target, reflects off the crystal and is then recorded on image plates placed in the circle of least confusion. The angular separation of the source and image planes relative to the crystal is 1.3°.

ing area of the crystal. After the astigmatism, local crystal quality is the most important limiter of the spatial resolution[68].

Figure 4.7(a) shows a typical Kα image recorded on a Fujifilm image plate. Visible are the Cu fluorescence layer of the target and the bright, central spot where most of the fast electrons passed through layer. Typically one is interested in an intensity profile along the radius of the spot. Fig. 4.7(b) shows the profile that results from averaging the intensity values over 2π radians in the θ direction for each point along the radius (bin size on the order of 1 image pixel). The resolution in this case was 20 μm.

4.3.2 Bremmstrahlung Spectrometer

As described in Chapter 2, bremmstrahlung radiation emitted from accelerating electrons is sensitive to both electron energy and propagation angle. The bremmstrahlung spectrometer[9] uses differential filtering to measure the x-ray emission spectrum (up to $\sim$1 MeV) due to fast

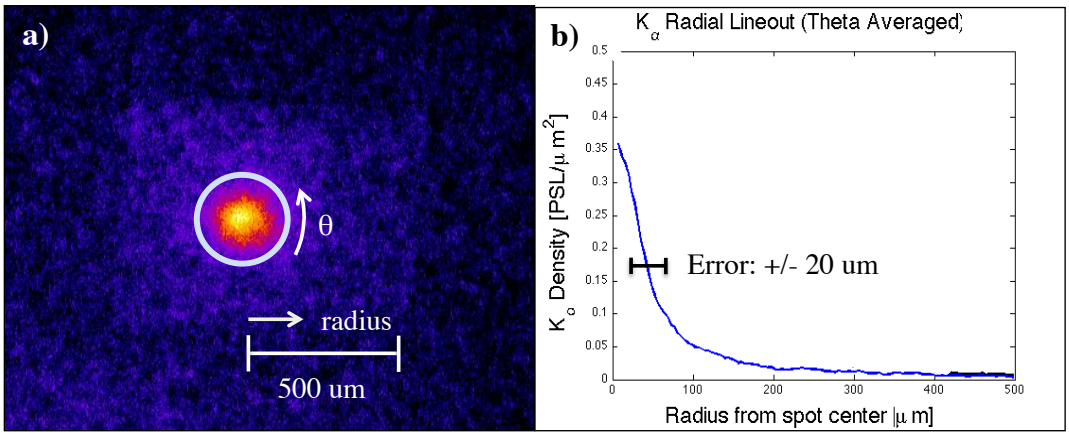

Figure 4.7: (a) Sample Kα image with radial and θ directions chosen for analysis. (b) Intensity profile taken along radial direction and averaged over θ.

electron propagation through experimental targets. A backward computational analysis is then used to infer the fast electron spectral parameters.

The spectrometer consists of 13 filters of increasing atomic number ranging from Al to Pb and Fujifilm image plates as dosimeters (see Fig. 4.8). This arrangement causes images plates in the back of the stack to be more sensitive to high energy x-rays than the those in the front. The filters and image plates are stacked in a Lexan cartridge and surrounded by a 1.8 cm thick Pb box that shields photons up to 2 MeV. Additionally, a 12.5 cm long Pb collimator with 1.25 cm diameter entrance hole is placed between the target and spectrometer to reduce background noise from directions other than the spectrometer-target axis. Finally, a magnet is placed in front of the collimator to deflect electrons up to 100 MeV from the collimator entrance.

Determining fast electron spectrum given bremmstrahlung data requires large amounts of computation. The Monte Carlo code ITS 3.0 is used to first model the x-ray spectrum produced by the transport of electrons through the experimental target, taking into account collisions and radiative losses but not field effects. Second, the image plate response of the spectrometer filter stack to a large range of photon energies is calculated (1 keV - 100 MeV). With these two response functions, spectrometer image plate signals can be predicted given an initial fast electron

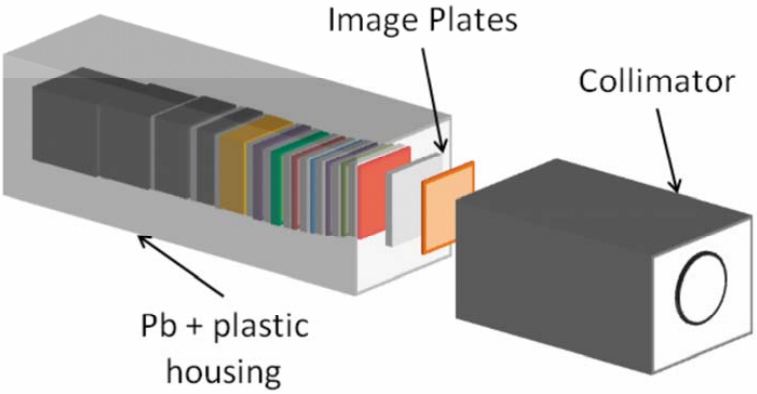

Figure 4.8: Setup of bremmstrahlung spectrometer showing filter and image plate stack, collimator and magnet. The image plates are placed behind each metal filter in the stack. Signals are averaged over the entire image plate for analysis. Figure taken from [9].

spectrum. A genetic algorithm is used to calculate the spectrometer responses to initial electron spectra within a large parameter space and those that are consistent with the experimental spectrometer data are noted. The fact that multiple electron energy distributions are consistent with the data is the largest source of error in the inferred electron spectrum[29]. Moreover, because of the large error associated with the bremmstrahlung spectrometer, it is used as a secondary diagnostic in this work to support the findings of Kα diagnostics.

Chapter 5

Experimental Transport Study

5.1 Introduction

Cone guided fast ignition (FI) inertial confinement fusion requires efficient energy transport of high-intensity short-pulse-laser-produced relativistic (or "fast") electrons through a solid cone tip to a high density fuel core[14]. Specifically, successful ignition with a reasonably sized ignition laser requires high conversion efficiency to 1-3 MeV electrons that have a minimum divergence[17, 36]. Previous simulations show that fast electron beam propagation in solid density plasmas are affected by a variety of mechanisms: scattering, resistive collimation[17, 18], resistive filamentation[19], ohmic heating and electric field inhibition[20, 21]. Evaluating the cone tip material, therefore, requires an understanding of the evolution of self-generated resistive fields and their cumulative effect on electron transport over the duration of the laser pulse.

Many experiments have investigated transport through solid materials. Most of them are limited, however, because they study transport through only one material [22, 23] or compare transport through different materials with different fast electron sources [24]. Reference [25] studies transport through insulators and conductors with the same electron source but using a laser with half the pulse length and an order of magnitude smaller energy than in the work pre-

sented here. Most analyses, also, do not go into detail about the magnetic field development and its effects on transport but rather focus on quantifying beam divergence, electron conversion efficiency and temperature, and electron stopping lengths. More recent work [69] describing proton generation from thin (10-40 μm) metal targets (various Z) has suggested that the differences observed in proton beam spatial profiles (filamentation, hollowing and collimation) are a consequence of self-generated magnetic fields arising from Z-dependent resistivity differences. This experiment, however, did not examine transport in different materials using the same electron source and the effect of the target material on forward-going fast electron energy flux, therefore, was not discussed.

This chapter reports a systematic investigation of fast electron transport in different materials (from high-Z Au to low-Z Al) without changing the electron source. It was demonstrated that a fast electron beam can be collimated with a thin ($\sim$10 μm), high- or mid-Z transport layer buried a few μm beneath a low-Z Al layer without imposing a significant loss in forward-going electron energy flux, in contrast to previous 1D Fokker-Planck (FP) modeling predictions [70] that suggest high-Z Au material would increase divergence due to scattering and reduce the forward energy coupling, but consistent with the analytical model and 2D FP modeling showing stronger resistive collimation in high-Z plasmas by Bell and Kingham[18] . In addition, the collimation did not rely on complex structured targets[71] or a double laser pulse configuration[72], as shown in recent experimental work. Kα fluorescence diagnostics directly characterized fast electron density distributions within the target. 2D collisional PIC simulation results are in excellent agreement with experiments and show the formation, in high-Z transport targets, of strong resistive magnetic channels enveloped by a global B-field that collimate initially divergent fast electrons. These magnetic channels extend into the subsequent lower resistance layers, maintaining the guidance of fast electrons.

5.2 Experimental Setup and Target Description

The experiment was performed using the Titan laser (150 J, 0.7 ps pulse duration, 17 mJ average prepulse pedestal energy in 2.3 ns, 1 μm wavelength) at the Jupiter Laser Facility, Lawrence Livermore National Laboratory. An f/3 on-axis parabola focussed the beam to a 10 μm (FWHM) spot with an incident angle of 17° onto the target front surface at $I_{peak} \sim 10^{20}$ W/cm^2. Figure 5.1 shows the target composition and its orientation relative to the laser beam and x-ray diagnostics.

The multilayer targets consisted of a common Al front layer (3 μm thick), a Z-transport layer made of either Au (8 μm), Mo (14 μm) or Al (33 μm) and a Cu tracer layer (22 μm) buried 110 μm behind the transport layer. The front Al layer provided an identical electron source for all targets. The areal densities of the Z-transport layers were 0.015 g/cm^2, 0.014 g/cm^2 and 0.009 g/cm^2 for Au, Mo and Al, respectively. The thicknesses of these layers were chosen to have similar shock transit times. This was to take into account the implosion driven shocks in the cone-guided FI scheme. The Cu tracer layer was used to characterize the fast electrons via Kα fluorescence. The transverse dimensions of these layers were 1 mm x 1mm. A final conductive carbon layer (1 mm thick, 10 mm x 3 mm in transverse dimensions) was used to minimize electron refluxing [73] in order to directly correlate the measured Kα signal to the fast electron forward flux.

5.3 Experimental Results

5.3.1 Bremmstrahlung Spectrometers

Data from the bremmstrahlung spectrometers was analyzed for each type of transport target as described in Section 4.3.2. The target and spectrometer response to electrons and photons, respectively, was modeled in ITS and a genetic algorithm (coded in MATLAB) determined the

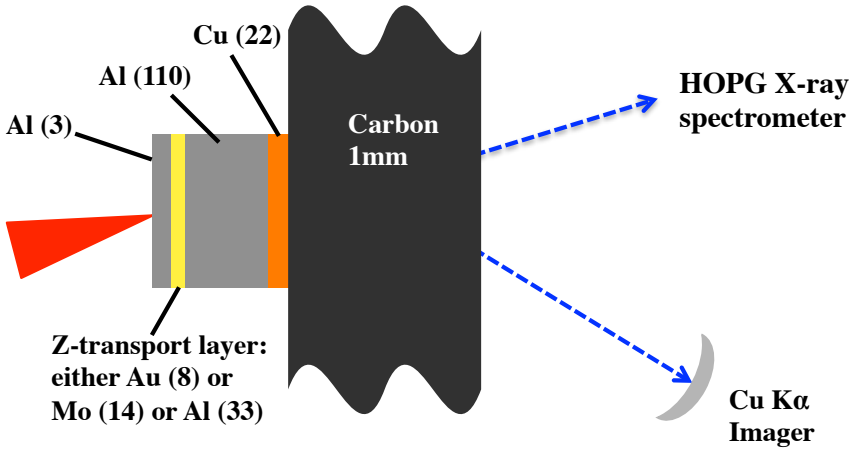

Figure 5.1: Layout of the target, laser and diagnostics. Target layer thicknesses are in μm. The laser was incident at 17° from target normal. The Kα imager was located 40° below the rear target normal and the HOPG x-ray spectrometer was 31° from the target normal in the equatorial plane.

electron spectra that best reproduced the data. Results for inferred laser energy-to-hot electron conversion efficiencies and average electron temperatures are shown in Fig. 5.2. Within experimental error, these parameters have the same value for all types of transport targets. In addition, the injected electron beam divergence angle was determined to be 50° for all cases, verifying that the initial Al target layer did indeed provide an identical electron source for all targets.

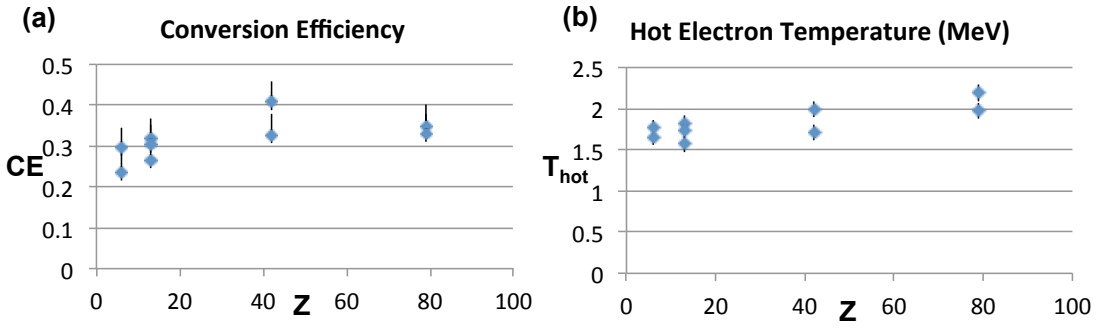

Figure 5.2: (a) Laser energy to hot electron conversion efficiency and (b) hot electron temperature vs target transport layer Z. Two data points per transport material were acquired.

5.3.2 Kα Radiation Diagnostics

The Cu Kα imager consistently recorded smaller emission spots from the Au and Mo transport layer targets as compared to the Al transport layer targets. Figures 5.3(a) and (b) show typical images for the Z = Au and Z = Al transport targets while Fig. 5.3(c) shows the corresponding radial Kα intensity profiles. Analysis of these profiles shows that the Kα spot sizes (FWHM) in Au (96 $\pm$ 20 μm) and Mo (84 $\pm$ 20 μm) cases are, on average, 36% smaller than that of the Al (140 $\pm$ 20 μm) targets, and the Kα signal reduction occurs mostly in the 1.2σ-2.2σ range (given a Gaussian distribution of $e^{-x^2/2\sigma^2}$.

Integrating under different parts of these curves allows us to look at spatial variations in the electron flux as a function of transport layer material. Within a 20 μm radius we calculate a 20% reduction of electron flux in the Au transport targets as compared to the Al transport targets. The lower and upper bounds of this reduction were 1% and 33%, respectively, given by the variation in the data as shown by the shaded area in Fig. 5.3(c). The same calculation for a 170 μm radius gives a reduction of 56% with bounds of 41% and 72%. Similar numbers are calculated for the Mo targets. The reduction in the integrated Kα signal at large radii is consistent with the reduction in the total Kα yield measured by the HOPG x-ray spectrometer as shown in Fig. 5.3(d). The Kα yield reduction by a factor of 2 cannot be explained simply by the increase of ionization energy in the high-Z material. Resistive stopping by strong resistive E fields and B-field trapping seem to be the main cause of the electron flux reduction in the high-Z transport material, as discussed in more detail below. It should be noted that signal variation (20% reduction) in the central 20 μm radius region is within our measurement error. It is reasonable to say, then, that although the total Kα yield from the entire target is reduced for the Au and Mo transport targets, Kα signal (and therefore fast electron flux) in a central 20 μm radius spot remains the same for all targets.

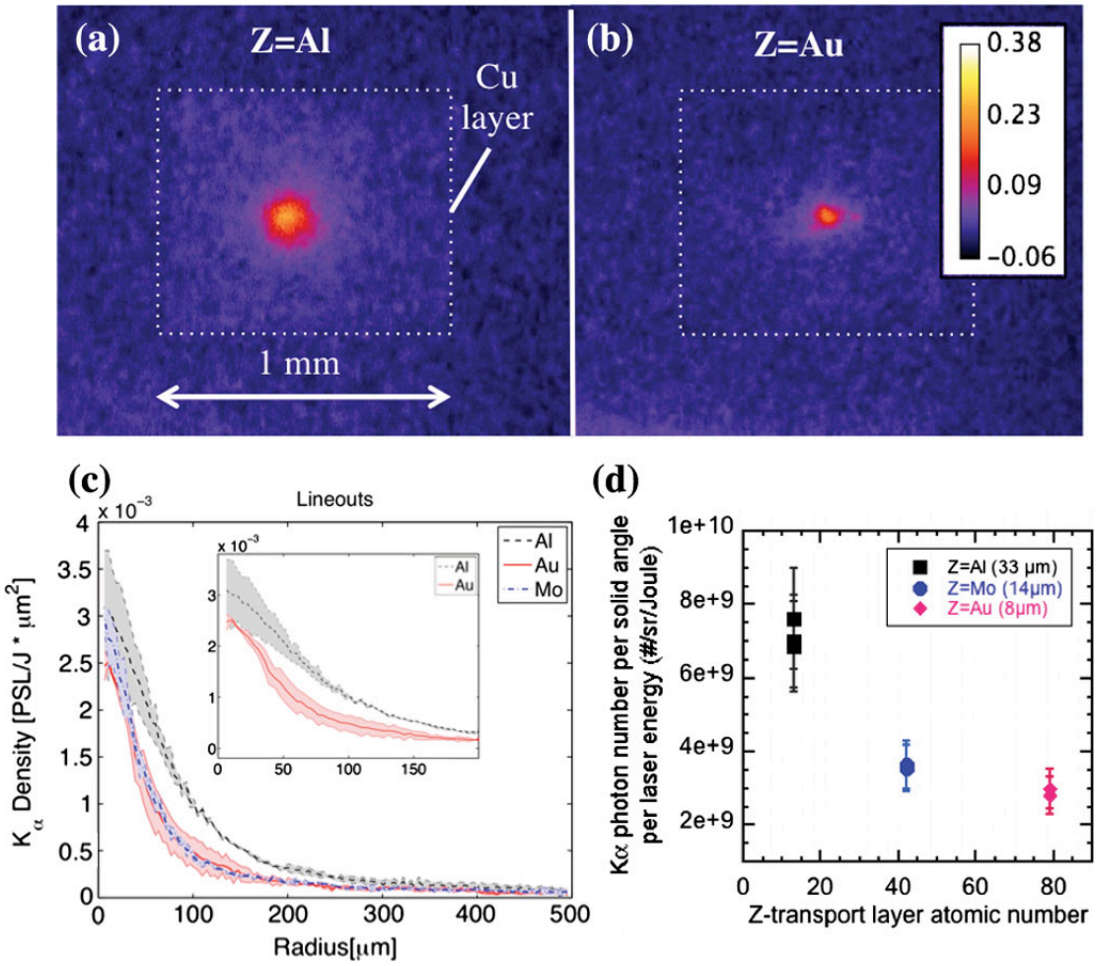

Figure 5.3: Cu Kα images (a) and (b) from Z = Al and Z = Au transport targets, respectively, the corresponding lineouts (c), and the total integrated Kα yields (d) from the HOPG x-ray spectrometer for three types of transport targets. The images have the same spatial and color scales. Kα intensity is normalized to the laser energy in (c) and to both the laser energy and solid angle in (d). Lineouts in (c) in bold are averaged over two data points per material. The shaded area between raw data lineouts (lighter lines) shows variation in data. Inset shows Z = Al and Z = Au lineouts only in a zoomed-in region of interest.

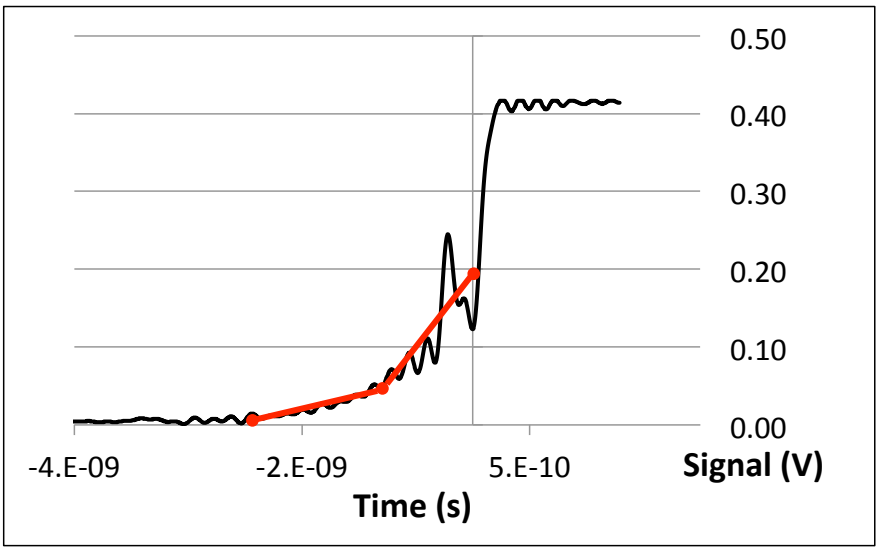

Figure 5.4: Experimentally measured prepulse trace (black) and linear approximation used in HYDRA (red).

5.4 Pre-Plasma Simulations

The pre-plasma created by the interaction of the laser prepulse and the target is important to characterize as it interacts significantly with main pulse. To do this the radiative hydrodynamic code HYDRA, described in Chapter 3, was used.

A 30 μm x 500 μm solid Al slab was placed in a 1 mm x 500 μm simulation region surrounded by low density helium gas. The initial density and temperature of the Al (He) was 2.69 (5.0e-7) g/cc and 2.5e-5 (2.5e-4) KeV, respectively. The Al slab was irradiated with a 17 mJ laser pulse with a spatial distribution given by the sum of two Gaussians with a FWHMs of 7.5 μm and 15 μm. Each Gaussian contained 50% of the energy pulse energy. The temporal shape of the pulse is shown in Fig. 5.4. The experimentally measured prepulse was approximated in HYDRA with a linear fit using 3 data points.

LEOS equation of state tables were used for both Al and He and 16 radiation bins were used for the radiation transport. The electron density profile of the preplasma at the end of the simulation (t = 2.3 ns) is shown in Fig. 5.5. The high density Al slab can be seen in red along

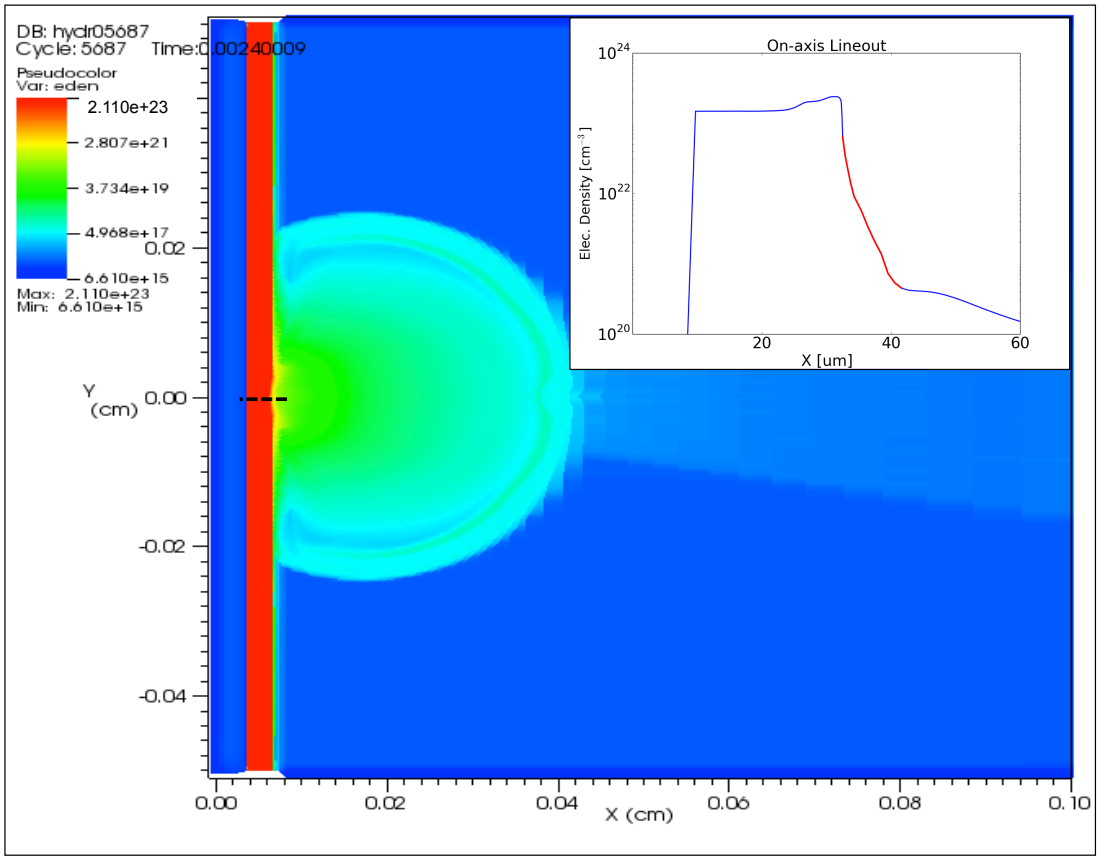

Figure 5.5: Electron density contour plot of preplasma predicted by HYDRA at t = 2.3 ns, where the laser propages from right to left. Dotted black line indicates where on-axis lineout was taken. Inset shows the lineout in blue with the portion used in LPI simulations highlighted in red.

with the expanding preplasma off the front surface. The inset shows an on-axis lineout of the electron density. Note the critical density ($\approx 10^{21}$ g/cc for 1 μm light) has moved ≈ 5 μm away from the front surface of the Al and the preplasma density remains high enough to affect laser propagation much farther away. Due to computational limitations, only the first 10 μm of the preplasma is modeled in the LPI simulations described in Section 5.5

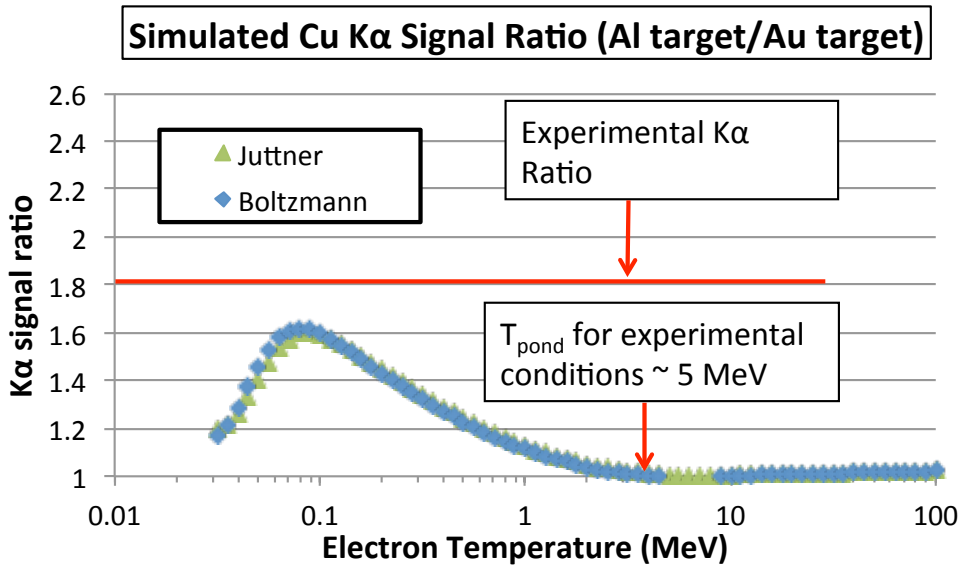

Figure 5.6: Simulated Cu Kα signal ratio in for Al vs Au transport targets. Ratios are shown for 2 types (Juttner, Boltzmann) of injected electron energy distributions and a large range of average temperatures. The experimentally measured ratio is marked with a red line, and the ponderomotive electron temperature predicted using experimental laser conditions is noted.

5.5 LPI and Transport Simulations

5.5.1 ITS Simulations

Monte Carlo simulations using the code ITS 3.0 were used to examine the effects of transport *without* field effects in the Al and Au transport targets. These simulations were quick and straightforward, and provided a good check of whether relativistic drag and scattering alone could explain experimental results. Electron spectra with two different energy distributions (Maxwell-Boltzmann, Juttner) were injected into Al and Au transport targets with a divergence angle of 50° (determined from bremmstrahlung spectrometer results, see Section 5.3.1) and wide range of temperatures. The total yield of Kα photons from the Cu fluorescence layer was calculated.

Figure 5.6 shows a plot of the simulated Cu Kα yield ratio (Z = Al / Z = Au) vs injected electron beam temperature. Given the laser conditions of the experiment, we expect an average

electron temperature near $T_{pond} \approx 5$ MeV. The simulation results shows that the difference due to scattering of Kα yields for the Al and Au targets is negligible for temperatures near T_{pond}. Even with very cold, unrealistic electron beam temperatures (≈ 0.1 MeV) for which scattering would be play a dominant role in transport, the simulated Kα yield ratio is less than the experimentally measured ratio. Thus more complicated field effects were determined to be at play in this experiment.

5.5.2 PICLS Simulation Setup

To understand the underlying transport physics in this experiment, 2D collisional PIC simulations were performed using the PICLS code[47] described in Chapter 3. Simulations included dynamic impact ionization, radiative losses and a relativistic binary collision model that incorporates collisions between free-free and free-bound electrons (particularly necessary to accurately reproduce energy transport in a high-Z partially ionized medium). Due to limited resources, only reduced-scale sections of the experimental targets for the two extreme Z values (Al and Au) were modeled.

A Gaussian (spatial and temporal) laser pulse with 1 μm wavelength, 726 fs pulse duration and a peak intensity $\sim$9x10^{19} W/cm^2 in a 10 μm focal spot was normally incident on the target front surface. The targets had a transverse dimension of 160 μm with layers of (I) Al + Z (Al) + Al, each with uniform density and thicknesses of 3 + 33 + 4 μm or (II) Al + Z (Au) + Al, also uniform, with thicknesses of 3 + 8 + 9 μm. Absorbing boundary conditions were applied for fields and particles (i.e., no fast electrons recirculated back into the target). The front target surface was preceded by a 10 μm long Al preplasma with a density that varied from 2x10^{20} to 1.2x10^{22} cm^{-3} with a 1/e scale-length of 2 μm. This density profile was obtained from the HYDRA simulations described in Section 5.4. The ion density for Al (Au) was set to 56 n_c (50 n_c) according to its mass density, 2.7 g/cc (19.7 g/cc), where n_c is the critical density for 1 μm wavelength light. The initial ionization state was set to +3 (+4). The mass of the Al (Au) ion

used in calculations was 27 M_p (179 M_p) where M_p is the proton mass. The simulations used a spatial (temporal) resolution of 0.017 μm (0.055 fs or 1 laser cycle). Initially all particles were at rest with the plasma temperature set to zero.

5.5.3 Electron Energy Density

We first examine electron flux predictions for comparison with the experimental Kα data. Contour plots of the electron energy density at the end of the simulation in Fig. 5.7(a) and (b) show clear agreement with experimental trends, i.e. smaller beam divergences for Au transport targets. Using a spatially resolved plot of electron number time integrated over the entire simulation (Fig. 5.7(c)), we calculate the ratio of the FWHM of the Al target distribution to that of Au to be 1.47, in excellent agreement with the experimental Kα spot size ratio of 1.5. In addition, simulations predict the same collimation effect in the Au transport target as seen in experimental data: a reduction of electron flux occurs outside a central 20 μm radius spot while flux inside this spot is maintained. Note the strong deformation of the critical density surface in the contour plots. For the Al target, this deformation causes a large beam divergence [32] and, though weak filamentation is evident, electron energy is distributed more or less uniformly throughout the beam. In contrast, the Au target shows strong filamentation in the central regions of the Au transport and Al propagation layers. Though we also see the same high energy density near a deformed critical surface, we observe a relatively narrow beam. Fig. 5.7(d) shows the significant reduction in propagation angle for electrons in the Au target within a central region.

5.5.4 Azimuthal Magnetic Field and Resistivity Evolution

The observed difference in fast electron beam transport can be explained by the corresponding self-generated resistive magnetic fields as a result of different resistivity evolutions in these two types of targets. The growth of the self-induced magnetic field is determined by the

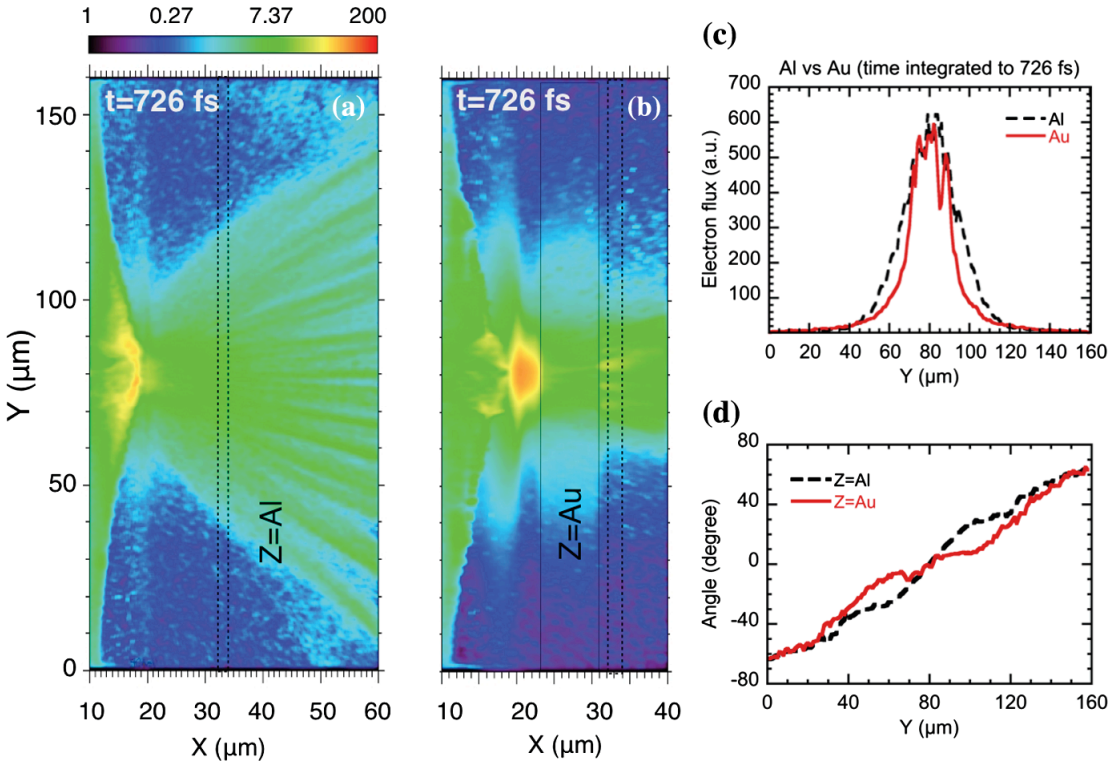

Figure 5.7: Electron energy density contour plot of (a) Al and (b) Au targets at the end of the laser pulse (726 fs). The plot shows electrons in the preplasma region (starting with X=10 μm) and target. For spatially resolved (Y direction) (c) electron flux and (d) mean propagation angle plots, electrons >100 keV were sampled in a 160 μm wide, 2 μm width thick box marked between the dashed lines in (a) and (b).

equation $\frac{\partial \mathbf{B}}{\partial t} = -\nabla \times \mathbf{E} = -\nabla \times (\eta \mathbf{J_r})$, where $\mathbf{J_r}$ is the return current excited to neutralize the fast electron current ($\mathbf{J}$) and η is the background plasma resistivity. In our simulation geometry, the dominant terms for azimuthal B-field generation are given by

$$\frac{\partial \mathbf{B_z}}{\partial t} = \mathbf{J_x}\frac{\partial \eta}{\partial y} + \eta \frac{\partial \mathbf{J_x}}{\partial y}. \tag{5.1}$$

Note that the resistivity in PICLS results from binary collisions between different particle species and follows the Spitzer behavior ($\eta \propto Z^*/T^{3/2}$), but with the collision frequency in cold plasma ($<$10 eV) kept at a constant for a degenerate plasma [47]. Fig. 5.8 compares the quasi-static azimuthal B_z fields in Al and Au transport targets at both an early time (198 fs) and later time (end of the laser pulse, 726 fs). Note that a high-intensity-laser-produced fast electron beam (> Mega-Ampere current) is subjected to the resistive filamentation instability when traveling through a charge and current neutralizing background[19]. This instability tends to destroy the local current neutralization causing the beam to breakup into multiple self-guided current channels. At an early time (198 fs), similar diverging electron beam and filamented field structures (Fig. 5.8(a) and (b)) are observed in both Al and Au transport targets. With the rapid ionization and heating of the Al target, the resistivity drops in the center region where current density is high and thus the two terms on the RHS of Eq. 5.1 oppose each other and limit field growth. Relatively weak magnetic fields ($B_z \approx 5$ MG) allow the fast electron beam to continue to propagate ballistically inside the Al target maintaining its source divergence over the laser duration, as shown in plots of B_z (Fig. 5.8(c)) and electron energy density (Fig. 5.7(a)). This is consistent with the fast electron mean propagation angle plot in Fig. 5.7(d) showing that the fast electron beam spreads out with propagation distance inside the Al transport target.

In contrast, plasma resistivity and B-field dynamics are more complex in the Au transport target. Due to large heat capacity and high atomic number, Au plasma resistivity in the center of the high current remains high and the resistive field growth is dominated by the first term of

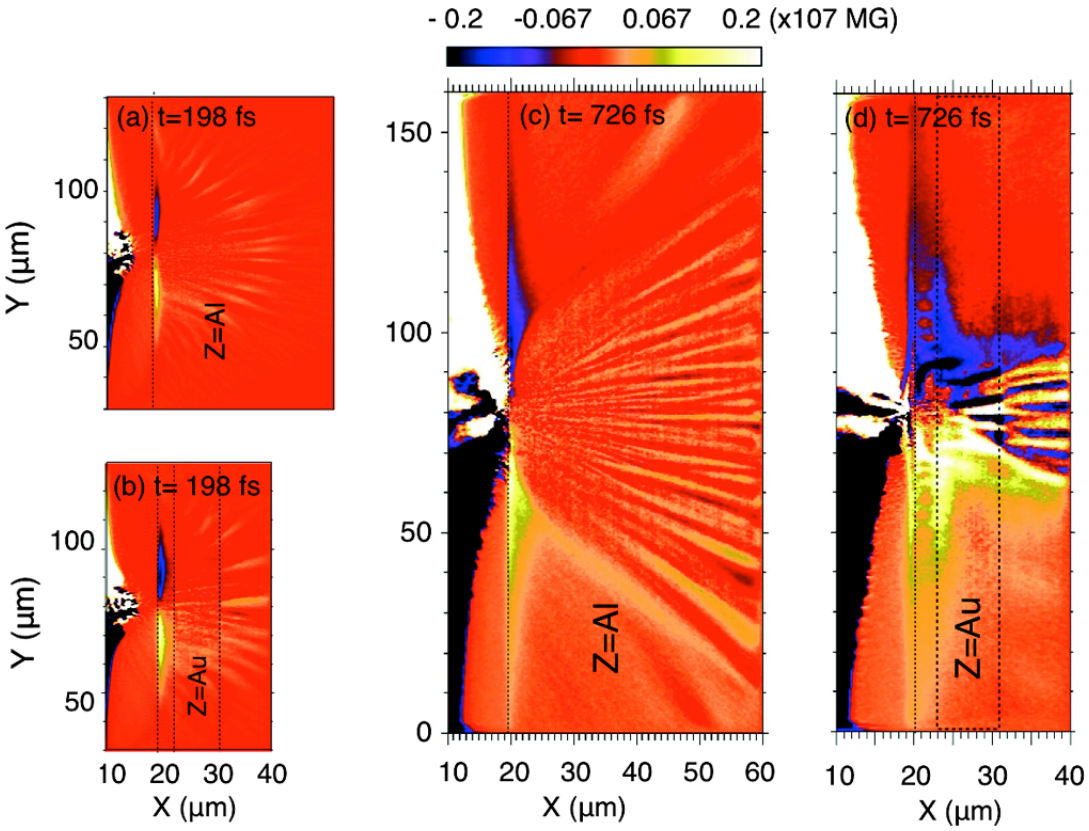

Figure 5.8: Contour plots of the quasi static magnetic fields (a), (b) at 198 fs and (c), (d), at 726 fs for Z = Al and Z = Au transport targets, respectively.

the RHS of Eq. 5.1. Resistive magnetic fields as strong as 60 MG are produced when the laser pulse is still at its rising stage near the peak intensity. In such intense fields the Larmor radius, r_L (μm) $\approx 30\ E_{MeV}/B_{MG}$, of 3 $\approx$ MeV electrons is 1 μm. Thus, we expect significant guiding and collimation of fast electrons in the magnetic channels. This is indeed evident in Fig. 5.8(d) where we observe a few current channels of width $\approx$ 3 μm in the Au layer. These magnetic channels extend further into the following Al propagation layer and continue to confine and guide subsequent electrons. By the time the laser interacts with its peak intensity, the majority of fast electrons flow through the center region, i.e., Y $\approx$ 60 - 100 μm. The confined flow of electrons in the center gives rise to a large transverse current gradient, that, combined with a high resistivity in Au, produces a global azimuthal field (30 - 50 MG) that acts to further collimate fast electrons. It is also noted that at later time, strong B_z fields (50-60 MG) due to the resistivity gradient $\partial B_z/\partial t = J_y(\partial\eta/\partial x)$ [74] are also observed at the Al-Au interface that are favorable for collimating the later arriving electrons. The cumulative effect of magnetic field induced collimation is clearly seen in Fig. 5.7(c) and Fig. 5.7(d) where the fast electron beam has a narrow spread with a reduced angular spread.

5.5.5 Time Resolved Electron Flux

As discussed above and shown in Fig. 5.7(c), fast electron flux (time integrated over the laser duration) in the central 20 μm radius region after the Au transport layer is at a similar level to that in the Al target. Detailed examination of the time-resolved electron flux data in the simulations suggests a rather more dynamic evolution. Figures 5.9(a) and (b) show comparison plots of the spatially resolved electron flux, time integrated up to 264 fs and 396 fs, respectively. At 264 fs, before the peak of the laser pulse, the transverse distribution profiles for the Al and Au targets are very similar with a slightly higher electron flux in the center region for the Al case, potentially due to stopping of relatively lower energy fast electrons produced at the rising edge of the laser pulse by collisions and drag in the high-Z Au layer. Just after the peak of

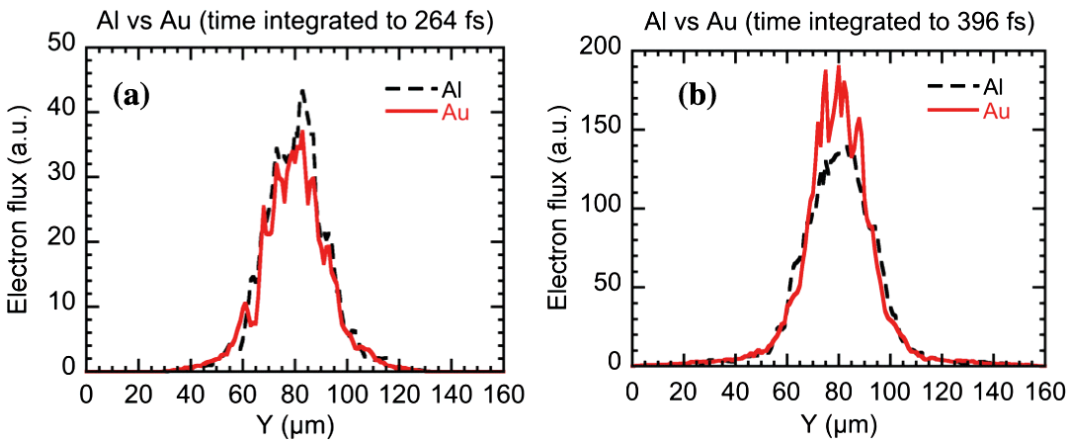

Figure 5.9: Time integrated electron flux distributions from the sampling box for Al and Au targets up to (a) 264 fs (before the peak intensity) and (b) 396 fs (at the laser pulse peak).

the laser pulse at 396 fs (Fig. 5.9(b)), guiding magnetic channels in the Au target are well established and electron flux in the central region of the target exceeds that in the Al case. The observed modulation in electron flux distribution also correlates well with the magnetic channel structure. During the falling edge of the laser pulse, fast electron flux through the center of the Au target drops below that in the Al target potentially due to both strong resistive electric field inhibition and the magnetic mirror effect, again particularly stopping low energy electrons. This is consistent with the observed strong localized energy deposition in the front Al layer of the Z=Au transport target in a small central region (Fig. 5.7(b)). As a result, over the whole duration of the laser pulse (726 fs), electron flux remains similar to that in the Al case.

The PICLS simulated reduction (24%) in total number of electrons in the Au transport target is smaller than what observed in the experiment (56% reduction in total Kα yield). There are several reasons that may contribute to this difference. The simulations were performed in a 2D Cartesian geometry using a simple Gaussian intensity distribution in a 10 μm spot and a temporal pulse shape with a relatively sharp rise (330 fs), which is quite different from a real 3D experiment. A more accurate laser intensity distribution $I(r,t)$ characterized on full energy shots shows a much larger low-intensity wing region in the focal spot and also a longer pulse

rise time[75]. Including the wings (spatial and temporal) of the pulse while still injecting the same total energy in simulations would result in more low energy electrons that would be more effectively stopped in the Au transport target. In the experiment there is also an additional 100 μm Al propagation layer between the Z-transport layer and the Cu tracer layer, which is beyond our computational capability. Nonetheless, the trend is well established and the simulated spread of the time integrated electron beam flux is in excellent agreement with the experiment.

5.5.6 Summary

In summary, it has been directly shown that fast electron transport inside solid targets strongly depends on the transport material. A high- or mid-Z transport layer a few μm beneath the front low-Z interaction layer collimates fast electrons, as compared to a low-Z aluminum transport layer, and maintains the electron flux within a 20 μm radius central spot. 2D collisional PIC modeling results are in excellent agreement with the experiment and show that resistive field effects, rather than scattering, dominate fast electron transport. Strong resistive B-field channels and global fields can confine and guide fast electrons with an initially large divergence. This work is very promising for cone-guided FI and provides a good foundation for future studies employing different transport and source layer materials. In addition, it has important implications for FI relevant pulse conditions where a higher flux of electrons could be transported to the fuel core via the guiding magnetic channels formed during the leading edge (with the sub-ps time scale) of the 10 ps high intensity pulse.

Chapter 5, in part, is a reprint of material as it appears in S. Chawla, M.S. Wei, R. Mishra, K.U. Akli, C.D. Chen, H.S. McLean, A. Morace, P.K. Patel, H. Sawada, Y. Sentoku, R.B. Stephens, F.N. Beg, Physical Review Letters **110**, 025001 (2013). The dissertation author was the primary investigator and author of this paper.

Chapter 6

ZUMA Transport Simulations

6.1 Introduction

For fast ignition, we seek to maximize the amount of electron energy flux at some distance from the electron source. In the previous chapter, we determined that resistive magnetic fields can form in high atomic number materials during fast electron transport that can collimate the electrons while maintaining electron flux levels comparable to low atomic number materials. Though the fields in Au were strong enough (see Fig. 5.9) to yield a higher flux level than in Al at early times during the pulse duration, the final flux levels in both materials were equivalent, likely to due to higher stopping and deposition in Au. These results illustrate the dynamic competition between two transport mechanisms that are essential to understand in order to optimize electron flux levels: deposition and collimation. Moreover, they motivate further study of how resistive magnetic field growth depends on material properties, and which materials have an optimal balance of stopping and collimation for fast electron transport.

In this chapter, we will thoroughly investigate the physics of these two mechanisms in various materials at Titan-like conditions. For collimation, we will examine the temporal and spatial evolution of magnetic fields and the origin of magnetic field growth rates. For deposi-

tion, we will examine how various energy electrons deposit their energy and which deposition mechanisms dominate transport.

This will be accomplished with the hybrid-PIC code ZUMA described in Chapter 3. ZUMA's physics models are consistent with fast electron transport problems and the code can run simulations at large spatial and temporal scales much faster than PIC codes. Other computational studies of transport using hybrid-PIC codes [76–78] have used simplified physics models (such as fixed ionization state), non-Titan like conditions and/or simplified electron sources. Honrubia [21] uses a Titan-like electron source with a time dependent energy/angle distribution but, as with the other studies, does not include a detailed comparison of the dynamics of field growth, resistivity, ionization and temperature between different materials. In this work, we use electron source parameters determined by the PICLS simulation previously discussed along with a time-dependent electron energy distribution to investigate and compare deposition and collimation in Al, Cu, Ag and Au.

6.2 Simulation Setup

ZUMA was run in an RZ geometry with a mesh size of 0.4 μm. The simulation domain ranged from 0 - 80 μm in r and 0 - 160 μm in z. The run time was 2.2 ps with a temporal resolution of 0.5 fs. A fast electron source was injected at z = 80 μm into four different background materials: Al, Cu, Ag and Au. All materials were initialized to a temperature of 0.1 eV at solid density, and the magnetized LMD model (see Sec. 2.3.5) was used in Ohm's Law.

Sec. 3.3.1 describes generally how ZUMA injects fast electron particles into a simulation region. Laser intensity parameters, electron energy and angular injection distributions must be supplied so that particle weights, energies and injection angles can be correctly calculated at every time step. The required parameters were obtained from the injection parameters and particle data associated with the PICLS simulation described in Sec. 5.5.2. The intensity parameters used

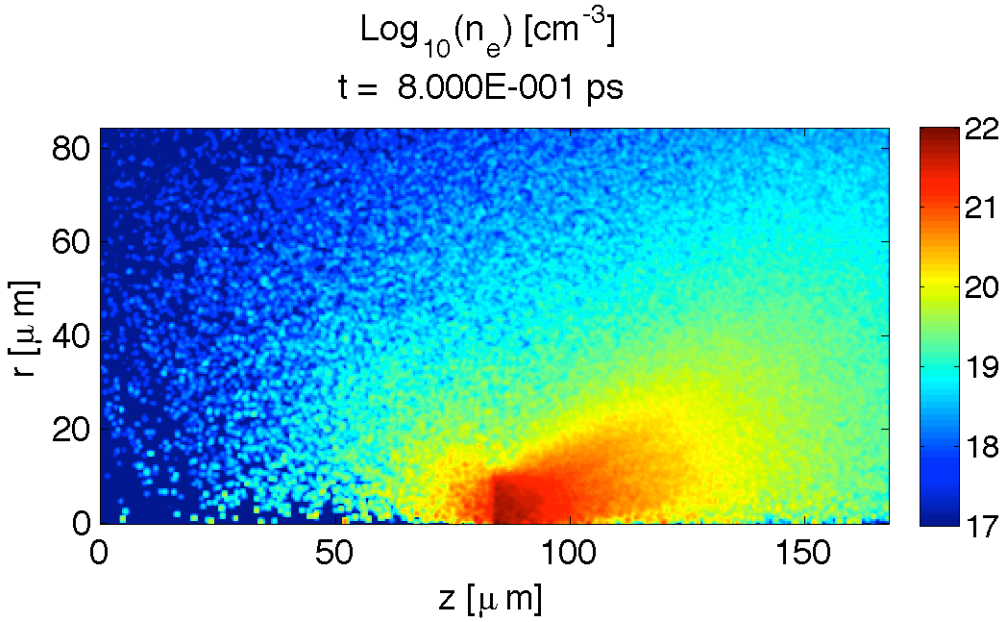

Figure 6.1: Sample electron energy density contour plot for Ag.

were the same as those used for the laser: λ = 1 μm, I_0 = 9x10^{19} W/cm^2, σ_r = 4.25 (FWHM = 10) μm, σ_t = 0.31 (FWHM = 0.73) ps. This resulted in a fast electron beam with a total energy of 55 J and average current of 10^{13} A/cm^2. Approximately 5.6x10^5 macroparticles were injected (averaged over all simulations), weighted to represent 2x10^{14} electrons. Electrons were injected at radii $r \leq 10$ μm according to a Gaussian radial distribution with σ_{HWHM} = 5 μm. The pulse peak time was set to 0.8 ps. Figure 6.1 shows an example of electrons propagating through a Ag target at the peak pulse time.

The PICLS particle data included snapshots every 33 fs of position, velocity and weight for each laser-produced electron macroparticle in a 1 μm thick (X-direction) box located 1 μm away from the injection plane. From this data, mean particle energy and propagation angle distribution vs time were evaluated. The formula $E_{mean} = 1.25T_{hot}(t)$, where T_{hot} is defined by Eq. 2.33 and t is time, was found to fit the mean particle energy vs time data well. This formula

was then used to define a temporally dependent electron energy distribution

$$\frac{dN}{dE} = e^{-E/E_{mean}(t)}.$$

The particle data also showed the 99% of electrons produced were in the energy range of 10 keV to 27 MeV, so these limits were chosen for injected particles in ZUMA. The resulting, time-integrated electron spectrum injected for all simulations is shown in Fig. 6.2.

The propagation angle distribution was found not to vary much with time, so for simplicity a non-time dependent distribution that fit the particle data well was used:

$$\frac{dN}{d\theta} = e^{-(\theta/\theta_{mean})^4},$$

where $\theta_{mean} = 54.8^\circ$. ZUMA was set to output various data every 50 fs for post-processing and analysis. These included fields, resistivity, current density, temperature and ionization state as functions of space and time.

6.3 Results and Discussion

6.3.1 Deposition

We begin our discussion of simulation results with an examination of relativistic electron deposition throughout the background material. Figure 6.3 shows deposition normalized by total injected electron energy vs. time.

Deposition is greatest in Au, followed by Ag, Cu and finally Al. During the first half of the injected electron pulse deposition is very similar in Al, Cu and Ag ($\sim$8-10% at I_peak) and slightly higher for Au ($\sim$15%). After the pulse peak, deposition for Al, Cu and Ag continues to grow approximately linearly reaching values of $\sim$15-19% at the at the falling edge FWHM

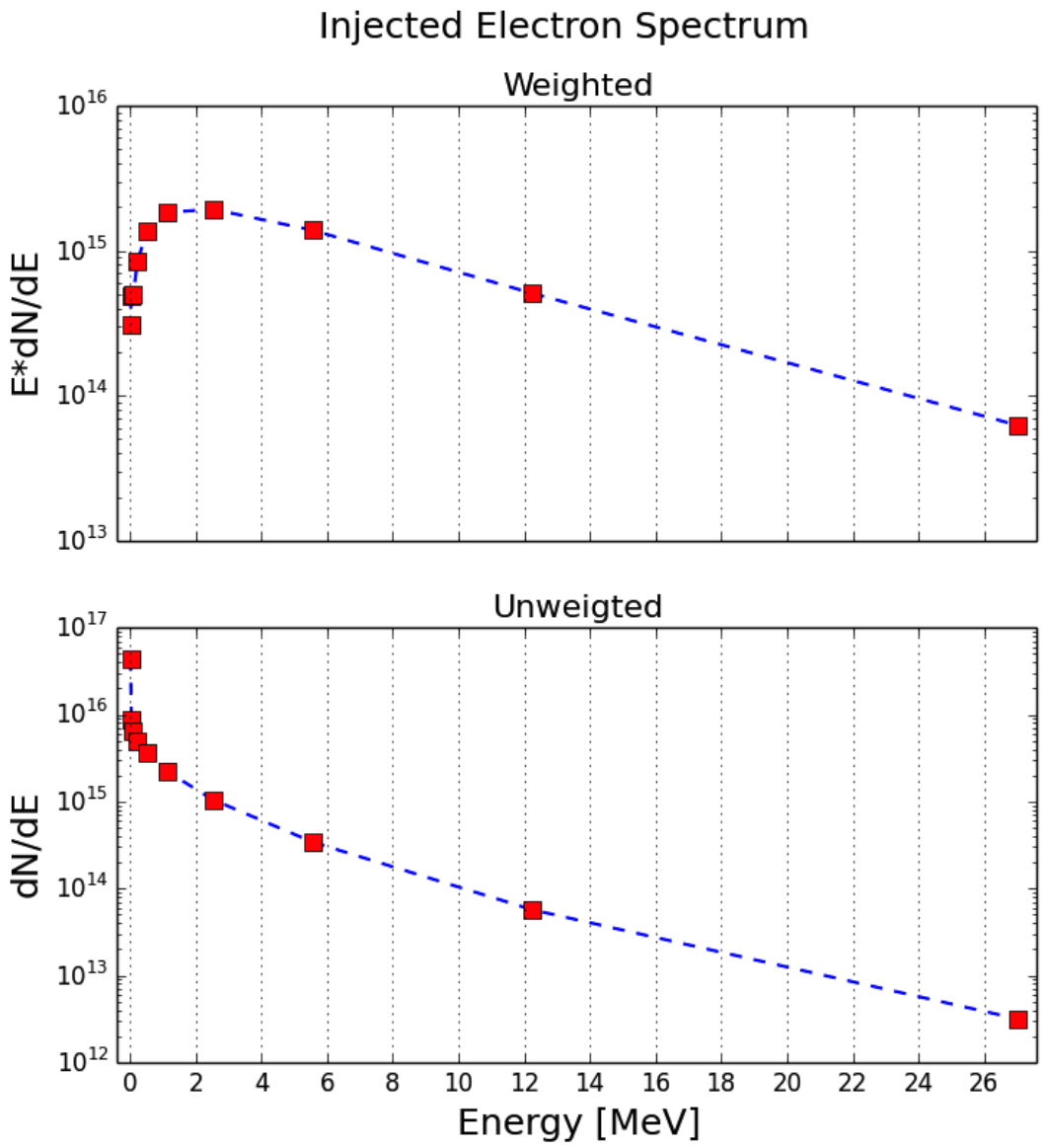

Figure 6.2: Injected electron energy spectrum, red squares indicate amount of injected particles per energy group and are plotted at the upper bound of each group. The top plot shows the spectrum weighted by energy while the bottom shows the raw number density.

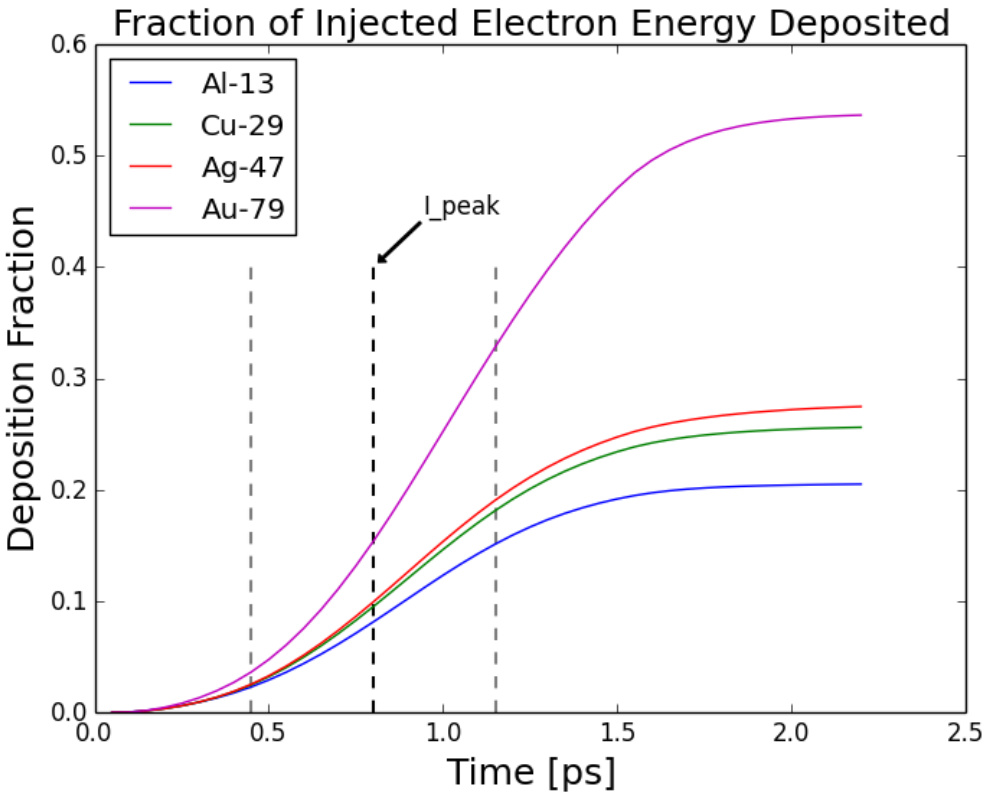

Figure 6.3: Total deposition normalized by total injected fast electron energy (54.63 J in this case). The dotted line labeled I_peak denotes the peak intensity time of the injected electron beam and the unlabeled dotted lines denote the temporal FWHM locations of the beam (Gaussian shape). Legend entries give material atomic weights.

Table 6.1: Total (total deposition normalized by injected electron energy) and Collisional (collisional deposition normalized by total deposition) Deposition Fractions for all materials at the end of the simulations.

	Total Deposition Fraction	Collisional Deposition Fraction
Al	21%	19%
Cu	26%	40%
Ag	26%	44%
Au	54%	91%

time. Deposition in Au, however, increases nonlinearly to around double these values (33% at the same time). Deposition in all materials flattens out around 1.5-1.7 ps, attaining values summarized in the first column of Table 6.1.

We can break down total deposition by the physical mechanisms of collisional and ohmic (or collective, see Chap. 2) stopping. Figure 6.4 shows collisional deposition for each material as a function of time, normalized by the total deposition. The shapes of the curves are similar to those for total deposition with larger differences in deposition fractions for most times. Collisional deposition constitutes less than half of total deposition in Al, Cu and Ag at all times and for most of the pulse duration in Au, **implying that ohmic stopping is the dominant mechanism for slowing down relativistic electrons** in all materials at Titan-like conditions (see second column of Table 6.1). Note that collisional deposition at the end of the simulations depends on target size and simulations time. For a very large simulation region and long simulation time, electrons would continuously deposit energy via collisions long after the end of the pulse as they travel ballistically through the material. Thus, when considering the importance of collisional deposition one should be aware of the travel time and distance scales of the electrons involved.

Deposition values can also be broken down by relativistic electron energy group (see diagnostic description in Sec. 6.2). Figure 6.5 shows a stackplot of the fractional energy deposited by various electron energy groups as a function of time for each material, normalized by the total energy deposited over the entire simulation. For all materials, the three groups of electrons with energies between 0.52 and 5.56 MeV deposit the most energy. Table 6.2 summarizes the

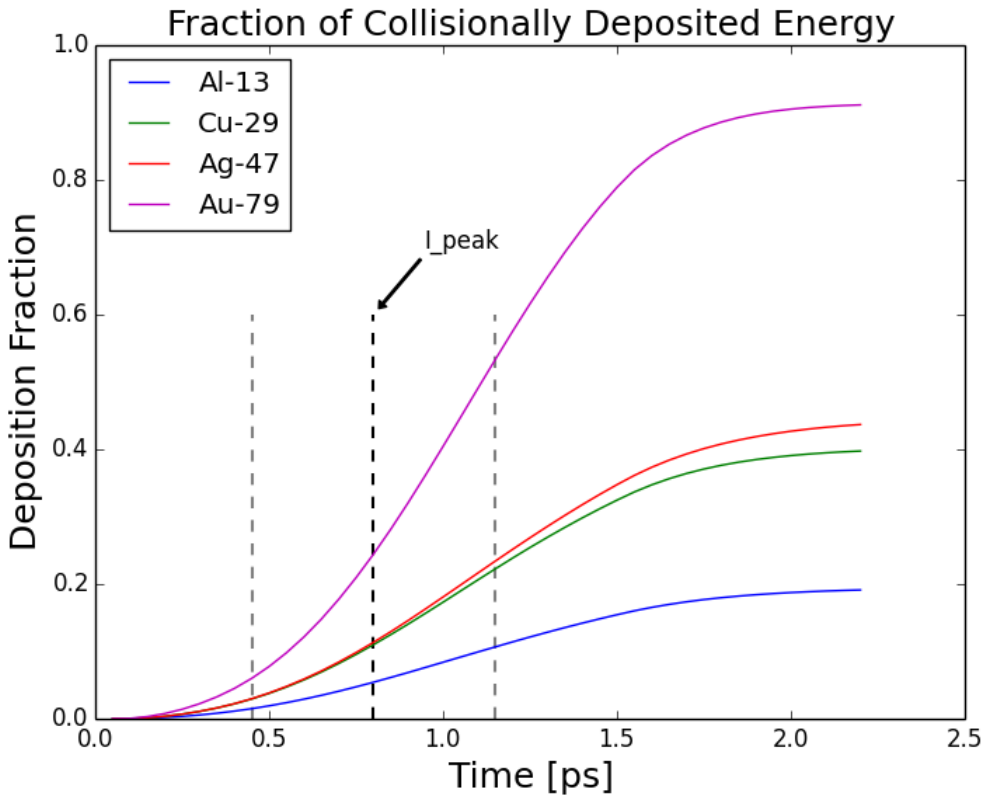

Figure 6.4: Collisional deposition normalized by total deposition (ohmic + collisional).

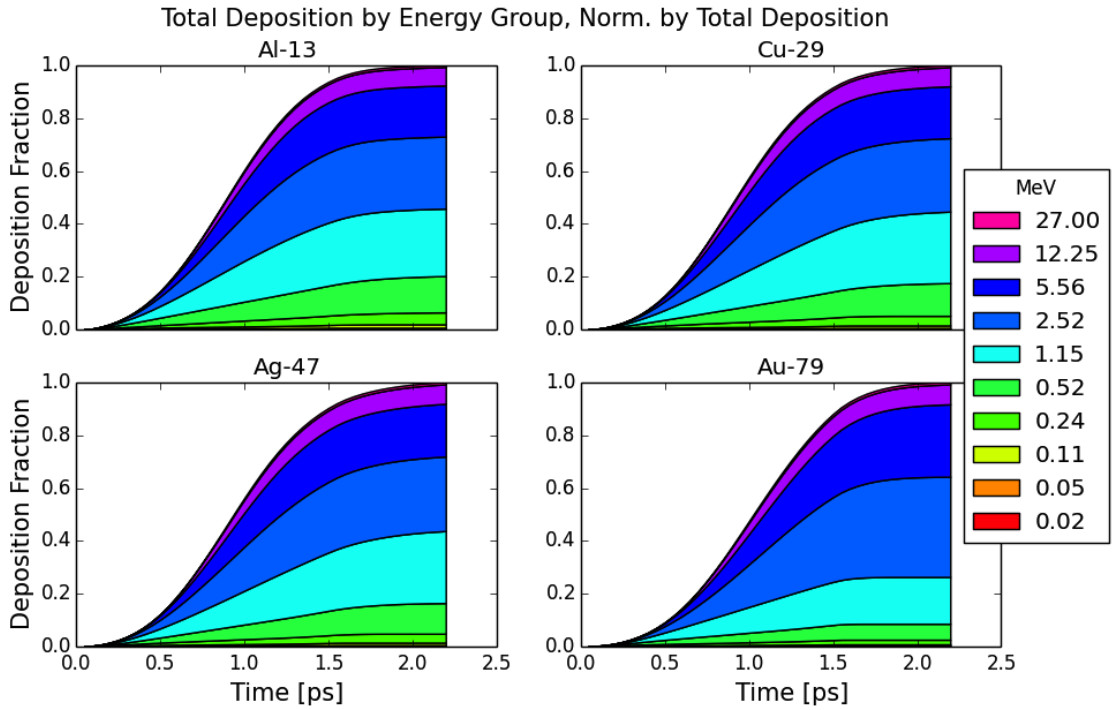

Figure 6.5: Total deposition per electron energy group normalized by total energy deposited. The areas of the colored bands correspond to energy group fractions and are stacked according to the order shown by the legend. Labels are upper bounds of energy bins.

results. Note values are very similar for Al, Cu and Ag, clearly indicating that varying between these materials has little effect on electron deposition. Deposition in Au is different as 18% less energy is deposited by electrons < 1.15 MeV and 18% more for 1.15 - 5.56 MeV electrons.

This difference can be explained by examining a stackplot for the fractional collisional energy deposited by each energy group, normalized by the total collisional energy deposited (Fig. 6.6). For Al, Cu and Ag, electrons with energies < 1.15 MeV are responsible for a majority

Table 6.2: Total deposition by energy group, normalized by total energy deposited for all materials at the end of the simulations.

	< 0.52 MeV	0.52 - 1.15	1.15 - 2.52	2.52 - 5.56	5.56 - 27
Al	20%	26%	27%	19%	8%
Cu	17%	27%	28%	20%	8%
Ag	17%	27%	28%	20%	8%
Au	8%	18%	38%	27%	8%

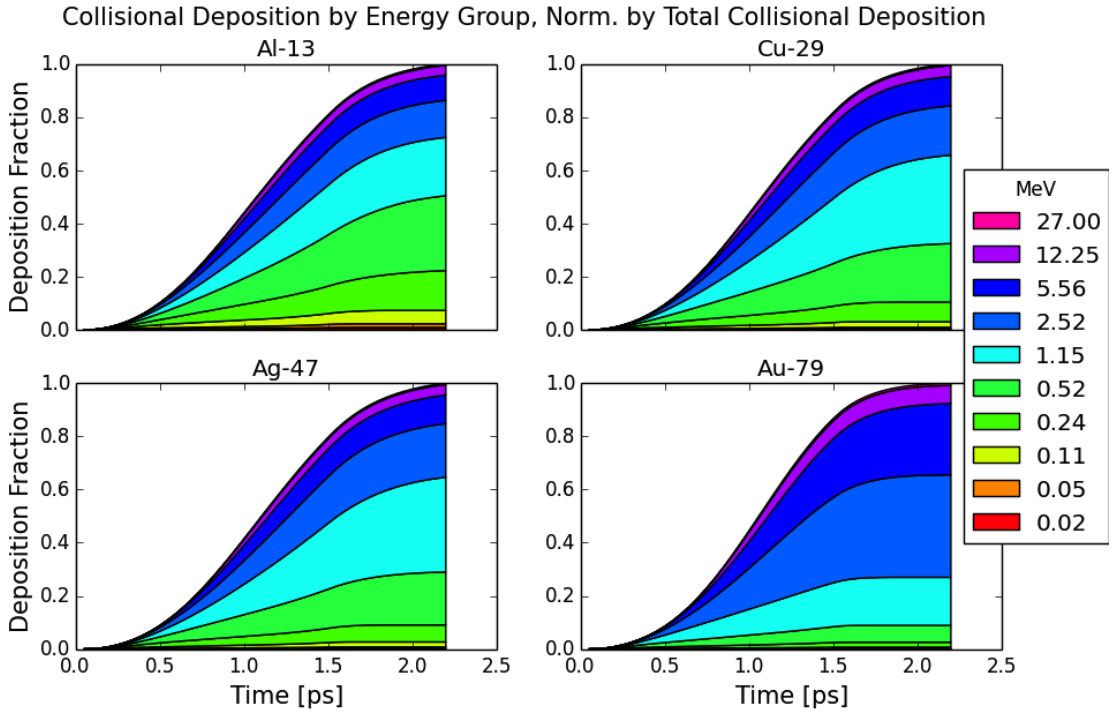

Figure 6.6: Collisional deposition per electron energy group normalized by total collisional energy deposited.

of the collisional deposition throughout the target. In the case of Au, however, 1.15-5.56 MeV electrons collisionally deposit the most energy, thus accounting for the 18% difference. As mentioned previously, the amount of collisional deposition in these simulations is dependent on target size. However, these results are important because they suggest that **1.15 - 5.56 MeV electrons become more sensitive to collisional stopping in large size targets with high atomic number materials**.

To summarize deposition results, though deposition of initial electron beam energy is lowest in Al, as expected, it is not significantly lower than that in the mid-Z materials of Cu and Ag. The major change is the fraction of energy deposited collisonally versus ohmically, though ohmic dominates for all materials at most times. Furthermore, various electron groups behave very similarly in terms of total deposition for all three materials. Au deposits almost double of its energy compared to other materials and half of it is collisional.

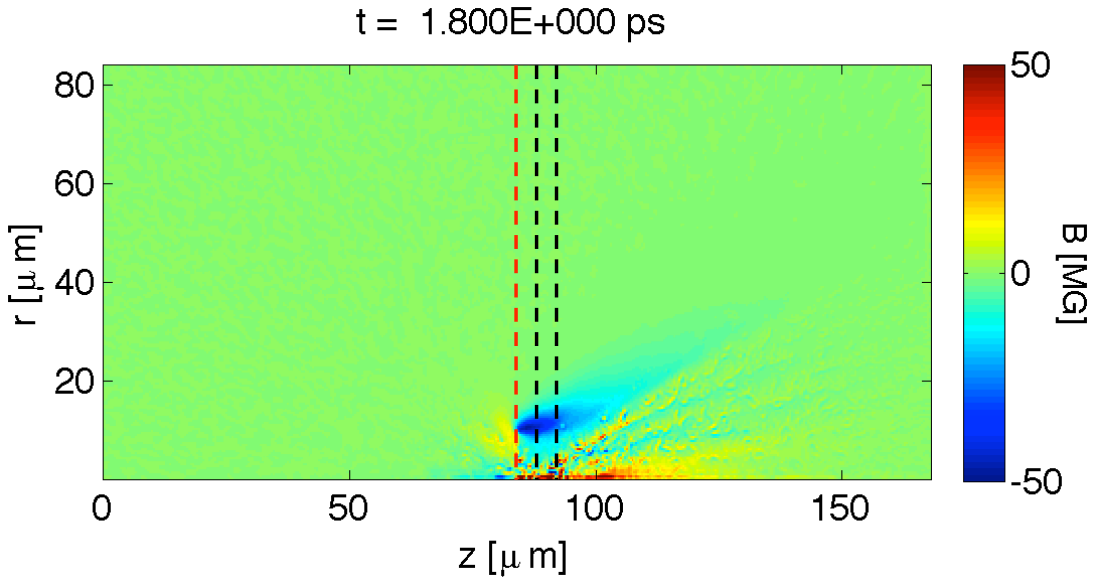

Figure 6.7: Sample magnetic field contour plot (B_θ) for Ag at t=1.8 ps. The red line indicates the injection z-plane and the and black lines the radial lineout z-planes for the plots in Fig. 6.8.

6.3.2 Magnetic Fields

Figure. 6.7 shows a sample magnetic field contour plot (B_θ) for the Ag simulation after the end of the injection pulse. There is very strong, global field near the electron beam edge within the first 20 μm of the injection location present, as well as thinner, weaker magnetic filaments within the beam due to beam filamentation[19]. These two features are common to all material simulations. The global field vector has a direction out of the page and can, therefore, bend electrons moving the $+z$ direction towards the center of the beam resulting in collimation. We can compare the spatial and temporal evolution of this global field for all materials by examining radial lineouts of B_θ, as shown in Fig. 6.8.

An initial scan of the global field over all z values indicates the maximum field strength occurs at $z = 85$ μm (5 μm downstream of the injection location at $z = 80$ μm) for all materials and times. Lineouts are taken there and at $z = 95$ μm in order to investigate the spatial dependence of the field. Field profiles are shown at three time steps during the simulation: 0.3, 0.8

(electron pulse peak time) and 1.6 (magnetic field energy peak time) ps. Beginning at the top of the left column, we see global field strengths of $\approx$ 20 MG for Al, Cu and Ag at a radius of $\approx$ 10 μm. The oscillating polarity of the magnetic filaments can be seen at radii below 5 μm. Peak global field strength in Au is relatively low ($\approx$ 5 MG) at this point in time and has a larger spatial extent radially than other materials. At the peak time of electron injection (middle plot), peak field strengths for Al, Cu and Ag have attained close their maximum values over the entire simulation. Note the Cu and Ag field profiles are almost identical, and the maximum field strength for both ($\approx$ 50 MG) is nearly double that of Al. The global field for Au has grown significantly to 30 MG at its peak and maintains relatively large values at small radii. Well after the end of electron injection (bottom plot), not much as has changed in Al, Cu and Ag. In Au, however, the field strength has grown to a value similar to those of Cu and Ag.

The column on the right shows corresponding magnetic field profiles at $z = 95$ μm. Most important is the fact that global field strengths are relatively quite low at this distance, attaining peak values less than half those at $z = 85$ μm for all materials. Also important is that peak global field strengths are attained at very different radii for the various materials, indicating smaller electron beam opening angles (possibly due to collimation).

It it is useful to examine the peak value of the global magnetic field as a function of time, as plotted in Fig. 6.9. Growth is similar for Al, Cu and Ag for the first 0.2 ps but quickly flattens in the Al case. Note the maximum field strength attained in Ag is only $\approx$ 10% higher than that attained in Cu. For the first half of the electron pulse, peak field strength in Au is $\approx$ 15 MG lower than in Cu and Ag and reaches its maximum value later in time than in other materials. These results are clearly significant because strong magnetic fields are desired as early as possible during electron injection for beam collimation.

In addition to field strength and temporal evolution, spatial development of the magnetic field is important when considering collimation. The two important parameters of spatial development to consider are the radial location of the peak global magnetic field and the dependence

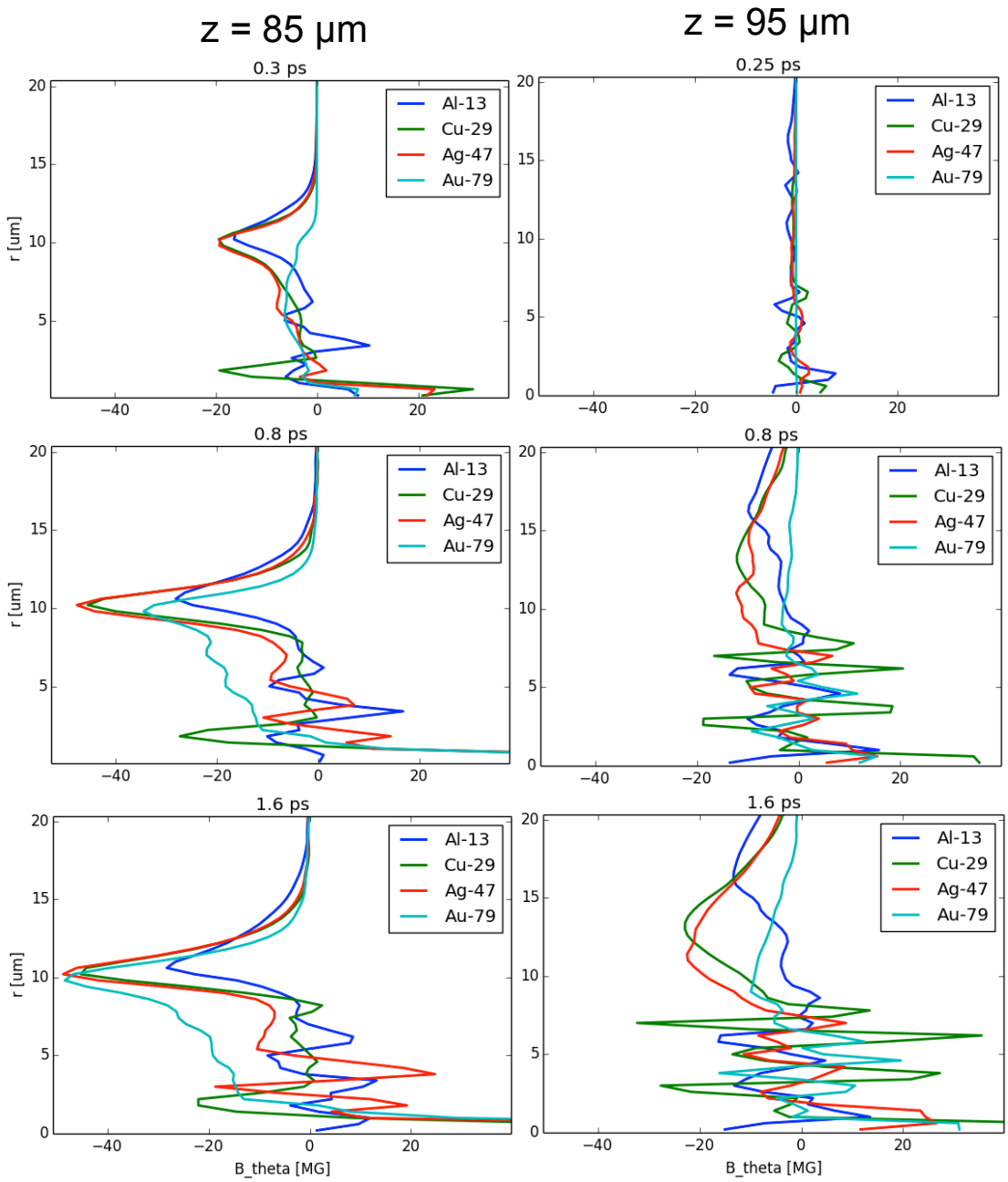

Figure 6.8: Radial B_θ line outs (radius vs field strength) for all materials at $z = 85$ μm (left) and $z = 95$ μm (right) at three different times.

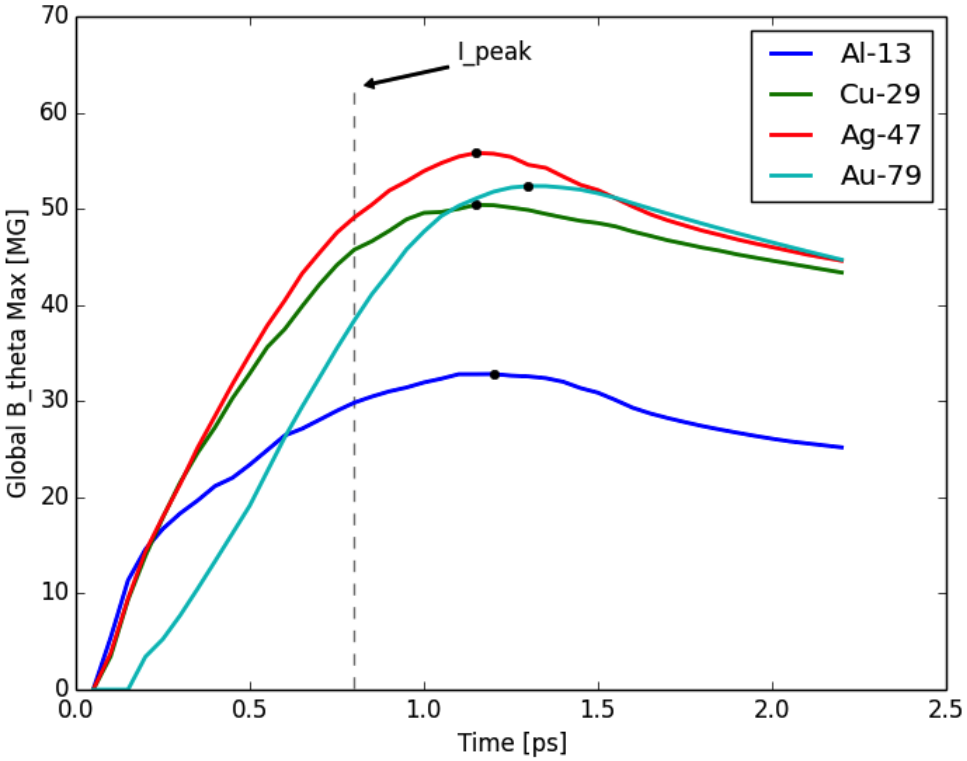

Figure 6.9: Maximum global B_θ value vs time. Black circles indicate maximum values for all times and the dotted black line indicates peak intensity time for electron injection.

of peak global field strength on the distance from the electron injection plane. Fig. 6.10 shows the peak value of the global magnetic field as a function of distance along the electron propagation axis. At distances far from the injection plane global field values are on the order of the random oscillations in field strength arising from electron beam nonuniformities. These oscillations are on the order of 2 MG, and therefore only global field strengths greater than 2 MG are considered here. In the top right plot of Fig. 6.8 these small oscillations in field strength can be seen at radii above 15 μm. Additionally, the lineouts in Fig. 6.10 are averaged over 3 μm bins along the z-axis to reduce noise. The extent of the global field in the z-direction decreases as material atomic number increases. In fact, the global field in Au disappears within 20 μm of the electron injection plane. Field strength values are highest in Cu and Ag for the 20-30 μm after injection, after which that in Al is slightly higher.

The radial location of the global field is also important for collimation as the electron beam quickly diverges after injection. Fig. 6.11 shows the radial location of the peak global field as a function of distance from the electron injection plane. The radii in the Cu and Ag runs are only a few microns smaller than that in Al. In Au, however, the global field is located significantly closer to injection radius of 5 μm, a potentially useful property when choosing the optimal material for collimation.

To summarize, there are a few key features of the global magnetic field that vary amongst materials, all being important for collimation. Magnetic fields in Cu and Ag evolve in a very similar manner in that they have the fastest growth rates and attain $\approx$ 50 MG peak field values. In addition, they have the highest field strengths for the first 25 μm after electron injection along the electron propagation axis. The collimating field in Al extends the farthest along the electron propagation axis, though it's maximum value is around half those attained in other materials. The field in Au grows more slowly than those in Cu and Ag, but eventually reaches a similar maximum strength. In addition, the fields in Au develop closer to the injection radius than other materials, though the spatial extent is only 15 μm beyond the injection plane.

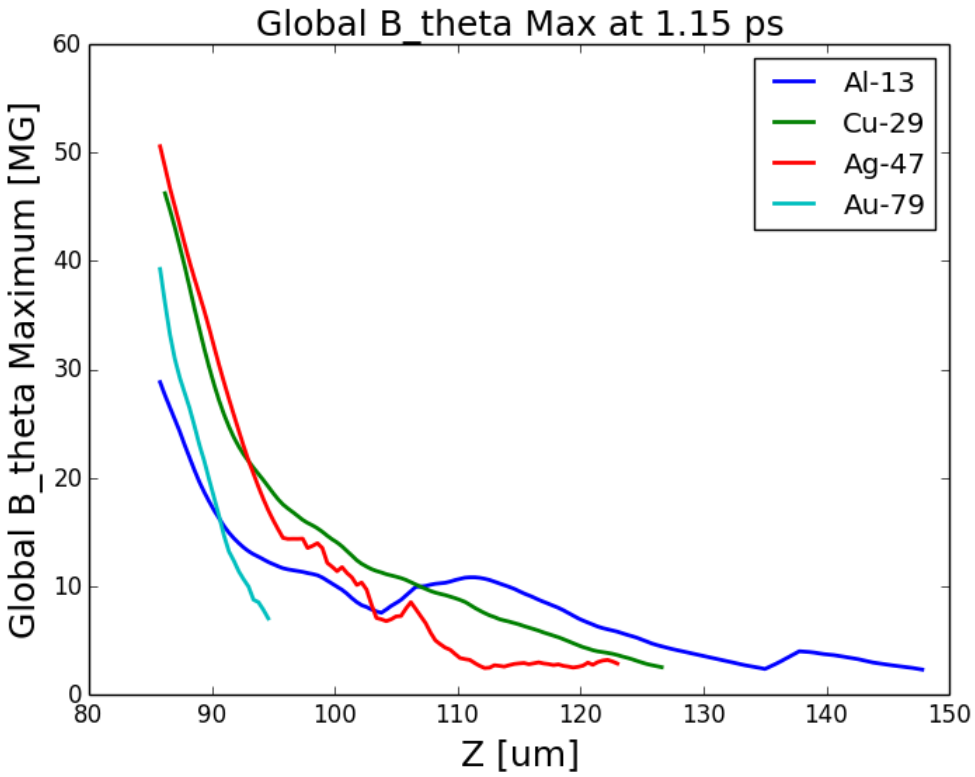

Figure 6.10: Peak global magnetic field value vs distance along the z (electron propagation) axis as 1.15 ps (maximum field strength timestep).

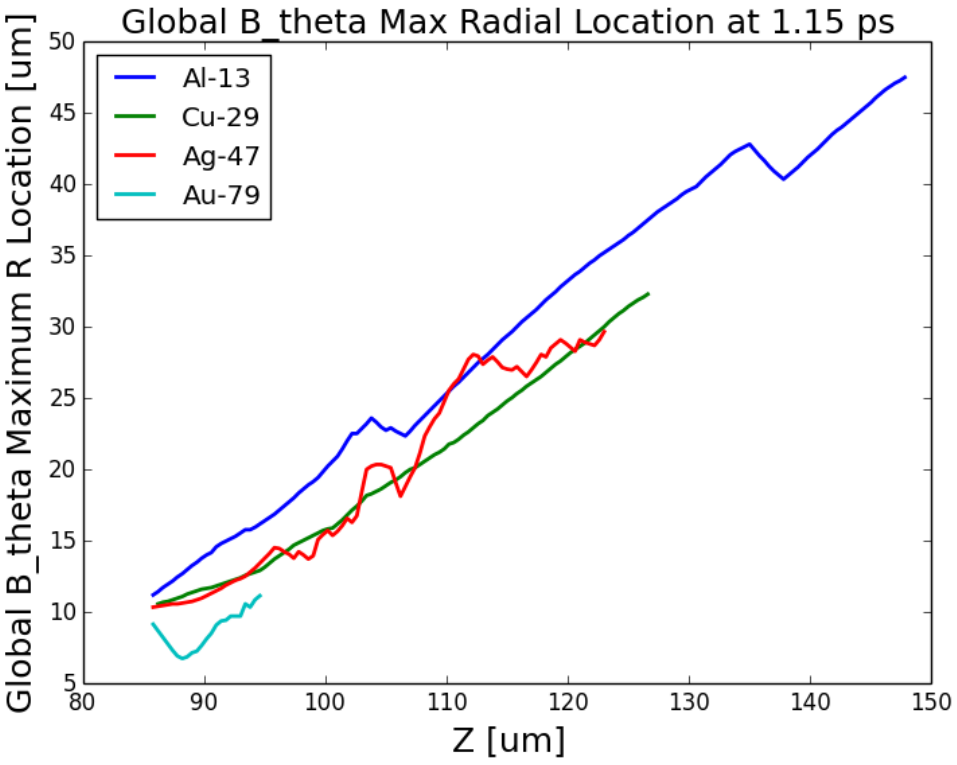

Figure 6.11: Peak global magnetic field radial location vs distance along the z-axis as 1.15 ps.

6.3.3 Resistivity and Field Growth

As described in the previous chapter, magnetic field growth is directly related to resistivity and current evolution. For convenience, Eq. 5.1 is repeated here in the cylindrical coordinate system used in the simulations in this chapter:

$$\frac{\partial \mathbf{B}_\theta}{\partial t} = \mathbf{J_z}\frac{\partial \eta}{\partial r} + \eta\frac{\partial \mathbf{J_z}}{\partial r}. \tag{6.1}$$

ZUMA was configured to output particle and resistivity data every 50 fs. The particle data was used to calculate current density, which was then spatially smoothed using a Savitzky-Golay filter with a window size of 3 data points (1.2 μm). The current density, $\mathbf{J_z}$, and resistivity, η, were then used to estimate magnetic field growth using Eq. 6.1. The running integral of $\frac{\partial \mathbf{B}_\theta}{\partial t}$ yielded an estimate of $\mathbf{B}_\theta(\mathbf{t})$, and this result is compared to the magnetic field calculated by ZUMA during runtime (see Eq. 3.3.1) in Fig. 6.12. The particle data used to calculate current included only relative macroparticle weights, thus absolute magnetic field values could not be calculated. Relative values of $\mathbf{B}_\theta(\mathbf{t})$, however, are reproduced well for all materials.

Relative field growth due to each source term on the RHS of Eq. 6.1 can seen in Fig. 6.13(a). T1 denotes the term depending on the current gradient while T2 denotes the term depending on the resistivity gradient. T1 and T2 have opposite signs for most the simulation. Most noticeable is how T2 for Au is very small for the entire run, thus allowing the total field strength to reach values comparable to those of Cu and Ag even though the individual contribution from T1 is only half those of Cu and Ag.

Figure 6.13(b) shows the ratio of the absolute value of the magnetic field contribution from each source term (|T1| / |T2|). T1 clearly dominates over T2 in Au for all times with the ratio starting near 90. The ratio oscillates at first because T2 initially is positive and increasing, then decreases and becomes negative. The behavior for Cu and Ag is similar for both terms, with T1 $\sim$2x larger than T2 for all times. For Al, T1 dominates until $\sim$0.5 ps. Afterwards, the

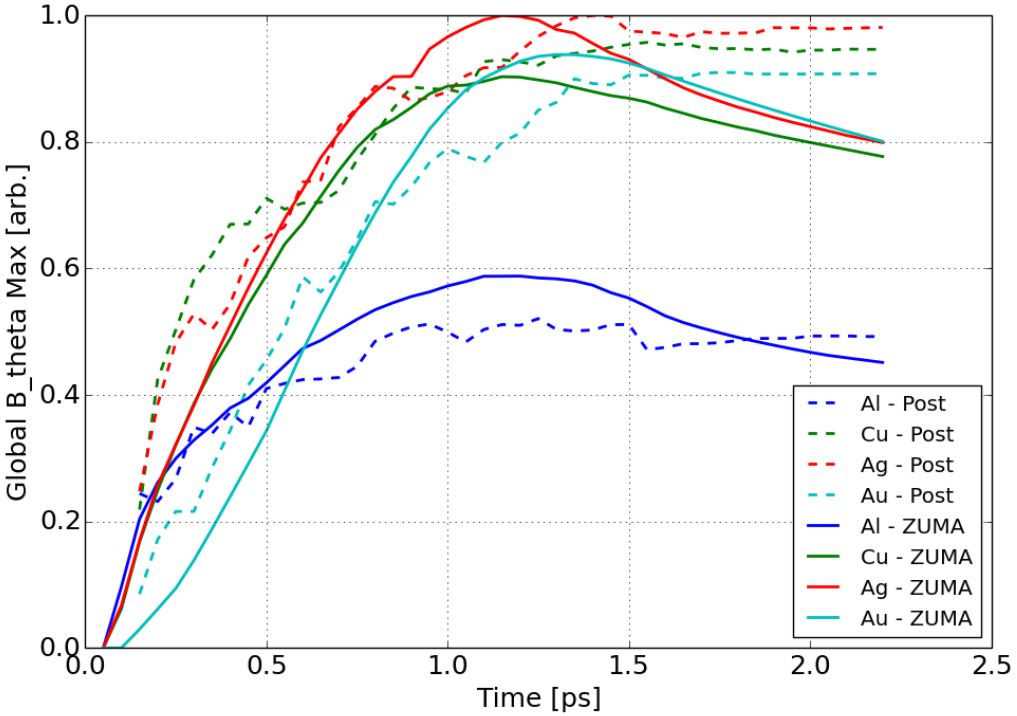

Figure 6.12: Maximum global magnetic field (normalized) over time computed by both ZUMA during simulation runtime and post processing of ZUMA output.

contribution from T2 is strong enough to dampen the maximum global field growth, as seen in Fig. 6.12.

The competition over time between source terms is different for each material but, as is the case with Au and Cu for example, can lead to similar maximum magnetic field strengths. Understanding the resistivity evolution for each material helps us to further understand source term evolution. Figure 6.14 shows the resistivity vs. temperature curve predicted by the LMD Model (see Sec. 2.3.5) for Al. Resistivity increases with temperature and reaches a peak around $T_{peak} \approx 10$ eV, then begins to fall again. The temperature range $T > T_{peak}$, where resistivity is inversely proportional to temperature, is known as the Spitzer regime. The shape of this curve allows for both positive and negative spatial gradients to develop during transport because of the inhomogeneous heating caused by the nonuniform electron beam. On average, all terms on the RHS of Eq. 6.1, except the resistivity gradient $\frac{\partial \eta}{\partial r}$, maintain their sign throughout the simulation. Thus the direction of this gradient serves to either intensify or limit magnetic field growth.

Figure 6.15 shows the resistivity evolution of all materials at various timesteps during the simulation. Heating is most intense between the radii of 0 and 5 μm (center of the electron beam) and resistivity, therefore, changes the fastest there. At $t = 0.1$ ps, resistivity values for Al, Cu and Ag have already reached the maximum values predicted by the LMD model and have moved into the Spitzer regime in the center. Away from the center of the beam (r >30 μm), there is very little heating and resistivities remain at the initial values set by the LMD model. As time progresses, resistivity values in the center continue to drop at different rates for each material. The resistivity evolution for Au is much slower than in the other materials due to its higher heat capacity, as will be discussed later. Spatially, we observe that resistivity remains high near the beam edge (≈ 10 μm) for most of the simulation while rising and falling in the center. It is the evolving gradient between these two locations that contributes to source term T2.

The resistivity gradient for the same timesteps is shown in Fig. 6.16. At very early times we observe two gradients with opposite signs; the first is strongly negative and comes

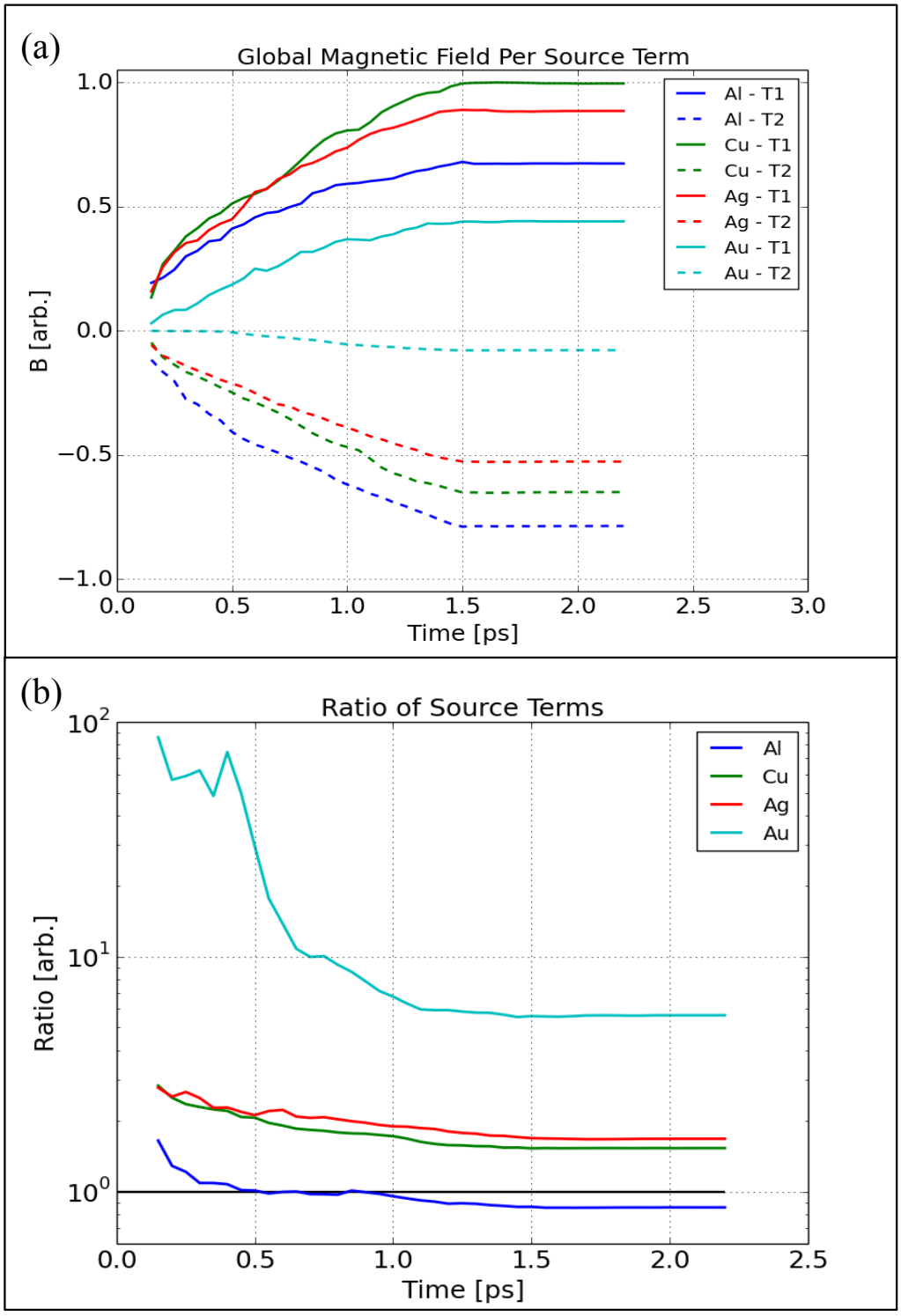

Figure 6.13: (a) $\mathbf{B}_\theta(\mathbf{t})$, normalized to maximum field value, due to individual source terms from Eq. 6.1 where T1 $= \eta \frac{\partial \mathbf{J_z}}{\partial r}$ and T2 $= \mathbf{J_z} \frac{\partial \eta}{\partial r}$. (b) Ratio |T1| / |T2| vs time.

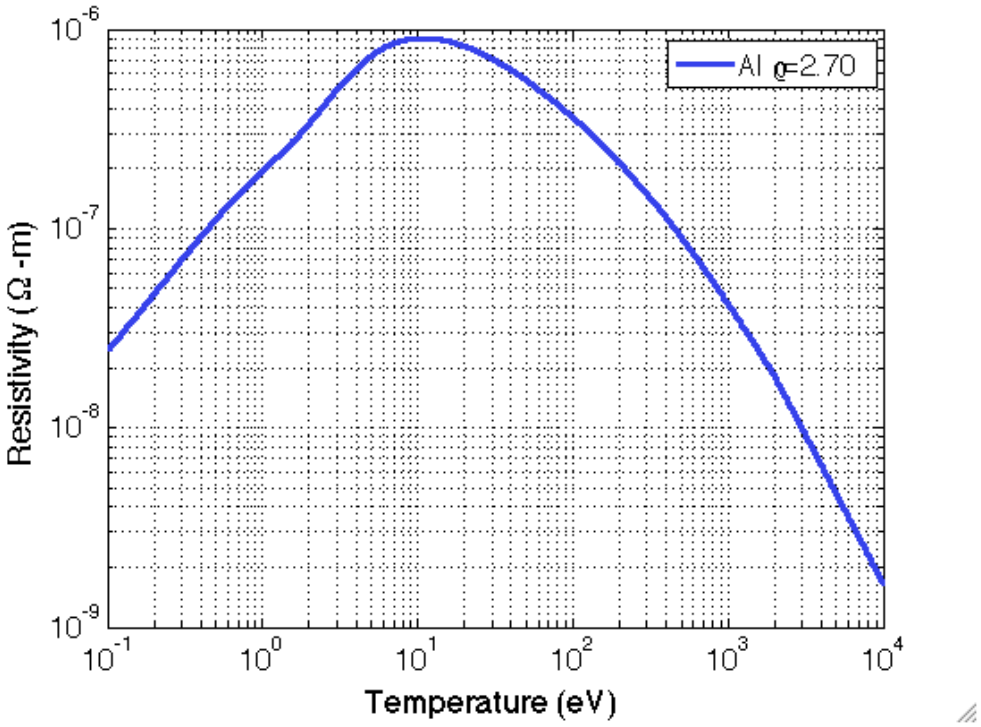

Figure 6.14: Resistivity vs. temperature for Al predicted by the LMD model.

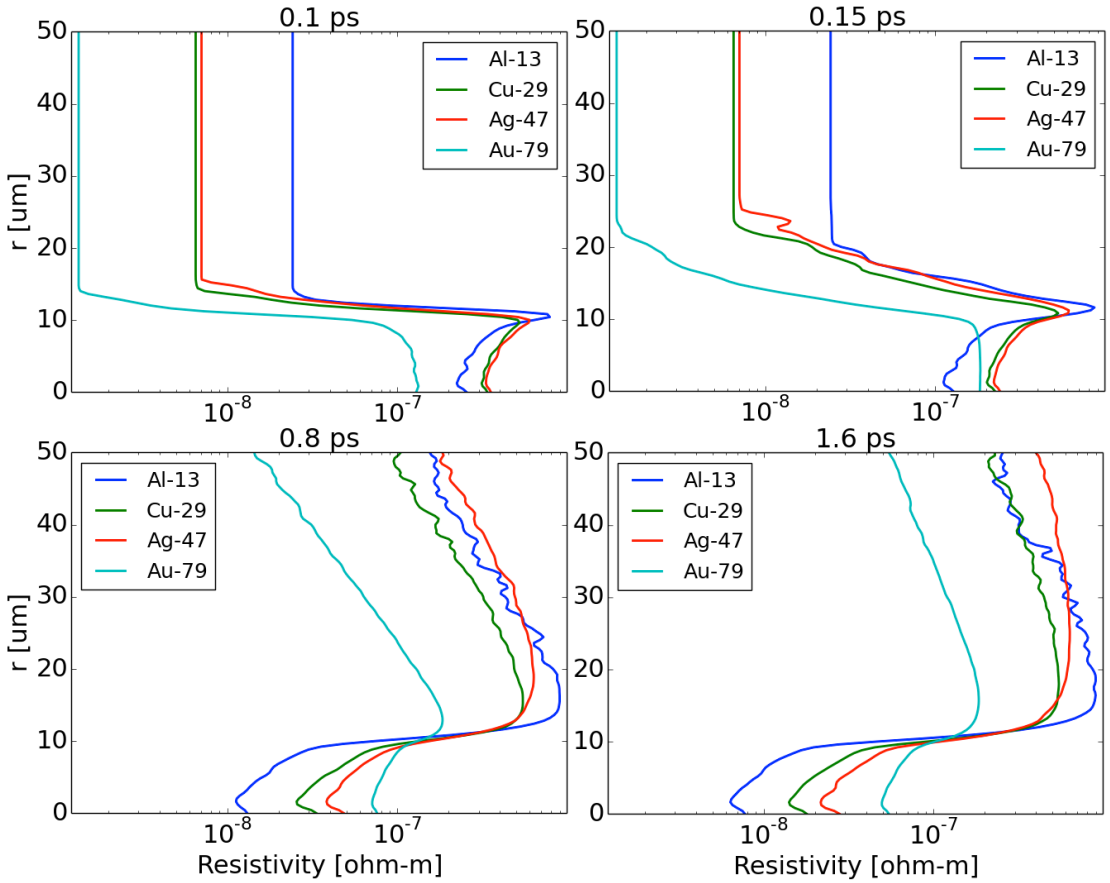

Figure 6.15: Radial line outs of resistivity for all materials at a depth of $z = 85$ μm at 0.1, 0.15, 0.8 and 1.6 ps.

from the difference in resistivity between the beam edge and the background material, and the second is strongly positive and arises from the resistivity difference between the beam edge and beam center. As the beam spreads and slowly heats the background material at larger radii, the negative gradient disappears. The positive gradient remains for all materials and contributes to source term T2, as mentioned above. It is positive because the resistivity in the center is lower than at the beam edge for almost all times. It is clear that Al has the largest gradient, followed by Cu, Ag and finally gold. Note the maximum gradient for Au remains very small throughout the simulation, thus keeping source term T2 small and allowing T1 to dominate magnetic field growth. For the other materials, as well, the maximum gradient as a function of time corresponds nicely with the evolution of T2.

As seen in Chapter 2, Fig. 2.7, resistivity evolution in the LMD model is very similar to that of Spitzer theory after a certain material temperature has been reached (known as the Spitzer regime). As shown in Fig. 6.15, resistivity values in the beam center reach the Spitzer regime very quickly, so we can use the Spitzer model to understand evolution there. As a verification of this, Fig. 6.17 shows resistivity vs. time in the center of the beam (r = 2 μm) as calculated by ZUMA using the LMD model and estimated via post processing of ionization state and temperature data using the Spitzer model. As seen in Fig. 2.7, Spitzer and LMD theory are in very good agreement after 250 eV. The estimated resistivity, therefore, was plotted after the time at which this temperature was reached for each material. Both models agree to within a factor of 2, as expected.

The Spitzer model (Eq. 2.85) dictates that $\eta \sim Z^*/T^{3/2}$. We can, therefore, investigate Z^* and T evolution in order to understand η evolution. The growth rates for ionization state and temperature are shown in Fig. 6.18 for the center of the beam. For Al, Cu and Ag, the ionization growth rate drops rather quickly. Indeed, the ionization state reaches its peak value in these materials by $\sim$0.6 ps. Because Au has a much higher atomic number and, therefore, much larger sink for deposited energy, the decrease in ionization growth rate is much slower.

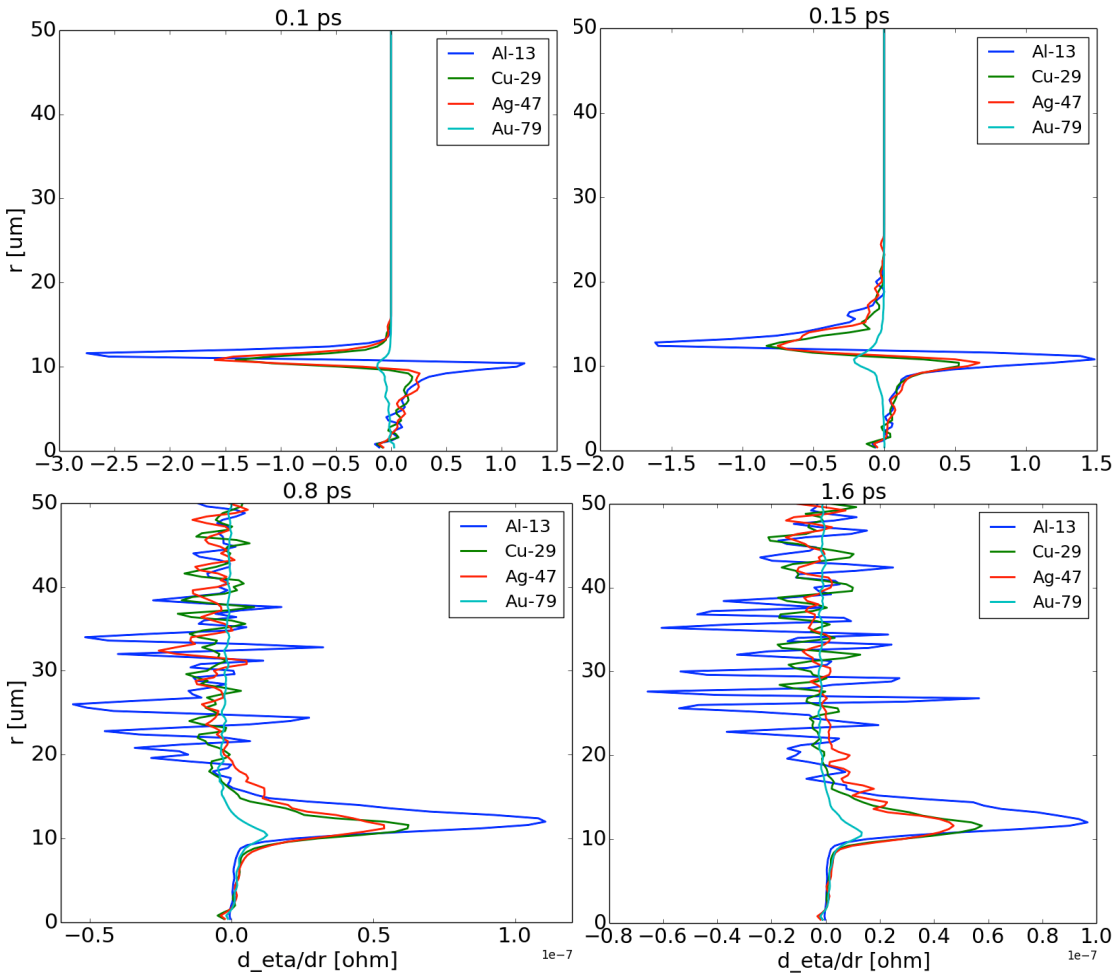

Figure 6.16: Radial line outs of resistivity gradient for all materials at a depth of $z = 85$ μm at 0.1, 0.15, 0.8 and 1.6 ps.

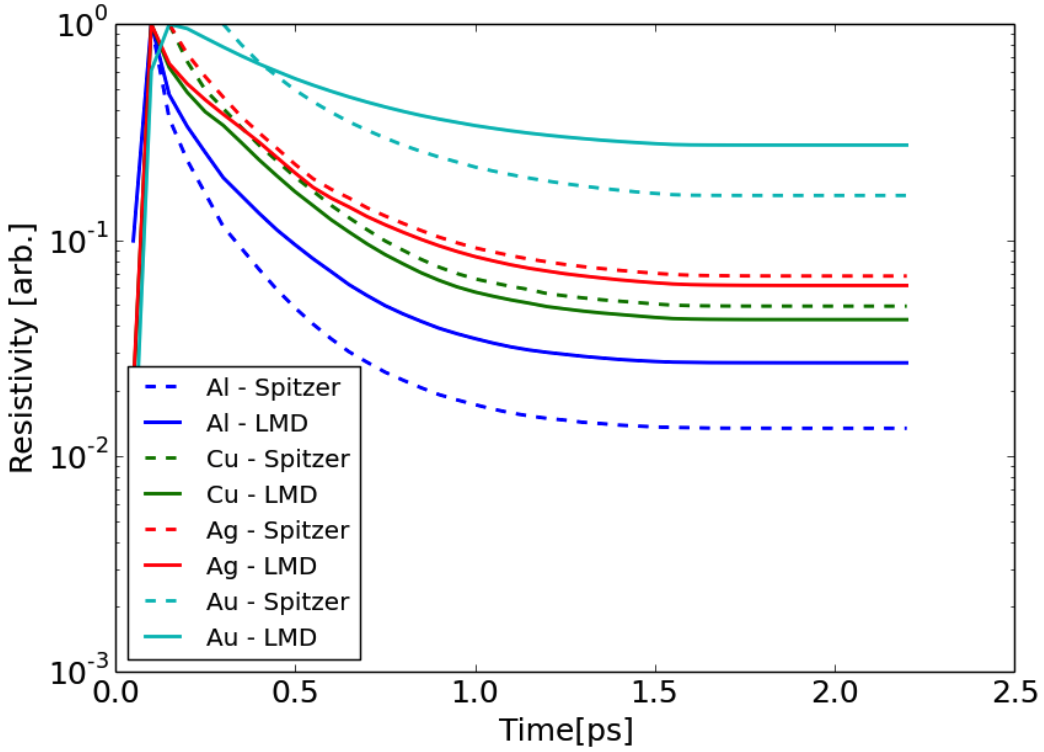

Figure 6.17: Resistivity at r = 2 μm calculated by ZUMA/LMD (solid lines) and estimated from Z^* and T data using the Spitzer model (dashed lines). Values are normalized to the maximum for each material and model.

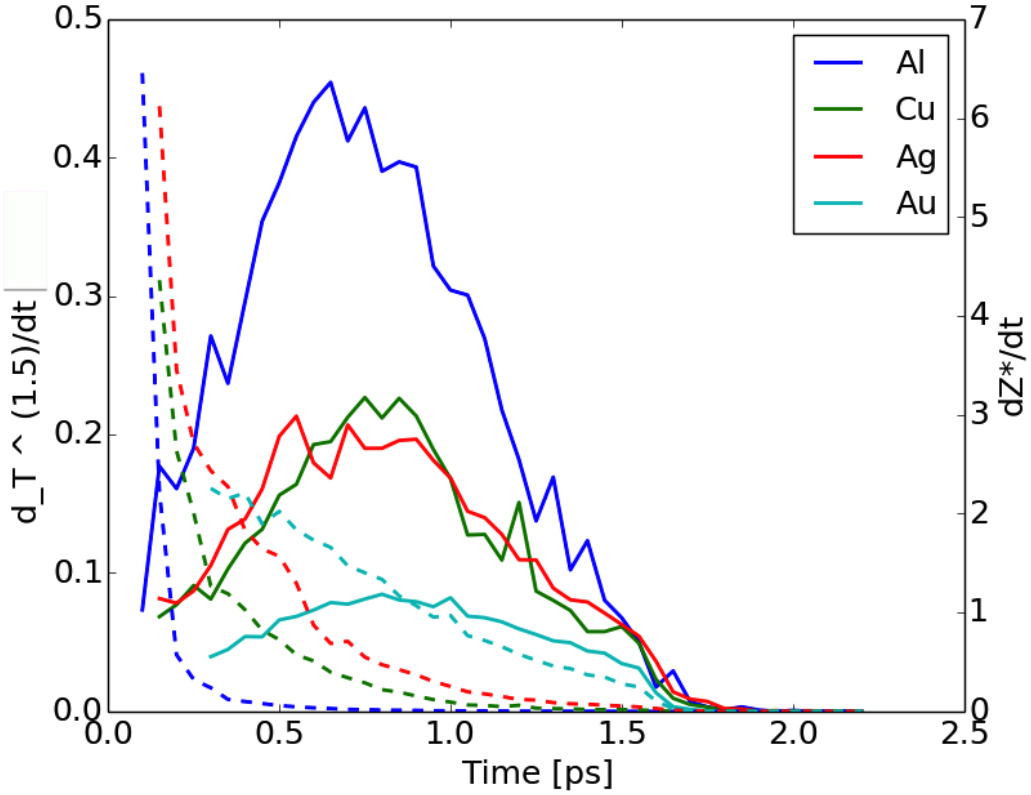

Figure 6.18: dZ^*/dt (dotted lines, right y-axis) and $dT^{3/2}/dt$ (solid lines, left y-axis) at r = 2 μm.

For all materials, $dT^{3/2}/dt$ evolves as described in Eq. 3.15, with Al achieving the largest growth rate, followed by Cu, Ag and finally Au. It is now clear why the resistivity drops the fastest in Al, as seen in Fig. 6.17; the ionization growth rate drops quickly as the ionization state reaches 13 while the temperature continues to increase. Behavior is similar for Cu and Ag, though the temperature growth rates are not as high as in Al and the ionization growth rates are decrease more slowly. Because of this, the resistivity does not drop as sharply as in Al. In Au, ionization growth rates are the highest for most of the pulse while temperature growth rates are the smallest, thus leading to the slowest decrease in resistivity in the center of the beam.

In summary, it has been shown that the resistive and current gradient terms dominate evolution of the azimuthal component of magnetic field growth during transport. These terms oppose each other for most of the fast electron pulse, with the current term dominating in strength over the resistivity term. For Au in particular, the resistivity term is so small that it allows large magnetic fields to develop similar in strength to those in Cu and Ag. Spatially, we observe that it is the resistivity gradient between the electron beam edge and center that determines global magnetic field development. The resistivity, for most times, evolves according to the Spitzer model. In general, it was found that as material atomic number increase, ionization growth rates increases and temperature growth rates decrease, leading to a slower drop in resistivity in the beam center for higher atomic number materials. This slower drop leads to larger magnetic field strengths via the resistivity gradient term for magnetic field growth.

6.4 Summary and Conclusions

The simulations in this chapter have, for the first time, yielded important results that help us to understand how fast electron transport at Titan-like conditions is dynamically affected by deposition and collimation. The dominant mechanism for slowing down fast electrons is ohmic deposition, though in Au collisional deposition dominates in very large targets. The amount

of initial energy deposited only increases $\sim 5\%$ when considering Cu and Ag over Al, while deposition amounts double in large Au targets due collisional stopping.

Cu and Ag are more favorable than Al for collimation as global magnetic fields in those materials grow faster, attain higher strengths and are located closer to the beam center than in Al. Though the field in Au achieves a similar strength to those in Cu and Ag and is located even closer to the electron beam center, it grows at a slower rate and does not persist along the propagation axis far beyond the injection location. Magnetic field growth rates are determined by the competition between current density gradient and resistivity gradient source terms. At very early times, these terms constructively yield collimating fields as both gradients are oriented towards the electron beam center. Once resistivity values in the center move into the Spitzer regime, the magnetic field growth source terms oppose each other in sign. Resistivity evolution is then dominated by the competition between the ionization state and temperature growth rates.

These results have important implications for the cone tip design in the Fast Ignition scheme. Deposition (Fig. 6.3) and spatial field strength (Fig. 6.10) analyses suggest using a tip thickness of less than $\sim$20 μm. With higher atomic number materials, larger cone tips will significantly affect the fast electron beam via deposition. Furthermore, maximum field strengths drop very quickly along the propagation axis, so thicker cone tips offer little advantage in terms of collimation.

Field growth rate (Fig. 6.9) and field location (Fig. 6.11) analyses show that mid and high atomic number materials can offer significant advantages over low atomic number materials in terms of collimating fields. These advantages can be exploited in multilayer target designs such as that used in the experiment described in Chapter 5 (see Fig. 5.1). The Al source and propagation layers can be replaced with Cu or Ag, as they will yield stronger collimating fields. The transport layer material can have a higher atomic number, such as Au, as this material has been shown to produce strong pinching fields close to the electron injection radius. This layer should also be thin to avoid deposition issues.

At FI conditions ($\sim$200 kJ deposited in 20 ps with a 0.5 ps ramp) [33], a large amount of energy is deposited very quickly. We expect, then, that material resistivities will move into the Spitzer regime and strong magnetic fields will be formed before the majority of the electron pulse is injected. With higher atomic number materials, the competition between ionization state and temperature persists longer than in lower atomic number materials as fast electron energy is deposited. Given the FI pulselength is $\sim$20x that of Titan, higher atomic number materials are expected to have an advantage as collimating fields will grow during a longer period with the pulse length.

Chapter 6, in part, is a reprint of material as it appears in S. Chawla, M. Bailly-Grandvaux, H.S. McLean, P.K. Patel, M.S. Wei, F.N. Beg, Physics of Plasmas **26**, 033111 (2019). The dissertation author was the primary investigator and author of this material.

Chapter 7

Summary and Future Work

This thesis describes detailed experimental and computational investigations of how cone tip material affects the transport of laser-produced relativistic electrons.

An experiment was performed using the Titan laser (150 J, 0.7 ps pulse duration, 17 mJ average prepulse pedestal energy in 2.3 ns, 1 μm wavelength) at the Jupiter Laser Facility, Lawrence Livermore National Laboratory. The laser irradiated multilayer targets that consisted of a common Al front layer (3 μm thick), a Z-transport layer made of either Au (8 μm), Mo (14 μm) or Al (33 μm) and a Cu tracer layer (22 μm) buried 110 μm behind the transport layer. Bremmstrahlung spectrometer data verified the electron source was similar for the various transport targets. The Cu Kα imager consistently recorded smaller emission spots from the Au and Mo transport layer targets as compared to the Al transport layer targets, but with similar electron flux levels near the beam center.

2D collisional PIC simulations of the laser-solid interaction and subsequent electron transport (along with a radiation-hydrodynamics simulation to predict the preplasma structure) were performed using the PICLS code. Electron density results were in excellent agreement with experimental trends. Magnetic field results suggested that self-generated resistive fields were responsible for the significantly different transport in Al vs Au transport targets. In the

center of the Al target, full ionization is achieved very quickly while the temperature continues to increase throughout the laser pulse duration. The resistivity, therefore, drops in the center while the current density remains high. Thus the the current gradient and resistivity gradient source terms of the magnetic field growth equation oppose each other and limit field growth. The result is an electron beam the diverges as it propagates through the target with out any collimating effect from magnetic fields. In contrast, both ionization level and temperature in the center of the Au target increase with time, so the the decrease in resistivity is strongly mitigated. The resistivity gradient contribution to the magnetic field is very small and thus cannot balance the field growth caused the current driven term. Very strong collimating fields are formed and collimate the fast electron beam as it propagates. Furthermore, electron flux results showed flux levels in the center of the Au target surpassing those in the Al target at early times, and eventually falling below them at later times. These results suggested the competing mechanisms (in terms of electron flux) of deposition and collimation were important to consider in various materials when optimizing for energy flux.

In order to gain a deeper understanding of the temporal and spatial evolution of magnetic fields and deposition in various materials during electron transport, a computation study using the hybrid-PIC code ZUMA was performed. A Titan-like electron source based on the source produced from the previously mentioned PICLS simulations was injected into four materials: Al, Cu, Ag and Au.

Total energy deposition by the electron beam was similar in Al, Cu and Ag targets for all electron energy levels. Though more energy was deposited via collisional deposition for Cu and Ag targets, ohmic deposition was still the dominant mechanism for deposition for all 3 types. In Au, ohmic deposition dominated at early times while collisional deposition dominated at later times. This was because electrons in the 1-6 MeV range continued to propagate throughout the target after the end of the pulse and deposit their energy via collisions.

Analysis of the azimuthal magnetic field showed the presence of strong, collimating

magnetic fields generated near the beam edge during transport. Peak field values occurred $\sim 5\mu$m from the injection location along the electron propagation axis. The relative magnitudes of the peak global field varied both in time and space between materials. Magnetic fields in Cu and Ag evolve in a very similar manner in that they have the fastest growth rates and attain ≈ 50 MG peak field values. In addition, they have the highest field strengths for the first 25 μm after electron injection along the electron propagation axis. The collimating field in Al extends the farthest along the electron propagation axis, though it's maximum value is around half those attained in other materials. The field in Au grows more slowly than those in Cu and Ag, but eventually reaches a similar maximum strength. In addition, the fields in Au develop closer to the injection radius than other materials, though the spatial extent is only 15 μm beyond the injection plane.

Current and resistivity results were used to verify field growth is dominated by the current gradient and resistivity gradient terms in Faraday's law. These terms oppose each other in sign for most of the fast electron pulse, with the current term dominating in strength over the resistivity term. For Au in particular, the resistivity term is so small that it allows large magnetic fields to develop similar in strength to those in Cu and Ag. Spatially, we observe that it is the resistivity gradient between the electron beam edge and center that determines global magnetic field development. The resistivity, for most times, evolves according to the Spitzer model. In general, it was found that as material atomic number increases, ionization growth rates increase and temperature growth rates decrease, leading to a slower drop in resistivity in the beam center for higher atomic number materials. This slower drop leads to larger magnetic field strengths via the resistivity gradient term for magnetic field growth.

These results open the door for further computational and experimental work to investigate how material properties can be exploited to maximize fast electron beam collimation whilst minimizing deposition rates. While hybrid-PIC codes are very useful for quick parameter space studies, PIC simulations with more accurate ionization, radiation transport and heat transport

models should be used to solidify the results presented here. Additional materials, along with complex multilayer targets, can be simulated systematically to find targets that balance deposition, field growth rate and field spatial structure to maximize energy flux through cone tip scale lengths. Moreover, transport at FI conditions will be different due to increased laser spot size, energy and pulse length. More energy will be injected into the cone tip very quickly, leading to faster ionization and heating rates. Higher atomic number materials may be favorable at these conditions as ionization can continue for a longer period during the $\sim$20 ps FI pulse. In addition, experiments with single material and multilayer targets can be performed at various laser conditions to verify the predictions of simulations. Given the experiments here only investigated 3 transport materials without varying transport layer thickness, location, and source/propagation layer material, the available parameter space for experimentation is quite large.

Bibliography

[1] J. Lindl, Physics of Plasmas **2**, 3933 (1995).

[2] A. J. Mackinnon, *Fast Ignition Using Energetic Electrons or Protons* (2007).

[3] S. Atzeni, Physics of Plasmas **6**, 3316 (1999).

[4] J. Freidberg, R. Mitchell, R. Morse, and L. Rudsinski, Phys. Rev. Lett. **28**, 795 (1972).

[5] P. Mora, PPCF **43**, A31 (2001).

[6] Y. T. Lee and R. M. More, Phys. Fluids **27**, 1273 (1984).

[7] M. P. Desjarlais, Cont. Plasma Phys. **41**, 267 (2001).

[8] C. Hombourger, Journal Phys. B **31**, 3693 (1998).

[9] C. Chen, J. King, M. Key, K. Akli, F. Beg, H. Chen, R. Freeman, A. Link, A. Mackinnon, and A. MacPhee, Rev. Sci. Inst. **79**, 10E305 (2008).

[10] G. Fraley, E. Linnebur, R. Mason, and R. Morse, Physics of Fluids **17**, 474 (1974).

[11] D. Strickland and G. Mourou, Optics Communications **55**, 447 (1985).

[12] W. Joosen, H. Bakker, L. Noordam, H. Muller, and H. Heuvell, JOSA B **8**, 2537 (1991).

[13] R. Baumgartner and R. Byer, Journal of Quantum Electronics **15**, 432 (1979).

[14] M. Tabak, J. Hammer, M. E. Glinsky, W. L. Kruer, S. C. Wilks, J. Woodworth, E. M. Campbell, M. D. Perry, and R. J. Mason, Phys. Plasmas **1**, 1626 (1994).

[15] P. Norreys, R. Allott, R. Clarke, J. Collier, D. Neely, S. Rose, M. Zepf, M. Santala, A. Bell, and K. Krushelnick, Physics of Plasmas **7**, 3721 (2000).

[16] R. Kodama, P. A. Norreys, K. Mima, A. E. Dangor, R. G. Evans, H. Fujita, Y. Kitagawa, K. Krusheinick, T. Miyakoshi, and N. Miyanaga, Nature **412**, 798 (2001).

[17] A. A. Solodov, K. S. Anderson, R. Betti, V. Gotcheva, J. Myatt, J. A. Delettrez, S. Skupsky, W. Theobald, and C. Stoeckl, Phys. Plasmas **15**, 112702 (2008).

[18] A. R. Bell and R. J. Kingham, Phys. Rev. Lett. **91**, 35003 (2003).

[19] L. Gremillet, D. Bénisti, E. Lefebvre, and A. Bret, Phys. Plasmas **14**, 040704 (2007).

[20] J. J. Honrubia, C. Alfonsin, L. Alonso, B. Perez, and J. A. Cerrada, Laser Part. Beams **24**, 217 (2006).

[21] J. J. Honrubia, A. Antonicci, and D. Moreno, Laser Part. Beams **22**, 129 (2004).

[22] J. A. Koch, M. H. Key, R. R. Freeman, S. P. Hatchett, R. W. Lee, D. Pennington, R. B. Stephens, and M. Tabak, Phys. Rev. E **65**, 016410 (2001).

[23] J. J. Santos, F. Amiranoff, S. D. Baton, L. Gremillet, M. Koenig, E. Martinolli, M. R. L. Gloahec, C. Rousseaux, D. Batani, and A. Bernardinello, Phys. Rev. Lett. **89**, 25001 (2002).

[24] M. H. Key, M. D. Cable, T. E. Cowan, K. G. Estabrook, B. A. Hammel, S. P. Hatchett, E. A. Henry, D. E. Hinkel, J. D. Kilkenny, J. A. Koch, W. L. Kruer, A. B. Langdon, B. F. Lasinski, R. W. Lee, B. J. MacGowan, A. MacKinnon, J. D. Moody, M. J. Moran, A. A. Offenberger, D. M. Pennington, M. D. Perry, T. J. Phillips, T. C. Sangster, M. S. Singh, M. A. Stoyer, M. Tabak, G. L. Tietbohl, M. Tsukamoto, K. Wharton, and S. C. Wilks, Phys. Plasmas **5**, 1966.

[25] F. Pisani, A. Bernardinello, D. Batani, A. Antonicci, E. Martinolli, M. Koenig, L. Gremillet, F. Amiranoff, S. Baton, and J. Davies, Phys. Rev. E **62**, 5927 (2000).

[26] C. E. Max, *Physics of Laser Fusion Volume I: Theory of the Coronal Plasma in Laser Fusion Targets*, Tech. Rep. (LLNL, 1982).

[27] S. Wilks, W. Kruer, M. Tabak, and A. Langdon, Phys. Rev. Lett. **69**, 1383 (1992).

[28] F. Beg, A. Bell, A. Dangor, C. Danson, A. Fews, M. Glinsky, B. Hammel, P. Lee, P. Norreys, and M. Tatarakis, Physics of Plasmas **4**, 447 (1997).

[29] B. Westover, C. Chen, P. Patel, M. Key, H. Mclean, R. Stephens, and F. Beg, Phys. Plasmas **18**, 063101 (2011).

[30] C. Chen, P. Patel, D. Hey, A. Mackinnon, M. Key, K. Akli, T. Bartal, F. Beg, S. Chawla, and H. Chen, Physics of Plasmas **16**, 082705 (2009).

[31] A. Kemp, Y. Sentoku, and M. Tabak, Phys. Rev. E **79**, 066406 (2009).

[32] A. Debayle, J. Honrubia, E. d'Humières, and V. T. Tikhonchuk, Phys. Rev. E **82**, 036405 (2010).

[33] D. Strozzi, M. Tabak, D. Larson, L. Divol, A. Kemp, C. Belei, M. Marinak, and M. Key, Physics of Plasmas **19**, 072711 (2012).

[34] A. Bell, J. Davies, S. Guerin, and H. Ruhl, PPCF **39**, 653 (1997).

[35] A. Solodov and R. Betti, Physics of Plasmas **15**, 042707 (2008).

[36] S. Atzeni, A. Schiavi, and J. R. Davies, Plasma Phys. Control. Fusion **51**, 015016 (2009).

[37] P. Panek, J. Kaminski, and F. Ehlotzky, Laser Physics **14** (2004).

[38] N. Mott, Proceedings of the Royal Society of London. Series A **135**, 429 (1932).

[39] M. Gryziński, Physical Review **138**, A305 (1965).

[40] R. Feynman, N. Metropolis, and E. Teller, Physical Review **75**, 1561 (1949).

[41] R. More, K. Warren, D. Young, and G. Zimmerman, Physics of Fluids **31**, 3059 (1988).

[42] L. Spitzer and R. Härm, Phys. Rev. **89**, 977 (1953).

[43] M. M. Marinak, S. W. Haan, T. R. Dittrich, R. E. Tipton, and G. B. Zimmerman, Phys. Plasmas **5**, 1125 (1998).

[44] *The Flash Center for Computational Science, User Guide Version 4.2* (2014).

[45] C. Orban, M. Fatenejad, S. Chawla, S. C. Wilks, and D. Q. Lamb, arXiv:1306.1584 (2013).

[46] A. Langdon, B. Cohen, and A. Friedman, Journal of Computational Physics **51**, 107 (1983).

[47] Y. Sentoku and A. Kemp, J. Comp. Phys. **227**, 6846 (2008).

[48] R. Mishra, *Computational study of hot electron generation and energy transport in intense laser produced hot dense matter*, Ph.D. thesis, University of Nevada, Reno (2010).

[49] J. Davies, Phys. Rev. E **65**, 026407 (2002).

[50] J. Halbleib, R. Kensek, T. Mehlhorn, G. Valdez, S. Seltzer, and M. Berger, *ITS version 3.0: The integrated TIGER series of coupled electron/photon Monte Carlo transport codes* (1992).

[51] E. Epperlein and M. Haines, Physics of Fluids **29**, 1029 (1986).

[52] R. P. Drake, *High Energy Density Physics: Fundamentals, Inertial Fusion, and Experimental Astrophysics* (2006).

[53] W. Bambynek, B. Crasemann, R. Fink, H. Freund, H. Mark, C. Swift, R. Price, and P. Rao, Reviews of Modern Physics **44**, 716 (1972).

[54] P. Rao, M. Chen, and B. Crasemann, Physical Review A **5**, 997 (1972).

[55] D. R. Welch, D. V. Rose, M. E. Cuneo, R. B. Campbell, and T. A. Mehlhorn, Physics of Plasmas **13**, 063105 (2006).

[56] D. Higginson, *Ultra-High-Contrast Laser Acceleration of Relativistic Electrons in Solid Targets*, Ph.D. thesis, University of California, San Diego (2013).

[57] K. Eidmann, J. M. ter Vehn, T. Schlegel, and S. Hüller, Phys. Rev. E **62**, 1202 (2000).

[58] D. Spence, P. Kean, and W. Sibbett, Optics Letters **16**, 42 (1991).

[59] B. Stuart, J. Bonlie, J. Britten, J. Caird, R. Cross, C. Ebbers, M. Eckart, A. Erlandson, W. Molander, and A. Ng, CLEO (2006).

[60] J.-C. Diels, J. Fontaine, I. McMichael, and F. Simoni, App. Optics **24**, 1270 (1985).

[61] S. L. Pape, Y. Tsui, A. Macphee, D. Hey, P. Patel, A. Mackinnon, M. Key, M. Wei, T. Ma, and F. Beg, Optics Letters **34**, 2997 (2009).

[62] J. P. Santos, F. Parente, and Y. K. Kim, J. Phys. B **36**, 4211 (2003).

[63] C. Reich, P. Gibbon, I. Uschmann, and E. Förster, Phys. Rev. Lett. **84**, 4846 (2000).

[64] K. U. Akli, P. K. Patel, R. V. Maren, R. B. Stephens, M. H. Key, D. P. Higginson, B. Westover, C. D. Chen, A. J. Mackinnon, and T. Bartal, JINST **5**, P07008 (2010).

[65] K. Zeil, S. D. Kraft, A. Jochmann, F. Kroll, W. Jahr, U. Schramm, L. Karsch, J. Pawelke, B. Hidding, and G. Pretzler, Rev. Sci. Inst. **81**, 013307 (2010).

[66] B. R. Maddox, H. S. Park, B. A. Remington, and M. McKernan, Rev. Sci. Inst. **79**, (2008).

[67] J. A. Koch, Y. Aglitskiy, C. Brown, T. Cowan, R. Freeman, S. Hatchett, G. Holland, M. Key, A. Mackinnon, and J. Seely, Rev. Sci. Inst. **74**, 2130 (2003).

[68] J. Koch, O. Landen, T. Barbee, P. Celliers, L. D. Silva, S. Glendinning, B. Hammel, D. Kalantar, C. Brown, and J. Seely, App. Optics **37**, 1784 (1998).

[69] Y. Sentoku, E. d'Humières, L. Romagnani, P. Audebert, and J. Fuchs, Phys. Rev. Lett. **107**, 135005 (2011).

[70] T. Johzaki, Y. Sentoku, H. Nagatomo, H. Sakagami, Y. Nakao, and K. Mima, Plasma Phys. Controlled Fusion **51**, 014002 (2009).

[71] B. Ramakrishna, S. Kar, A. Robinson, D. Adams, K. Markey, M. Quinn, X. Yuan, P. Mckenna, K. Lancaster, J. Green, R. Scott, P. Norreys, J. Schreiber, and M. Zepf, Phys. Rev. Lett. **105**, 135001 (2010).

[72] R. Scott, C. Beaucourt, H.-P. Schlenvoigt, K. Markey, K. Lancaster, C. Ridgers, C. Brenner, J. Pasley, R. Gray, I. Musgrave, A. Robinson, K. Li, M. Notley, J. Davies, S. Baton, J. Santos, J.-L. Feugeas, P. Nicolaï, G. Malka, V. Tikhonchuk, P. Mckenna, D. Neely, S. Rose, and P. Norreys, Phys. Rev. Lett. **109**, 015001 (2012).

[73] P. M. Nilson, W. Theobald, J. Myatt, C. Stoeckl, M. Storm, O. V. Gotchev, J. D. Zuegel, R. Betti, D. D. Meyerhofer, and T. C. Sangster, Phys. Plasmas **15**, 056308 (2008).

[74] A. R. Bell, J. R. Davies, and S. M. Guerin, Phys. Rev. E **58**, 2471 (1998).

[75] Y. Ping, A. J. Kemp, L. Divol, M. H. Key, P. K. Patel, K. U. Akli, F. N. Beg, S. Chawla, C. D. Chen, R. R. Freeman, D. Hey, D. P. Higginson, L. C. Jarrott, G. E. Kemp, A. Link, H. S. Mclean, H. Sawada, R. B. Stephens, D. Turnbull, B. Westover, and S. C. Wilks, Phys. Rev. Lett. **109**, 145006 (2012).

[76] C. Zhou, T. Cai, W. Zhang, and X. He, Laser Part. Beams **30**, 111 (2012).

[77] M. Storm, A. Solodov, J. Myatt, D. Meyerhofer, C. Stoeckl, C. Mileham, R. Betti, P. Nilson, T. Sangster, and W. Theobald, Phys. Rev. Lett. **102**, 235004 (2009).

[78] R. Evans, High energy density physics **2**, 35 (2006).